IP2016 / 4th

International Workshop
on Induced Polarization

Abstracts

from poster session A

IP2016/4th International Workshop on Induced Polarization

Effect of mineralogy on Spectral Induced Polarization of sediments: A conceptual model of membrane polarization

Konstantin Titov
St. Petersburg State University
7-9 Universitetskaya naberezhnaya,
199034 St. Petersburg, Russia
k.titov@spbu.ru

Daniil Chuprinko
St. Petersburg State University
7-9 Universitetskaya naberezhnaya,
199034 St. Petersburg, Russia
d.chuprenko@spbu.ru

SUMMARY

We discuss a membrane polarization effect produced by the difference in mineral composition of walls of two sequential pores, which can occur, for example when the first pore is encased in calcite and the second – in alumosilicate. We assume that the zeta potential values of these minerals differ from each other. This leads to a difference in the cation and anion transference numbers (even if the above two pores are of the same radius) and, therefore, to a membrane polarization when an electrical field is applied. We model this effect for two pores filled with water of low salinity (1 and 10 Mol·m³), and for three pore radius values (10^{-6}, 10^{-7} and 10^{-8} m). We assume that one pore is "passive," i.e., the interface potential is zero, and the other pore is "active", with zeta potential of -75 mV. We calculate the maximum values of phase shift and the corresponding values of peak frequency as a function of lengths of the active and passive pores.

We show that the maximum phase shift corresponds to a case where the pores have the same length. The shift values are between 13 and 210 mrad depending on the ion concentration in free water and on the pore radius. The peak frequency distributions for all modeled cases are very similar and, therefore, depend mostly on the pore length. We assume that the ratio of the pore length to its diameter can achieve values between 10 and 50. With this assumption, for the pore radius of 10^{-8}, 10^{-7}, and 10^{-6} m, the membrane polarization effect can be detected in the frequency range from 1.6 kHz to 1MHz, from 20 Hz to 1 MHz, and from 0.20 Hz to 1 MHz, respectively. Our modeling shows that the effect of mineral composition can appear superimposed on the polarization effect of the Stern layer, which coats the mineral grains.

Key words: Spectral Induced Polarization, Membrane Polarization, Zeta Potential, Mineral composition.

INTRODUCTION

Causes of induced polarization (IP) in sediments are primarily related to polarization of the Stern layer of the electrical double layer (EDL) coating mineral grains (e.g., Revil, 2012). The second cause of IP is the membrane polarization produced by the mobility difference or radius difference in a sequence of two pores (e.g., Marshall and Madden, 1959; Bücker and Hördt, 2013). Also, IP can be produced by the Maxwell-Wagner polarization when electrical field crosses materials of different electrical properties (e.g., Tabbagh et al., 2009). In this paper, we focus on the membrane polarization. In cases of both the mobility difference and the ion radius difference, the ion transference numbers in two pores differ from each other; therefore, an ion concentration gradient occurs when an electrical field is applied. This gradient leads to a secondary electrical field, which produces a phase shift between the electrical current and the tension. However, the same effect can occur in a case where the walls of the adjacent pores are built of different minerals, with different interface potentials, even if the radii of the two pores are equal. To the best of our knowledge, this effect has not yet been studied. In this paper, we analytically investigate its properties.

THEORY

The theory of membrane polarization was first proposed by Marshall and Madden (1959). They postulated that the membrane polarization is produced by a concentration gradient resulting from an external electrical field along a sequence of pores with different ion mobility values. Fridrikhsberg and Sidorova (1961) and Kormiltsev (1963) proposed a different explanation of the membrane polarization, based on a difference in concentration of cations and anions in wide and narrow pores. Recently, Bücker and Hördt (2013) modified the Marshall and Madden's theory to explicitly include the chemical parameters (zeta potential and partition coefficient), as well as the textural ones (pores radius and length). In this paper, we use the latter theory as a basis. We assume that ion concentrations in a cylindrical pore system (c_p and c_n) in the directions perpendicular and parallel to the pore axis, are independent of each other,

$$c_{p,n}(x,r) = c_o(x) \cdot b_{p,n}(r) , \quad (1)$$

where $c_0(x)$ is the concentration along the pore far from the pore walls in Mol·m³, $b_{p,n}(r)$ describes variations of the dimensionless concentration across the pores, indices p and n stand for cations and anions, respectively. The current density averaged by the pore section is as follows,

$$\bar{j}_{p,n} = -F \frac{\mu_{p,n} \bar{b}_{p,n} k_B T}{e} \frac{\partial c_0(x)}{\partial x} + F \mu_{p,n} \bar{b}_{p,n} c_0(x) E \ , \qquad (2)$$

where $F = 96\,485$ is the Faraday constant in C·Mol^{-1}, $e = 1.602 \cdot 10^{-19}$ is the elementary charge in C, $\mu_{p,n} = \frac{D_{p,n} e}{k_B T}$ is the ion mobility in m^2(V·s)$^{-1}$, $D_{p,n}$ is the ion diffusion coefficient in m^2·s^{-1}, $k_B = 1.38 \cdot 10^{-23}$ is the Boltzmann constant in J·C^{-1}, E is the electrical field in V·m^{-1}, and

$$\bar{b}_{p,n} = \frac{2}{r^2} \int_0^r b_{p,n}(\rho) \rho d\rho \qquad (3)$$

is the dimensionless concentration of ions averaged by section of the pore with radius r (ρ being the cylindrical coordinate). As was shown by Bücker and Hördt (2013), Eq. (2) is identical to Eq. (6) of Marshall and Madden (1959); therefore, their solution is applicable.

However, the general form of the transference numbers, $t_{p,n}$, includes not only the ion mobility (Marshall and Madden, 1959) but also the average ion concentrations (e.g., Bücker and Hördt, 2013):

$$t_p = \frac{\mu_p \bar{b}_p}{\mu_p \bar{b}_p + \mu_n \bar{b}_n} \qquad (4)$$

$$t_n = \frac{\mu_n \bar{b}_n}{\mu_p \bar{b}_p + \mu_n \bar{b}_n} \ . \qquad (5)$$

Therefore, $t_{p,n}$ depend on the pore radii (see Eq. (1)). For simplicity, we consider $\mu_p = \mu_n$ and we focus on the difference in $\bar{b}_p$ and $\bar{b}_n$ in the EDL. To obtain $\bar{b}_{p,n}$ values, first the potential in the diffuse layer must be calculated:

$$\varphi(\rho) = \varsigma \frac{J_0(ik\rho)}{J_0(ikr)} , \qquad (6)$$

where ς is the zeta potential in V, $J_0(x)$ is the zero order Bessel function, $i = \sqrt{-1}$, $k = (\lambda_D)^{-1}$ in m^{-1}, $\lambda_d = \sqrt{\frac{\varepsilon \varepsilon_0 k_B T}{2 c_0 e F}}$ is the Debye length in m, $\varepsilon = 80$ is the dimensionless water relative permittivity, and $\varepsilon_0 = 8.54 \cdot 10^{-12}$ is the vacuum permittivity in F·m^{-1}.

The difference in zeta potential values in a sequence of two pores of the same radius can occur if the pores walls are built of different materials, with different interface potential values. An example can be a carbonate mineral in contact with silicate or alumosilicate. For silicates and alumosilicates, the zeta potential values (at pH about 7) are usually between -20 and -80 mV, depending on the water salinity (e.g., Revil 2003, Leroy and Revil 2004). For carbonate minerals, the zeta potential values are significantly lower in absolute values (e.g., Guichet *et al.*, 2006), and can approach zero. Wu *et al.* (2010) argued that "calcium carbonates in thermodynamic

equilibrium with pore fluid produce a negligible SIP response due to very small surface charges".

The ion concentration distributions in the diffuse layer along the pores radius are calculated,

$$b_{p,n} = \exp\left(\pm \frac{e \varphi(\rho)}{k_B T} \right) , \qquad (7)$$

and numerically integrated by the pores section (Eq. (3)). According to Bücker and Hördt (2013), we include the Stern layer contribution to calculate the ion concentration in the pores:

$$\tilde{b}_p = \frac{\bar{b}_p - f_p}{1 - f_p} , \qquad (8)$$

where f_p is the partition coefficient defined as the ratio between the Stern layer charge density and the whole EDL charge density (e.g., Revil, 2012). Finally, the impedance of the pore sequence is calculated according to the Marshall and Madden (1959) equation,

$$Z(\omega) = \frac{L_1}{\mu_{p1} \bar{b}_{p1} c_0 F}(t_{p1} + \frac{B}{A} t_{p2} +$$

$$+ \frac{(S_2 - S_1)^2}{\frac{X_1(\omega) S_1}{t_{p2}^2 \tanh(X_1(\omega))} + \frac{A}{B} \frac{X_2(\omega) S_2}{t_{p1}^2 t_{p2} \tanh(X_2(\omega))}}) , \qquad (9)$$

where ω is the angular frequency, L_1 is the length of the pore in m, $B = \frac{\tilde{b}_{p1}}{\bar{b}_{p2}}$, $A = \frac{L_1}{L_2}$, $S_{1,2} = \frac{t_{n1,2}}{t_{p1,2}}$, and $X_{1,2}(\omega) = \left(\frac{i\omega}{2 D_p t_{n1,2} \bar{b}_{p1,2}} \right) \frac{L_{1,2}}{2}$ are dimensionless quantities, and indices "1" and "2" refer to the pore with smaller ("passive") and greater ("active") interface potential, respectively.

MODELING

We model two parameters of spectral IP: maximum values of the phase shift, ϕ_{max}, and the corresponding peak phase frequency. The calculations are carried out for two values of the free pore water salinity, namely 1 Mol·m^{-3} and 10 Mol·m^{-3}, and for the pore radius values of 10^{-8}, 10^{-7}, and 10^{-6} m. We consider the ion diffusion coefficient to be constant for cations and anions, $D_p = D_n = 10^{-9}$ m^2·s^{-1}, and the zeta potential to be -75 mV. For active pore we apply the average partition coefficient obtained for clays, $q_p = 0.85$ (see Revil, 2012, his Fig. 3). We calculate the phase shift, as well as the peak frequency, f_c, as functions of the pore lengths. We present the data as the maps of calculated values vs. pore lengths (Fig. 1). In the maps, we also show values of three peak frequencies corresponding to two cases: (1) common limits of the spectral IP measurements (between 1 mHz and 20 kHz); and (2) limits of the wideband (see e.g., Volkmann and Klitzsch, 2015) measurements (between 1 mHz and 1MHz).

DISCUSSION

The maximum values of ϕ_{max} are found to be between 13 and 210 mrad depending on the ion concentration in free water and the pore radius (Fig. 1). The values increase with the decrease of the water salinity and the pore radius. This effect reflects the growth of the Debye length and, therefore, of the diffuse layer thickness relative to the pore size. The maximum values of ϕ_{max} correspond to the case of equal pore lengths. The behavior of f_c is very similar in all cases (shown in Fig. 1 for the case of the water salinity of 1 Mol·m^{-3} and the pore radius of 10^{-8} m only), which indicates that the main parameter determining f_c is the pore length. The maximum curvature of the isocurves of f_c corresponds to the case where $L_1 = L_2$.

For ϕ_{max}, we establish a threshold of 10 mrad, considering that values below it would be under the detection limit because of the capacitive coupling and Maxwell-Wagner polarization. We assume that the pores can be elongated, i.e., their aspect ratio (L/d) can achieve the characteristic values of 10 and 50 (see Weber at al., 2014 for clay particles). In the phase maps, we show areas corresponding to these aspect ratio values by hatch. These hatches are also limited to isocurves corresponding to the higher frequency limit of the broadband IP measurements (1 MHz).

Analysis of the maps shows that, for the narrowest pores (10^{-8} m), the effect is very strong (up to ~210 mrad), and can be detected in the frequency range between 1.6 kHz and 1 MHz. For larger pores (10^{-7} and 10^{-6} m), the effect is less pronounced (up to 130 and 13 mrad, respectively), and can be detected starting from the frequency values of 20 and 0.2 mrad, respectively. Therefore, it can be observed within the range of the common IP measurements. Our analysis shows that the studied effect, especially for the pore radii of 10^{-7} and 10^{-6} m, can be superimposed on the polarization effect of the Stern layer coating the mineral grains.

CONCLUSIONS

Our modeling shows that the IP effect of mineral composition can be significant. It can be detected in cases of fresh water, large values of the zeta potential difference between the adjacent pores, and in elongated pores. For three modeled pore radius values, f_c can be in the range between 1.6 kHz and 0.2 Hz; therefore, it can be observed in the range of typical spectral IP measurements, and can be superimposed on the polarization effect of the Stern layer coating the mineral grains.

ACKNOWLEDGMENT

REFERENCES

Bücker, M., and Hördt, A., 2013, Analytical modelling of membrane polarization with explicit parametrization of pore radii and the electrical double layer: Geophysical Journal International, DOI: 10.1093/gji/ggt136.

Guichet, X., Jouniaux, L., and Catel, N., 2006, Modification of streaming potential by precipitation of calcite in a sand–water system: laboratory measurements in the pH range from 4 to 12: Geophysical Journal International, 445–460, DOI: 10.1111/j.1365-246X.2006.02922.x

Fridrikhsberg, D.A., and Sidorova, M.P., 1961, Issledovanie sviazi yavlenia vyzvannoi polarizatsii s electrokineticheskimi svoistvami kapillarnyh sistem (A study of relationship between the induced polarization phenomenon and the electro-kinetic properties of capillary systems): Vestnik Leningradskogo Universiteta, Seria Chimia 4, 222– 226 (In Russian).

Kruschwitz, S., Binley, A., Lesmes, D., and Elshenawy, A., 2010, Textural controls on low-frequency electrical spectra of porous media: Geophysics, vol. 75, issue 4, p.113, DOI: 10.1190/1.3479835

Kormiltsev, V.V., 1963, O vozbuzdenii i spade vyzvannoi polarizatsii v kapillarnoi srede (On excitation and decay of Induced Polarization in capillary medium): Izvestia AN SSSR, Seria Geofizicheskaya (Solid Earth Physics) 11, 1658– 1666 (In Russian).

Marshall, D.J., and Madden, T.K., 1959, Induced polarization, a study of its causes: Geophysics 24 (1), 790– 816.

Revil, A., 2012, Spectral induced polarization of shaly sands: Influence of the electrical double layer: Water Resources Research, 48, p. 2517, DOI:10.1029/2011WR011260.

Leroy, P., and Revil, A, 2004, A triple-layer model of the surface electrochemical properties of clay minerals: Journal of Colloid and Interface Science, 270, 371–380, DOI:10.1016/j.jcis.2003.08.007.

Revil, A., Naudet, V., Nouzaret, J., and Pessel, M., 2003, Principles of electrography applied to self-potential electrokinetic sources and hydrogeological applications: Water Resources Research 39, 1114, DOI:10.1029/2001WR000916.

Tabbagh, A., Cosenza, P., Ghorbani, A., Guérin, R., and Florsch, N., 2009, Modelling of Maxwell–Wagner induced polarisation amplitude for clayey materials: Journal of Applied Geophysics, 67, 109–113, DOI:10.1016/j.jappgeo.2008.10.002.

Weber, C., Heuser, M., and Stanjek, H., 2014, A collection of aspect ratios of common clay minerals determined from conductometric titrations: Clay Minerals, 49, 495–498, DOI: 10.1180/claymin.2014.049.3.10.

Volkmann, J., and Klitzsch, N., 2015, Wideband impedance spectroscopy from 1 mHz to 10 MHz by combination of four- and two-electrode methods: Journal of Applied Geophysics, 114, 191–201, http://dx.doi.org/10.1016/j.jappgeo.2015.01.012.

Wu, Y., Hubbard, S. S., Ajo Franklin, J. B., Williams, K. H., 2010, Pore fluid chemistry and spectral induced polarization signatures of calcium carbonate: American Geophysical Union, Fall Meeting 2010, Abstract #NS33A-06.
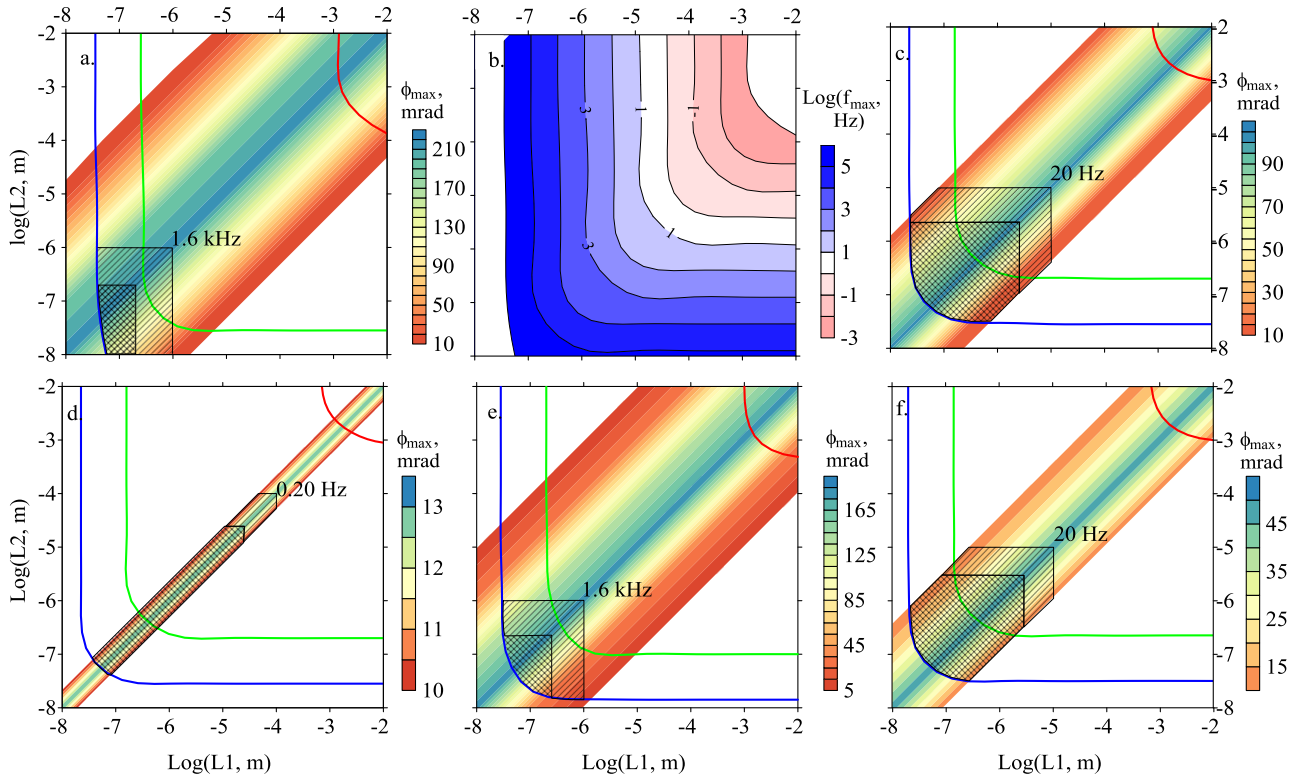
Figure 1. Maximum phase shift (a, c, e, d, f) and peak frequency (b) as functions of the passive (L1) and active (L2) pore length. The phase shift threshold is 10 mrad. Colored lines in panels a, c, d, e, f are peak frequency values: red – 10 mHz, green – 20 kHz, and blue – 1 MHz. Cross-hatch shows areas when the pore aspect ratio, *L/d*, is less than 10, hatch – less than 50. Numbers indicate the minimum peak frequency values, corresponding to the assumed ratio. Panels a, b, c, d: water salinity is 1 Mol·m⁻³; e, f - 10 Mol·m⁻³; panels a, b, e: *r* is 10⁻⁸ m; c, f : *r* is 10⁻⁷ m; d: *r* is 10⁻⁶ m.

IP2016/4th International Workshop on Induced Polarization

Evaluation of low frequency polarization models using well characterized sintered porous glass samples

Jan Volkmann

Applied Geophysics and Geothermal Energy,
E.ON Energy Research Center
RWTH Aachen University
Mathieustr. 10, 52074 Aachen, Germany
jvolkmann@eonerc.rwth-aachen.de

Norbert Klitzsch

Applied Geophysics and Geothermal Energy,
E.ON Energy Research Center
RWTH Aachen University
Mathieustr. 10, 52074 Aachen, Germany
nklitzsch@eonerc.rwth-aachen.de

SUMMARY

We assess the results of published theoretical and experimental findings regarding low frequency rock polarization for a reference system, consisting of sintered porous glass samples. Thereby, we benefit from well characterized samples, which allow for direct tests of theoretical predictions and empirical relations. We find that: (1) The correlation $\sigma''{\sim}S_m$ is stronger than $\sigma''{\sim}S_{por}$ for a wide range of fluid conductivities and frequencies above 1 Hz. (2) Correlation coefficients for the imaginary conductivity to inner surface area relations are strongly frequency dependent. (3) Normalized chargeability, obtained by fitting a Cole–Cole model to the spectral data, provides a fair alternative to single frequency information. (4) Salinity dependence of proportionality factors $a_1 = S_m/\sigma''$ and $a_2 = S_{por}/\sigma''$ due to a salinity dependent partition coefficient is confirmed qualitatively. Quantitative theoretic predictions of a_1 or a_2 fail due to the assumption of non-reduced Stern layer mobility for clay free silica. (5) Earliest grain size related models provide the best quantitative estimate of relaxation time. (6) Results agree well with published data for sands and sandstones with respect to (i) quantitative estimates of a_1 or a_2 and (ii) influences of rock structural parameters on relaxation time.

The study introduced here was published by Volkmann and Klitzsch (2016).

Key words
-Impedance spectroscopy
-Spectral induced polarization
-Low frequency polarization models

INTRODUCTION

It is generally argued that low frequency electrical polarization is caused by charged mineral surfaces leading to an electrical double layer (EDL) in the vicinity of the inner rock surface. The counterions in the EDL, which compensate the surface charges of the rock in the electrolyte, interact with an external electric field and cause the polarization of rocks, i.e. lead to a frequency dependent complex conductivity of water saturated rocks. For rocks containing ore minerals or electronic conductors an additional polarization process occurs, often named electrode polarization (Pelton et al., 1978; Wong, 1979), which is not considered here. For a quantitative description of the complex, frequency dependent conductivity of ore-free rocks partially competing theories were published (e.g. Revil and Florsch, 2010; Revil, 2012; Bücker and Hördt, 2013a). Moreover, an extensive database for a wide range of

rock samples has been analysed recently to verify theoretical and empirical relations (e.g. Weller et al., 2010; Weller et al., 2013). We assess the results of these published theoretical and experimental findings using a reference system, consisting of sintered porous glass samples.

In particular, we address the following questions:

1. Is the of correlation $\sigma'' \sim S_m$ of the imaginary part of conductivity to specific surface area per unit mass stronger than the correlation $\sigma'' \sim S_{por}$ of imaginary part of conductivity to specific surface area per unit pore volume?
2. Does this correlation depend on salinity or frequency?
3. Is there an advantage in frequency dependent measurement, e.g. by correlating normalized chargeability $m_n \sim S_m$ and $m_n \sim S_{por}$ instead of imaginary part of conductivity $\sigma'' \sim S_m$ and $\sigma'' \sim S_{por}$ to specific surface area?
4. Are the quantitative relations $\sigma'' = a_1 S_{por}$ and $\sigma'' = a_2 S_m$ valid, using plausible model parameters?
5. Which model provides the best quantitative estimate for Cole-Cole relaxation time τ_{CC}?
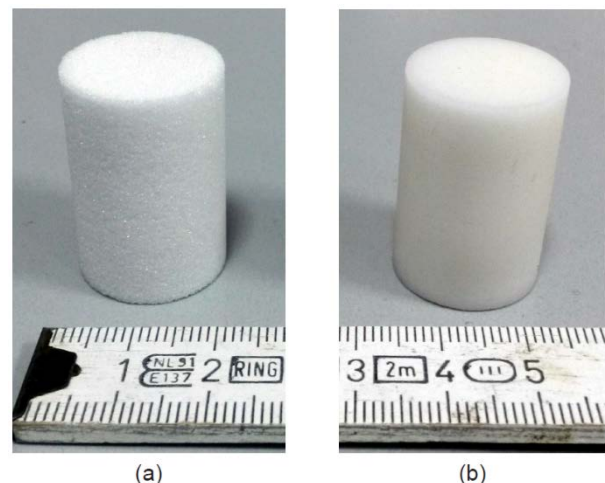
METHODS

Figure 1. Exemplary sintered porous borosilicate samples, manufactured by ROBU® Glasfilter-Geräte GmbH. (a): Dry sample with $d_{por,lm}$ = 63.25 µm (Sample P2); (b): Saturated sample with $d_{por,lm}$ = 12.65 µm (Sample P4).

We used porous borosilicate samples (Fig. 1) as an experimental reference system as described by Volkmann and Klitzsch (2016). These are sintered porous ceramics, manufactured by ROBU® Sintered Glassfilters, of pure

borosilicate 3.3 standard glass according to ISO 4793 and DIN/ISO 3585. Main advantage, regarding the purpose of this study, is their well-known chemical composition and nominal pore size, both given in the above mentioned DIN/ISO norms. We used samples with nominal pore size ranges between 0.9 µm-1.4 µm and 100 µm-160 µm. The cylindrical samples had a length of 0.03 m and diameter of 0.02 m. We provide a summary of relevant sample properties in Table 1.

Table 1. Nominal pore size d_{por} (MICP, given by ROBU® Glasfilter-Geräte GmbH, cf. ISO 4793), logarithmic mean of nominal pore size $d_{por,lm}$, logarithmic mean of (independently measured) grain diameter $d_{grain,lm}$, porosity (weighing), specific surface area S_m (BET, given by ROBU® Glasfilter-Geräte GmbH) Table modified according to Volkmann et al. (2013).

Sample ID	d_{por} / µm	$d_{por,lm}$ / µm	$d_{grain,lm}$ / µm	ϕ / %	S_m / m²g⁻¹
P1	$100-160$	126.5	316.2	32%	0.085
P2	$40-100$	63.25	158.1	30%	0.130
P3	$16-40$	25.30	63.24	44%	0.350
P4	$10-16$	12.65	31.62	39%	0.500
F_1, F_2	$4-5.5$	4.69	11.73	51%, 53%	1.200
VF_1, VF_2	$2-2.5$	2.24	5.59	46%, 41%	N/A
P5	$1.0-1.6$	1.27	3.16	54%	1.750
UF_1, UF_2, UF_3	$0.9-1.4$	1.12	2.81	46%, 48%, 51%	1.750

As described by Volkmann and Klitzsch (2015), it is advantageous to study Impedance Spectroscopy (IS) data over a wide frequency range, at least if subsequent model parameterizations shall be applied for further analysis. Thus, we follow the approach of Volkmann and Klitzsch (2015), using a combination of four- and two-electrode methods to enable wideband IS data from 1 mHz to 10 MHz. We conducted IS measurements under:

1. Variation of pore fluid salinity. We use NaCl solution in a conductivity range between $3 \cdot 10^{-4}$ Sm⁻¹ and $6 \cdot 10^{-2}$ Sm⁻¹.
2. Variation of predominant pore diameter. We use 8 different sample types with pore diameters $d_{por,lm}$ between 1.12 µm and 126.5 µm, cf. Table 1.
3. Variation of grain diameter. We use 8 different sample types with (logarithmic mean) grain diameter $d_{grain,lm}$ between 2.81 µm and 316.2 µm, cf. Table 1.
4. Variation of S_m (BET) between 0.085 m²g⁻¹ and 1.750 m²g⁻¹ (Table 1) and corresponding variation of S_{por}, cf. Table 1.

The resulting IS data were processed according to Volkmann and Klitzsch (2015) and analysed using a Cole–Cole model (e.g. Dias, 2000).

RESULTS

A main controversy is, if imaginary conductivity rather controlled by specific surface area per unit pore volume S_{por} (in m⁻¹) or specific surface area per unit mass S_m (in m²g⁻¹). In this respect, the quantitative model predictions have been made recently. Exemplary results at a selected single frequency of $f = 10$ Hz and fluid conductivity of $\sigma_f \approx 3 \cdot 10^{-4}$ Sm⁻¹ are shown in Figures 2 and 3. Here, we find a linear relation $\sigma''_{10Hz} = a_1 S_{por}$ with $a_1 = 2 \cdot 10^{-12}$ S with a correlation coefficient of $R^2 = 0.84$ and a relation $\sigma''_{10Hz} = a_2 S_m$ with $a_2 = 5.2 \cdot 10^{-9}$ S kg m⁻³ with a correlation coefficient of $R^2 = 0.94$. Thus, we find a stronger correlation of σ''_{10Hz} to S_m than to S_{por}, which is suggested from recent

Stern layer polarization models. Quantitatively, a_1 and a_2 agree with earlier experimental (sandstone sample) results, but imply a strongly reduced Stern layer mobility and/or partition coefficient.

Another open question is, if there is any advantage in frequency dependent measurements compared to single frequency information regarding S_{por}/S_m determination. To resolve this issue, we studied the quality of $\sigma'' \sim S_m$ and $\sigma'' \sim S_{por}$ relations for a set of separate frequencies between 10 mHz and 100 Hz (Fig. 4). As measure of quality, we used the correlation coefficient R^2 of the theoretically suggested linear fit. For comparison, we used the corresponding relation between normalized chargeability $m_n = m \cdot \sigma_0$ (from Cole–Cole model) and S_{por} or S_m as typical parameter of frequency dependent measurements. Examples for m_n at $\sigma_f \approx 3 \cdot 10^{-4}$ Sm⁻¹ are given in Figures 5 and 6. As a result, the correlation coefficients for σ'' are strongly frequency dependent and normalized chargeability provides a fair alternative to single frequency information.

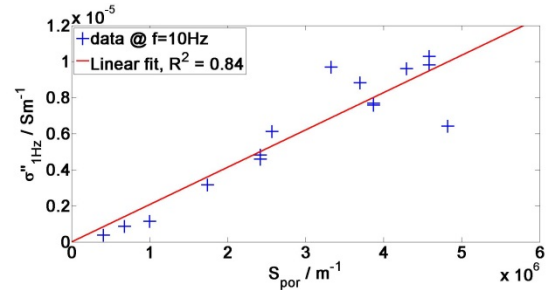**Figure 2. Dependence of imaginary conductivity $\sigma''_{10\ Hz}$ (blue crosses) on specific surface area per unit pore volume S_{por} (from BET, Table 1 and equation 22). A linear correlation $\sigma''_{10Hz} = a_1 \cdot S_{por}$ (red line) with $a_1 = 2.1 \cdot 10^{-12}$ S is found ($R^2 = 0.84$).**
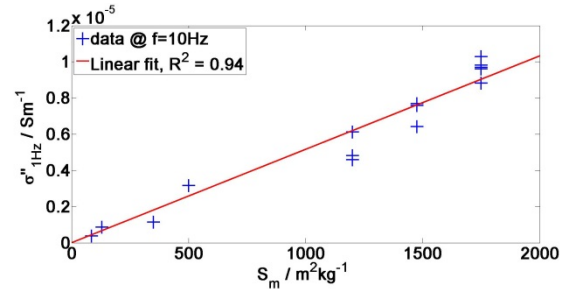

Figure 3. Dependence of imaginary conductivity σ''_{10Hz} (blue crosses) on specific surface area S_m (from BET, Table 1). A linear correlation $\sigma''_{10Hz} = a_2 \cdot S_m$ (red line) with $a_2 = 5.2 \cdot 10^{-9}$ S kg m⁻³ is found ($R^2 = 0.94$).
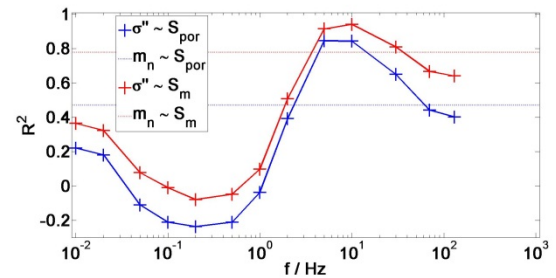

Figure 4. Dependence of correlation coefficient R^2 on frequency f for $\sigma'' \sim S_m$ (red) and $\sigma'' \sim S_{por}$ (blue) relation at a fluid salinity of $\sigma_f \approx 3 \cdot 10^{-4}$ Sm⁻¹. Dotted lines show R^2 for the corresponding $m_n \sim S_m$ and $m_n \sim S_{por}$ relations.

The slight difference in a_1 and a_2, e.g. compared to the data of Weller et al. (2010), may be explained by a salinity dependent partition coefficient as postulated by Leroy et al. (2008).

To resolve this issue, we repeated our studies at the three additional fluid conductivities. We confirm the expected increase in a_1 and a_2 with salinity (Figs. 7 and 8), except for the highest salinity. Normalized chargeability m_n increases with salinity up to the highest salinity. However, the salinity and pH dependent partition coefficient is not sufficient to explain the data quantitatively, if we do not assume a reduced counterion mobility at the same time.

Numerous hypotheses exist on the predominant influence on relaxation time and/or characteristic time τ. As an advantage of our reference system, e.g. compared to the similar studies of Revil et al. (2012), we have independent information about pore and grain diameters (Table 1). A power law fit leads to a dependence $\tau_{CC} = 1.8 \cdot 10^5 \cdot d_{por,lm}^{1.3 \pm 0.2}$ on logarithmic mean $d_{por,lm}$ of nominal pore size (Fig. 9). Similarly, we find a relation of $\tau_{CC} = 5.3 \cdot 10^4 \cdot d_{grain,lm}^{1.3 \pm 0.2}$ between relaxation time τ_{CC} and logarithmic mean $d_{grain,lm}$ of the independently measured grain diameters (Fig. 10). These are results are in good agreement with earlier results (cf. Volkmann and Klitzsch, 2010, their Table 1). Following theoretic suggestions of a quadratic model, we find $\tau_{CC} = (7.2 \pm 3.2) \cdot 10^8 \cdot d_{por,lm}^2$ and $\tau_{CC} = (1.2 \pm 0.5) \cdot 10^8 \cdot d_{grain,lm}^2$. These results support earliest grain size related model approaches (Schwarz, 1962) under the precondition of a non-reduced diffusion coefficient.
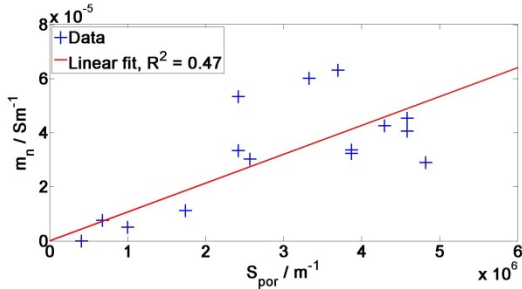

Figure 8. Dependence of the slope a_1 at f_{opt} = 10 Hz and the slope a_1 of the linear $m_n \sim S_{por}$ relation on fluid conductivity σ_f.

Figure 8. Dependence of the slope a_2 at f_{opt} = 10 Hz and the slope a_2 of the linear $m_n \sim S_m$ relation on fluid conductivity σ_f.

Figure 9. Dependence of Cole-Cole relaxation time (blue crosses) on pore diameter $d_{por,lm}$. A dependence of $\tau_{CC} = 1.8 \cdot 10^5 \cdot d_{por,lm}^{1.3 \pm 0.2}$, R^2 = 0.76 (red line) on pore diameter is found (Volkmann et al., 2013). A fit with fixed exponents leads to $\tau_{CC} = (7.2 \pm 3.2) \cdot 10^8 \cdot d_{por,lm}^2$, R^2 = 0.31 (green line).

Figure 5. Dependence of normalized chargeability m_n (blue crosses) on specific surface area per unit pore volume S_{por} (from BET, Table 1 and equation 22). A weak linear correlation $m_n = a_1 \cdot S_{por}$ (red line) with $a_1 = 1.07 \cdot 10^{-11}$ S is found (R^2 = 0.47).
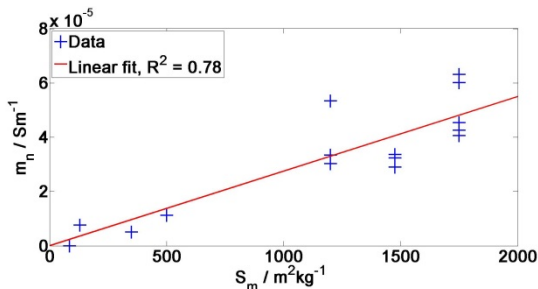

Figure 6. Dependence of normalized chargeability m_n (blue crosses) on specific surface area S_m (from BET, Table 1). A linear correlation $m_n = a_2 S_m$ (red line) with $a_2 = 2.75 \cdot 10^{-8}$ S kg m^{-3} is found (R^2 = 0.78).
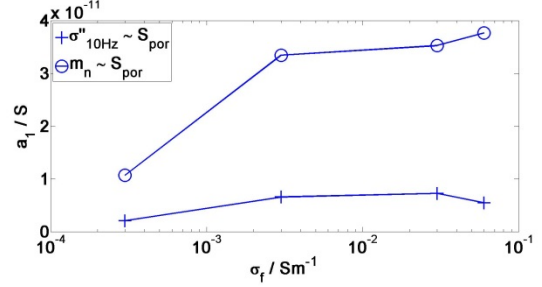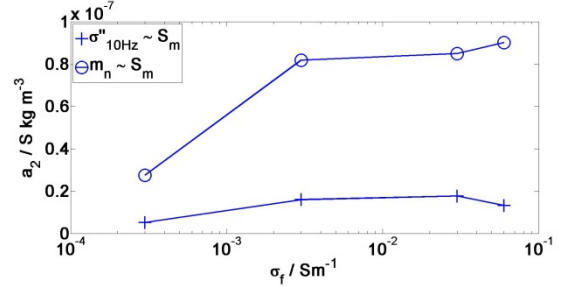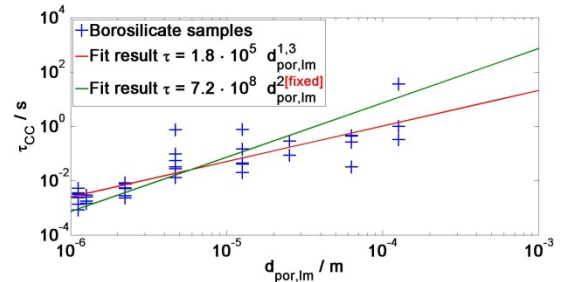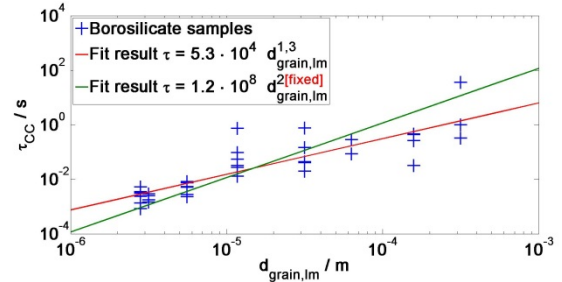

Figure 10. Dependence of Cole-Cole relaxation time (blue crosses) on grain diameter $d_{grain,lm}$. A dependence of $\tau_{CC} = 5.3 \cdot 10^4 \cdot d_{grain,lm}^{1.3 \pm 0.2}$, R^2 = 0.76 (red line) on grain diameter is found. A fit with fixed exponents leads to $\tau_{CC} = (1.2 \pm 0.5) \cdot 10^8 \cdot d_{grain,lm}^2$, R^2 = 0.31 (green line).

CONCLUSIONS

Regarding the recent developments in Stern layer polarization models, we find ambiguous results from our reference sample study. We can confirm the stronger correlation of imaginary part of conductivity to specific surface area (per unit mass), i.e. $\sigma'' \sim S_{\mathrm{m}}$, compared to specific surface area per unit volume, i.e. $\sigma'' \sim S_{\mathrm{por}}$, for a wide range of fluid conductivities and frequencies above 1 Hz. We find strongly frequency dependent correlation coefficients for both relations.

A normalized chargeability m_{n} to S_{m} correlation provides a fair alternative to the σ'' to S_{m} correlation, since the frequency f_{opt} of optimal correlation of imaginary part of conductivity is typically unknown. We can qualitatively confirm the salinity dependence of the corresponding proportionality factor, arising from the salinity dependence of the partition coefficient parameter of recent Stern layer polarization models. However, quantitative theoretic suggestions for these factors do not agree with experimental evidence. In particular, the assumption that Stern layer mobility of counter ions is not reduced for TYPE II (clay free silica) material is incorrect with respect to the $\sigma'' \sim S_{\mathrm{m}}$ relation, if we assume the general model framework being correct and vice versa. On the other hand, exactly this assumption of a non-reduced mobility leads to good agreement for the relaxation time of the reference samples. Thus, different mobilities, e.g. bulk fluid versus Stern layer mobility, might be responsible for the different studied quantities. In conclusion, recent Stern layer polarization models comprise promising ideas on rock polarization physics. Nevertheless, in terms of quantitative relations we recommend further enhancement.

Membrane polarization models on the other hand are very dependent on the particular geometric model conditions, predicting only the particular model impedance Z instead of conductivity σ. Nevertheless, these models prove falsifiability providing experimentally accessible differences to Stern layer polarization. In particular, relations between relaxation time and grain sizes (Stern layer polarization) or one the numerous imaginable pore size quantities (membrane polarization) have the potential to improve understanding. Unfortunately, we could not resolve any qualitative difference between the influence of independently measured (logarithmically mean) pore diameter and grain size using a power law fit on the reference sample data. Subsequently applying all sufficiently simple membrane polarization approaches, we could not challenge the earliest grain size related approach in a quantitative estimate of quadratic relaxation time behavior, but have to cope with numerous limiting assumptions. Thus, there is the potential to further improve these approaches in terms of universality, e.g. deduce the complex conductivity response, and reliable quantitative predictions for simple experimental cases.

ACKNOWLEDGMENTS

REFERENCES

Bücker, M., Hördt, A., 2013a. Analytical modelling ofmembrane polarization with explicit parametrization of pore radii and the electrical double layer. Geophys. J. Int.

Dias, C., 2000. Developments in a model to describe low-frequency electrical polarization of rocks. Geophysics 65 (2), 437–451.

Leroy, P., Revil, A., Kemna, A., Cosenza, P., Ghorbani, A., 2008. Complex conductivity of water-saturated packs of glass beads. J. Colloid Interface Sci. 321 (1), 103–117.

Pelton, W., Ward, S., Hallof, P., Sill, W., Nelson, P., 1978. Mineral discrimination and removal of inductive coupling with multifrequency IP. Geophysics 43 (3), 588–609.

Revil, A., 2012. Spectral induced polarization of shaly sands: influence of the electrical double layer. Water Resour. Res. 48 (2).

Revil, A., Florsch, N., 2010. Determination of permeability from spectral induced polarization in granular media. Geophys. J. Int. 181, 1480–1498.

Schwarz, G., 1962. A theory of the low-frequency dielectric dispersion of colloidal particles in electrolyte solution. J. Phys. Chem. 66 (12), 2636–2642

Volkmann, J., Klitzsch, N., 2010. Frequency-dependent electric properties of microscale rock models for frequencies from one millihertz to ten kilohertz. Vadose Zone J. 9 (4), 858–870.

Volkmann, J., Klitzsch, N., Mohnke, N., Schleifer, N., 2013. Rock properties influencing impedance spectra (IS) studied by lab measurements on porous model systems (Extended abstract), SCA2013-A039. Proceedings: International Symposium of the Society of Core Analysts held in Napa Valley, California, USA, pp. 419–424 (16–19 September, 2013).

Volkmann, J., Klitzsch, N., 2015. Wideband impedance spectroscopy from 1 mHz to 10 MHz by combination of four- and two-electrode methods. J. Appl. Geophys. 114, 191–201.

Volkmann, J., Klitzsch, N., 2016. Evaluation of low frequency polarization models using well characterized sintered porous glass samples. J. Appl. Geophys. 124 (2016): 39-53.

Weller, A., Slater, L., Nordsiek, S., Ntarlagiannis, D., 2010. On the estimation of specific surface per unit pore volume from induced polarization: a robust empirical relation fits multiple data sets. Geophysics 75 (4), WA105–WA112.

Weller, A., Slater, L., Nordsiek, S., 2013. On the relationship between induced polarization and surface conductivity: implications for petrophysical interpretation of electrical measurements. Geophysics 78 (5), D315–D325.

Wong, J., 1979. An electrochemical model of the induced-polarization phenomenon in disseminated sulfide ores. Geophysics 44 (7), 1245–1265.

SIP of the three-phase system CO$_2$-brine-sand under reservoir conditions

Jana H. Börner
TU Bergakademie Freiberg
Institute of Geophysics and
Geoinformatics
Gustav-Zeuner-Str. 12
D-09599 Freiberg
jana.boerner@geophysik.tu-freiberg.de

Volker Herdegen
TU Bergakademie Freiberg
Institute of Thermal, Environmental and Natural Products Process Engineering

Jens-Uwe Repke
TU Bergakademie Freiberg
Institute of Thermal, Environmental and Natural Products Process Engineering

Klaus Spitzer
TU Bergakademie Freiberg
Institute of Geophysics and
Geoinformatics

SUMMARY

We present laboratory measurements of the spectral complex electrical conductivity of water-bearing sand samples during exposure to and flow-through by carbon dioxide. Pressures up to 300 bar and temperatures up to 80°C were applied. Steady-state experiments serve for investigating the physicochemical equilibrium of the fluid phases. Dynamic experiments aim at analysing the impact of partial saturation and chemical interaction on complex conductivity.

The steady-state dissolution experiments show that besides the conductivity-increasing dissociation a second opposing process may be observed, which results in a significant reduction of conductivity at high salinities despite the added CO$_2$. We explain our observations with a semi-analytical formulation for the electrical conductivity taking into account the interactions of ion and neutral species.

A significant reduction of saturation is observed during CO$_2$ flow and drainage. The spectral complex conductivity maps both changes in saturation and chemical interaction. Including the semi-analytical correction for porewater conductivity allows for a good reconstruction of saturation from SIP-measurements. Additionally we get access to an indicator for changes of the inner surface area, which is related to mineral dissolution or precipitation processes.

Key words: SIP, reactive gas, high pressure, monitoring

INTRODUCTION

The electrical rock conductivity is a sensitive indicator for CO$_2$ migration processes (e.g. Börner et al., 2013). Due to their sensitivity to the pore fluids, electric and electromagnetic methods bear a great potential for monitoring CO$_2$ injections and leakages. However, CO$_2$ is a reactive gas which massively interacts with other pore fluids. Therefore, classic relationships do not necessarily apply to the three-phase system sand / pore water / CO$_2$. We investigate the system with the spectral induced polarization method (SIP) at geologically relevant pressure and temperature conditions to get additional information on physical and chemical processes at the grain-water interface and evaluate the monitoring capabilities.

THEORY

The electrical rock conductivity $\sigma_{\text{rock}}^*(\omega)$ is generally complex and frequency dependent.

$$\sigma_{\text{rock}}^*(\omega) = \sigma_{\text{rock}}' + i\sigma_{\text{rock}}'' \tag{1}$$

Complex quantities are marked with an asterisk, prime denotes the real and double prime the imaginary part, ω is the angular frequency.

Several conductance mechanisms contribute to rock conductivity. They occur in parallel and are differently affected by, e.g., salinity and saturation:

$$\sigma_{\text{rock}}^* = \sigma_{\text{electrolyte}} + \sigma_{\text{interface}}^* \tag{2}$$

The electrolytic conductivity $\sigma_{\text{electrolyte}}$ describes pure ohmic conduction caused by ions moving freely in the liquid. It contributes to the real part of conductivity only and is covered by Archie's law (Archie, 1942). The interface layer, which forms at the contact of silicate grain and pore water, gives rise to an interface conductivity $\sigma_{\text{interface}}^*$ acting similar to a lossy capacitor. It contributes to both real and imaginary part of conductivity and underlies multiple dependencies as well (e.g. Vinegar & Waxman, 1984; Revil & Skold, 2011; Skold et al., 2011; Weller & Slater, 2012). Especially changes in pore water conductivity σ_w and water saturation but also pH variations strongly influence all conductivity components.

CO$_2$ is a reactive gas and dissolves in water in great amounts depending on pressure, temperature and salinity (e.g. Duan et al. 2006). A small portion of the dissolved CO$_2$, which forms carbonic acid, dissociates in two steps:

$$\begin{aligned} CO_2 + H_2O &\rightleftharpoons H^+ + HCO_3^- \\ HCO_3^- &\rightleftharpoons H^+ + CO_3^{2-} \end{aligned} \tag{3}$$
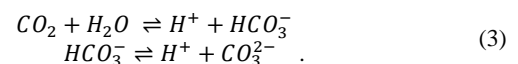
Since the dissociation of CO$_2$ adds considerable amounts of charged species to the fluid, the pore water conductivity should be affected by the presence of CO$_2$ in pore space. Generally the electrolytic conductivity of an aqueous solution consists of contributions of each charged species i :

$$\sigma_w = \sum_{i=1}^{n} \Lambda_i \gamma_i c_i \tag{4}$$

Here, c_i is the concentration of species i and Λ_i is the molar conductivity. The activity coefficient γ_i describes the change of ion mobility due to inter-species interactions:

$$\ln(\gamma_i) = \ln(\gamma_i^o) + f(c_{j \neq i}) \tag{5}$$

Where γ_i^o is the activity coefficient of a solution of species i only and $f(c_{j \neq i})$ is a function of all other species present in the solution.

METHOD AND RESULTS

Laboratory set-up and procedure

All experiments presented in this study were carried out with an experimental set-up based on the apparatus of Börner et al. (2013). It is possible to measure CO_2 concentration with a wet chemical analysis method. Thereby, a defined sample volume can be taken and the concentration may be determined by back titration. Core of the experimental set-up is a steel autoclave (see Fig. 1), in which a maximum pressures of 300 bar at a maximum temperature of 80°C is generated. The autoclave can be equipped with different measuring cells. Static conditions or CO_2 flow through the system may be realized.
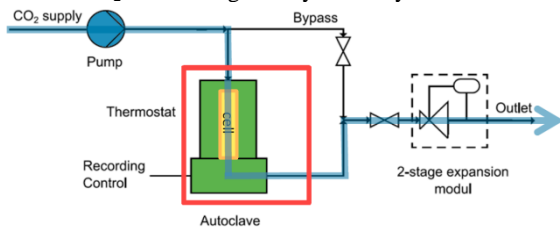

Figure 1. Laboratory set-up with steel autoclave (green) in a hot-air cabinet (red). The measuring cell (yellow) may be adapted to the type of experiment. CO₂ flow is plotted in blue.

Two types of experiments have been carried out: steady-state dissociation and dynamic flow experiments. For static dissociation experiments, a salt solution of known salinity was filled in a 0.75 l measuring cell placed inside of the autoclave. The measuring cell completely consists of glass. Current electrodes are placed at the top and bottom of the measuring cell in form of wire meshes. 6 equidistant wire rings serve as potential electrodes. All electrodes were made of platinized platinum. For 135 pressure/ temperature / salinity / species combinations the equilibrium solution conductivity σ_w was determined. If related to the initial solution conductivity σ_w^o we get the conductivity contrast due to CO_2:

$$\sigma_w^{\mathrm{norm}} = \frac{\sigma_w}{\sigma_w^o} \qquad (6)$$

For the dynamic flow experiments a different measuring cell is used, which is equipped with a permeable bottom to allow flow through the sample. The cell is filled with an initially fully saturated clean sand sample and the whole system is put under constant pressure and temperature. Then, pore water is driven out of the sample by a CO_2 mass flow. During depressurization at the end of each experiment, no further drainage takes place. The spectral complex conductivity of the sample is monitored throughout the whole process. Repeated flow experiments have been carried out for 8 pressure / temperature / salinity combinations representing different depths within the Earth's interior.

Results

The static dissociation experiments revealed a partially unexpected behaviour (see Fig. 2). For small salinities, we observe an increase in the electrical pore water conductivity when pressure increases (see left subplot in Fig. 2), which strongly

depends on the solution salinity. This is the expected effect, since the additional ions originating from the dissociation of carbonic acid contribute to the solution conductivity.

However, when higher salinities are considered this effect is completely diminished. For increasingly saline solutions it is even overcompensated (right subplot in Fig. 2). To explain these observations we present a semi-analytical model, which is formulated in terms of a correction factor σ_w^{norm} (Eq. 6) and is based on Eqs (4) and (5) (see solid lines in Fig. 2):

$$\sigma_w^{\mathrm{norm}} = \frac{\Lambda_{\mathrm{NaCl}}\gamma_{\mathrm{NaCl}}c_{\mathrm{NaCl}} + \Lambda_{\mathrm{CO2}}\gamma_{\mathrm{CO2}}c_{\mathrm{CO2(dis)}}}{\Lambda_{\mathrm{NaCl}}\gamma_{\mathrm{NaCl}}^o\, c_{\mathrm{NaCl}}} \; . \qquad (7)$$

The remaining unknown quantities in Eq. (7) are derived by a least-squares inversion (for details, see Börner et al. 2015). Depending on salinity and the environmental conditions, either the additional conductivity from the dissociated CO_2 or the decreased activity coefficient of the salt component dominates the solution conductivity.
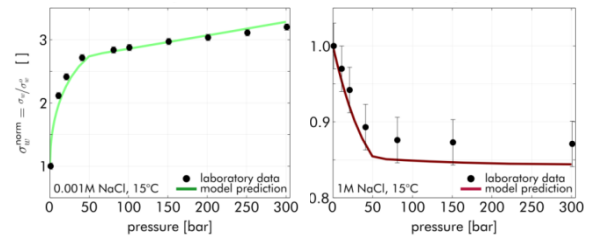

Figure 2. Conductivity contrast due to CO₂ dissociation for two salinities versus pressure (circles: measured data; 3% error bars). Solid lines represent the contrast predicted by the model (Eq. 7, Börner et al. 2015).

Fig. 3 shows the experimental conditions (top) and the complex conductivity (bottom, in terms of real and imaginary part) for one flow experiment with nitrogen (N_2, non-reactive) and one experiment with CO_2 (reactive). Both real and imaginary part drop due to the drainage, as expected. The difference between the N_2 and the CO_2 experiment is caused by the reactive nature of CO_2. The drop in the real part is dampened by the dissociation (cf. also Fig. 2, left). The disproportionate drop in the imaginary part may be associated with the low pH environment. We describe this effect with a second correction term $\sigma_{\mathrm{if}}^{\mathrm{norm}}$, which is defined in analogy to σ_w^{norm}. The complex conductivity during interaction with CO_2 may than be evaluated in terms of saturation. Since the imaginary part of conductivity strongly depends on the inner surface area of the porous medium (e.g. Börner et al., 1996; Weller et al., 2010) we can also deduce an indicator for the change in inner surface area. Such an indicator is of great interest during monitoring because a change in inner surface area is associated to mineral dissolution and/or precipitation processes.

CONCLUSIONS

Our laboratory study shows that CO_2 acts on the conductivity of a porous medium in several ways: By changing water saturation, by chemical interaction with the fluid phase and by mineral dissolution/precipitation processes. The chemical interaction with the pore water phase appears in different manifestations depending on salinity of the solution. We present a semi-analytical formulation to explain and predict these effects.

The transition salinity between the regimes of conductivity increase and conductivity decrease is in the range of shallow clean aquifer salinities. Therefore, the observed effect is very important for leakage detection methods. Migrating CO_2 might cause complex electrical anomalies with conductive and resistive areas. These effects have to be kept in mind when interpreting the flow experiments.

The spectral complex conductivity maps both changes in saturation and chemical interaction. When the CO_2-effects are taken into account a robust quantification of saturation and mineral dissolution and precipitation processes is possible.

ACKNOWLEDGMENTS

REFERENCES

Archie, G. E., 1942. The electrical resistivity log as an aid in determining some reservoir characteristics. *Transactions of the American Institute of Mining, Metallurgical and Petroleum Engineers, 146*, 54 – 62.

Börner, F. D., Schopper, J. R. & Weller, A., 1996. Evaluation of transport and storage properties in the soil and groundwater zone from induced polarization measurements. *Geophysical Prospecting, 44*, 583-601.

Börner, J. H., Herdegen, V., Repke, J.-U. and Spitzer, K., 2013. The impact of CO_2 on the electrical properties of water bearing porous media - laboratory experiments with respect to carbon capture and storage. *Geophysical Prospecting, 61*, 446 – 460.

Börner, J.H., Herdegen, V., Repke, J.-U. und Spitzer, K., 2015. The electrical conductivity of CO₂-bearing pore waters at elevated pressure and temperature: A laboratory study and its implications in CO_2 storage monitoring and leakage detection. Geophysical Journal International: 203: 1072-1084.

Duan, Z., Sun, R., Zhu, C. and Chou, I., 2006. An improved model for the calculation of CO_2 solubility in aqueous solutions containing Na^+, K^+, Ca^{2+}, Mg^{2+}, Cl^- and SO_4^{2-}. *Marine Chemistry, 98*, 131-139.

Revil, A. and Skold, M., 2011. Salinity dependence of spectral induced polarization in sands and sandstones. *Geophysical Journal International, 187*, 813-824.

Skold, M., Revil, A. and Vaudelet, P., 2011. The pH dependence of spectral induced polarization of silica sands: Experiment and modeling. *Geophysical Research Letters, 38*, L12304.

Vinegar, H. J. and Waxman, M. H., 1984. Induced polarization of shaly sands. *Geophysics, 49*, 1267-1287.

Weller, A. and Slater, L., 2012. Salinity dependence of complex conductivity of unconsolidated and consolidated materials: Comparisons with electrical double layer models. *Geophysics, 77*, D185-D198.

Weller, A., Slater, L., Nordsiek, S. and Ntarlagiannis, D., 2010. On the estimation of specific surface per unit pore volume from induced polarization: A robust empirical relation fits multiple data sets. *Geophysics, 75*, WA105-WA112.
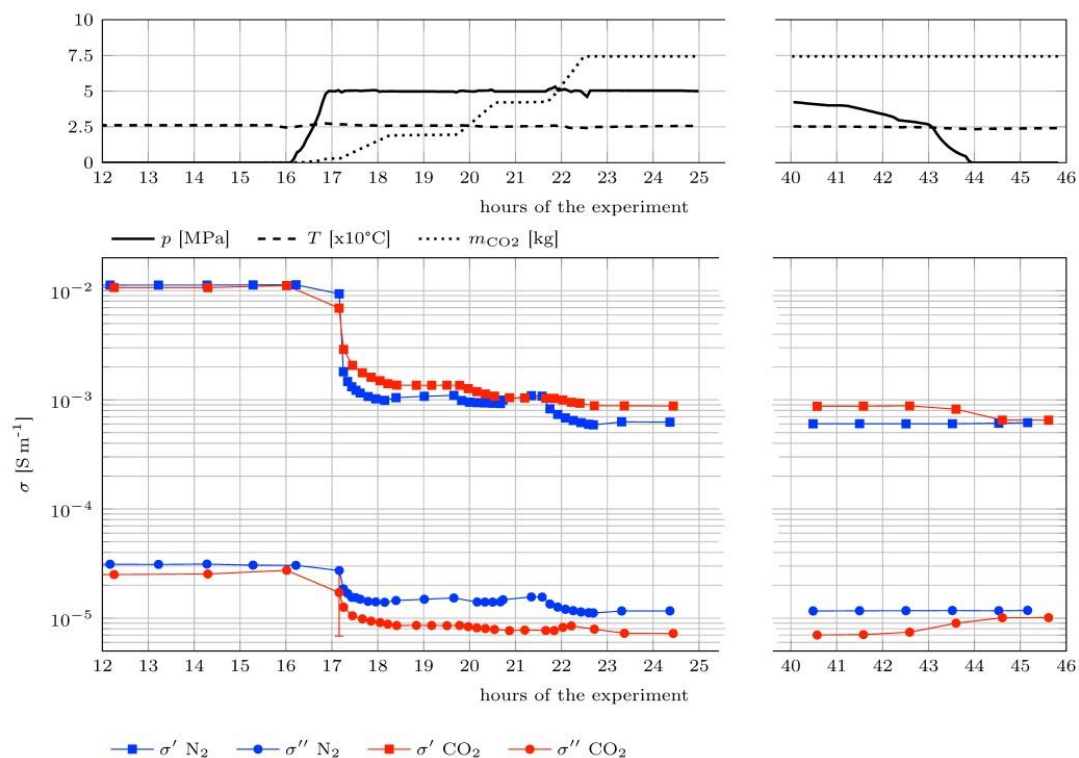

Figure 3. Top: pressure, temperature and cumulative CO₂ mass. Bottom: Real and imaginary part of conductivity at 11.7 Hz vs. time at 50 bar and 25°C with CO₂ (reactive, red symbols) and N₂ (non-reactive, blue symbols), respectively. The time period from 25 to 40 hours is skipped since no changes of the shown quantities occurred in this period.

Predictive relationships for the permeability of unconsolidated sands based on SIP and pore surface fractal dimensions

Malcolm Ingham
Victoria University of Wellington
PO Box 600
Wellington
New Zealand
malcolm.ingham @vuw.ac.nz

Sheen Joseph
Victoria University of Wellington
PO Box 600
Wellington
New Zealand
sheen.josephm @gmail.com

SUMMARY

We present calculations of specific internal surface (S_{por}) and pore surface fractal dimension (D) based on measurements on unconsolidated sand samples. It is found that for these samples, for which the effective hydraulic radius is greater than 10 μm, $D \approx 2$ and the generalized PaRiS model of Weller et al. (2015) gives a good prediction of permeability both for the unconsolidated samples and for the sandstone samples reported by Zhang and Weller (2014). We use fitted relationships to S_{por} for both the SIP time constant (τ) and the measured imaginary part of the conductivity at a frequency of 1 Hz (σ'') to deduce predictive relationships for permeability based on τ and σ'', on the assumption that $D = 2$. These relationships both overestimate permeability but improved predictions are obtained by using a slightly lower value of D commensurate with the average of the calculated values.

Key words: SIP, fractal dimension, specific internal surface, permeability.

INTRODUCTION

Assuming equivalence of electrical and hydraulic tortuosity, the Kozeny-Carman equation can be expressed in a form that relates the permeability (k) of a natural porous medium to the electrical formation factor (F) and the specific internal surface (S_{por})

$$k = \frac{1}{2 F S_{por}^{2}} \qquad (1)$$

The proportionality of S_{por} to both the surface conductivity (σ_{surf}) and the imaginary part of the bulk conductivity (σ'') as measured by spectral induced polarization (Weller et al, 2015) has led to predictive relations for permeability based on these parameters. For sandstone samples Zhang and Weller (2014) have also demonstrated a relationship between S_{por} and the fractal dimension (D) of the pore surface and incorporated D into a more general form of the PaRiS model

$$k = \frac{1}{8F} (\lambda_{N_2})^{\frac{2D-4}{D-3}} \left(\frac{S_{por}}{2} \right)^{\frac{2}{D-3}} \qquad (2)$$

originally proposed by Pape et al. (1987). In (2) λ_{N_2} represents the minimal length scale over which self-similarity occurs and

is generally taken as the diameter of a nitrogen molecule (0.4 nm).

In this paper we present measurements made on unconsolidated sand samples and calculate values of both S_{por} and D and compare the relationships between these and permeability with those found by Zhang and Weller (2014).

We find that for our unconsolidated samples, as long as the effective hydraulic radius (r_{eff}) is greater than 10 μm, the fractal dimension is very close to 2. In contrast, as observed by Zhang and Weller (2014), if r_{eff} is smaller than this there is a linear relationship between D and S_{por}. Using $D = 2$ for unconsolidated samples generalized forms of the PaRiS model (equation (2)) using σ'' or the SIP time constant (τ) slightly overestimate the permeability.

METHOD

SIP and permeability measurements have been made on sand samples which have been sieved into different size fractions in the range $\varphi = 0.00$ and $\varphi = 3.00$ on the Krumbein scale. The method for SIP and permeability measurements has been described previously by Joseph et al. (2015). Measurements have been made on both individual size fractions and on samples consisting of mixtures of different size fractions.

The specific internal surface has not been measured directly but, on the assumption of spherical grains, can be calculated using the measured value of the porosity (ϕ) and a knowledge of the total masses and mean diameters of the components of the sample. Thus for a mixture of masses M_1 and M_2 of grains of median diameter D_1 and D_2, S_{por} can be expressed as

$$S_{por} = \frac{6}{\rho \phi V} \left(\frac{M_1}{D_1} + \frac{M_2}{D_2} \right) \qquad (3)$$

where V is the total volume of the sample and ρ is the density of a grain.

From the calculated values of S_{por} estimates of the fractal dimension of the pore surface can be made using the relationship

$$D = 2 + \frac{\log(S_{por}) - \log(2/r_{eff})}{\log(r_{eff}/\lambda_{H_2O})} \qquad (4)$$

which is based on that given by Zhang and Weller (2014) but, as the measurement of S_{por} is based on measurement of the sample porosity, the minimal length scale is taken as the effective diameter of a water molecule (0.28 nm). In (4) r_{eff} can

be calculated from the measured permeability and formation factor using $r_{eff} = \sqrt{8kF}$.

RESULTS

The measured values of k and F, and the calculated values of r_{eff}, S_{por} and D for each of the sand samples are listed in Table 1. Uncertainties in the calculated values of D are slightly less than 0.1, meaning that the fractal dimension is almost indistinguishable from 2 – the normal dimension for surface area.

Sieved samples					
φ	k (m^2)	F	r_{eff}(μm)	S_{por}(m^{-1})	D
0.00	1.78E-10	4.22	77.5	9366	1.915
0.50	1.56E-10	4.48	74.8	14199	1.948
1.00	1.02E-10	3.47	53.2	17950	1.953
1.50	4.47E-11	3.58	35.8	22853	1.937
2.00	3.15E-11	3.80	30.9	32347	1.950
2.50	1.94E-11	3.86	24.5	47278	1.956
3.00	8.11E-12	3.83	15.8	66973	1.946
Mixtures of $\varphi = 0.25$ and $\varphi = 2.50$					
Prop	k (m^2)	F	r_{eff}(μm)	S_{por}(m^{-1})	D
100-0	1.39E-10	3.83	65.3	11094	1.918
90-10	5.83E-11	4.38	45.2	16958	1.920
80-20	5.70E-11	4.74	46.5	22355	1.946
60-40	2.82E-11	4.81	32.9	35874	1.955
20-80	9.80E-12	4.66	19.1	54820	1.942
0-100	1.19E-11	4.23	20.1	55550	1.948
Mixtures of $\varphi = 0.25, 0.50, 0.75$ and $\varphi = 2.50$					
Prop	k (m^2)	F	r_{eff}(μm)	S_{por}(m^{-1})	D
33-33-33-0	5.74E-11	4.25	44.2	13053	1.896
27-27-27-20	2.90E-11	6.09	37.6	30489	1.953
20-20-20-40	9.05E-12	5.84	20.6	41020	1.923
13-13-13-60	7.11E-12	5.28	17.3	46526	1.918
6.7-6.7-6.7-80	6.63E-12	4.84	16.0	56770	1.928

Table 1. Measurements of k, F, r_{eff}, S_{por} and D for sand samples.
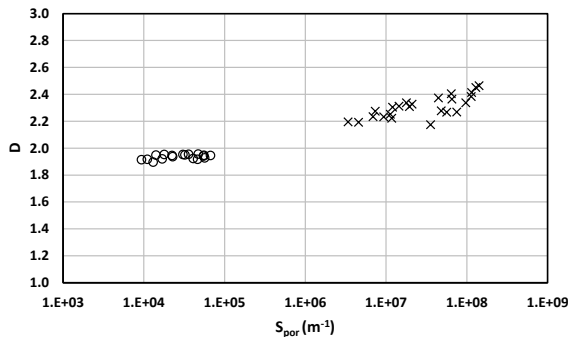

Figure 1. Pore surface fractal dimension plotted against specific internal surface. Circles – sand samples, crosses – sandstone data from Zhang and Weller (2014).

Shown in Figure 1 is a plot of fractal dimension against specific internal surface both for the sand samples listed in

Table 1 and for the sandstone samples discussed by Zhang and Weller (2014). Whereas equation (4) suggests a linear relationship between D and log (S_{por}), as indicated by Zhang and Weller, this appears only to hold for values of the effective hydraulic radius less than about 10 μm. For larger values of r_{eff}, such as for the unconsolidated samples in this study, the fractal dimension is very close to 2. This is illustrated in Figure 2 which shows D plotted against r_{eff}.
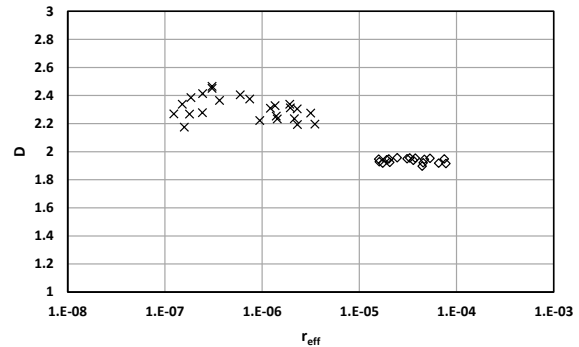

Figure 2. Pore surface fractal dimension plotted against effective hydraulic radius. Circles – sand samples, crosses – sandstone data from Zhang and Weller (2014).

Zhang and Weller (2014) presented equation (2) as a generalized form of the PaRiS model allowing for a variation in fractal dimension. The comparison of permeability predicted by (2) with the measured values is shown in Figure 3(a) in which k_{pred} has been calculated using the values of D calculated for each individual sample.
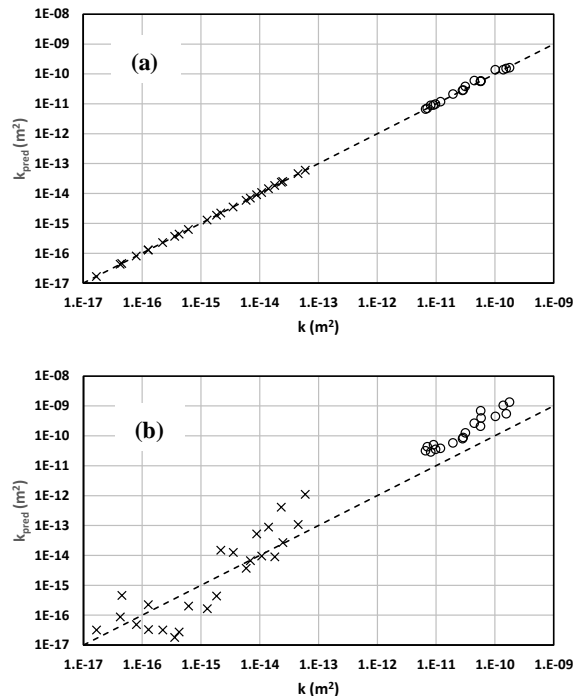

Figure 3. Permeability predicted by equation (2) plotted against measured permeability. (a) Using measured/calculated values of D. (b) Assuming that $D = 2$ for sand samples and $D = 2.307$ for sandstone samples. Circles – sand samples, crosses – sandstone data from Zhang and Weller (2014).

However, given that the fractal dimension is generally unknown, Zhang and Weller tested the predictive power of equation (2) by assuming their average value of D of 2.307. The predicted permeability given by (2) under this assumption for the sandstone samples and assuming a value of $D = 2$ for the unconsolidated samples in this study, is shown in Figure 3(b). Note that the assumption of $D = 2$ for the sand samples means that the term in the minimal scale length reduces to unity.

Although the generalized form of the PaRiS model incorporating variable values of D gives highly accurate values of permeability across at least 7 orders of magnitude, the use of constant values of D for different kinds of samples, while not as accurate, still yields usable predictions of permeability. Nevertheless, use of (2) requires a knowledge of S_{por} which, for field measurements, is not readily available. Thus it is pertinent to seek parameters that can be measured in the field which may have a direct relationship with S_{por} In this regard parameters measurable through the technique of spectral induced polarization (SIP) are the most promising. Weller et al. (2015) have discussed the proportionality of the imaginary part of the conductivity (σ'') measured at 1 Hz frequency with S_{por}. For the unconsolidated samples in this study if σ'' at 1 Hz is treated as a function of S_{por} the best fitting relationship is

$$\sigma'' = 9.84 \ x \ 10^{-7} S_{por}^{0.422}$$

with a coefficient of determination (R^2) of 0.38. Assuming $D = 2$ this leads to the predictive relationship for permeability of

$$k = \frac{1.357 \ x \ 10^{-28}}{8F} \sigma''^{-4.739} \quad (5)$$

in which σ'' is in S/m. The permeability predicted by this equation for the sand samples (shown in Figure 4).
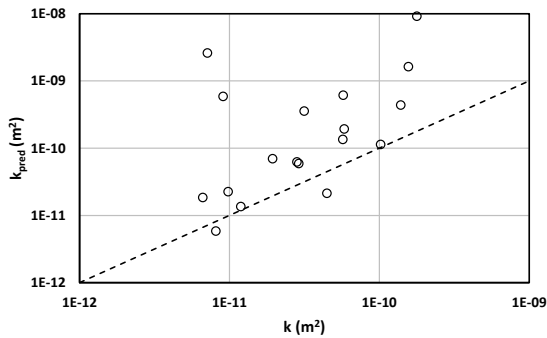

Figure 4. Permeability of sand samples predicted by equation (5) plotted against measured permeability.

The other frequently used parameter derived from SIP data is the time constant (τ) of the low frequency relaxation. For the sand samples listed in Table 1, as shown in Figure 5, there is a strong correlation between τ, determined by fitting a Cole-Cole model to the measured complex conductivity spectrum, and S_{por}. This relationship can be represented by the expression

$$\tau = 7.57 \ x \ 10^8 S_{por}^{-1.797}$$

which, again assuming $D = 2$, leads to the predictive equation for permeability

$$k = \frac{5.247 \ x \ 10^{-10}}{8F} \tau^{1.113} \quad (6)$$

The comparison between measured values of permeability and those predicted by equation (6) is shown in Figure 6.

As can be seen from Figures 4 and 6, both equations (5) and (6) overestimate the permeability. Additionally the permeability values predicted by equation (5) are very scattered reflecting the relatively low value of R^2. The permeability values predicted on the basis of τ, however, give a much better estimate of the measured values and are much less scattered. The overestimation of permeability by about half an order of magnitude comes partly from the use of $D = 2$ in deriving equation (6). The effect of this in increasing the estimate of k can be seen by comparing Figures 3(a) and 3(b). In the cases of predictions based on both σ'' and τ, taking an average value of D from Table 1 and using 2.78 x 10^{-10} m for the minimal scale length produces a much closer fit between the predicted and measured permeability. This is shown for predictions based on τ by the filled data points in Figure 6.
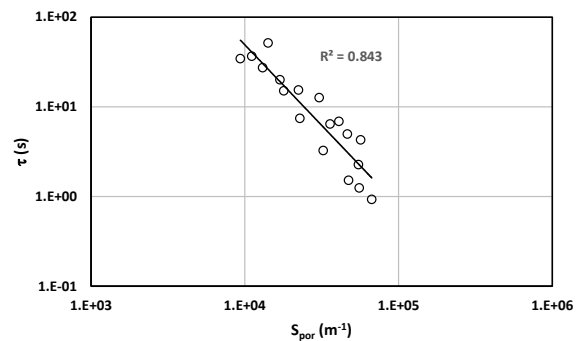

Figure 5. SIP time constant for sand samples plotted as a function of specific internal surface.
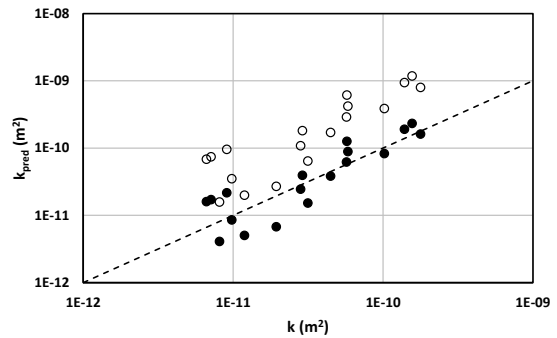

Figure 6. Open circles - permeability of sand samples predicted by equation (6), filled circles - predicted permeability derived from equation (2) using a value of $D = 1.936$.

CONCLUSIONS

Measurements on unconsolidated sand samples, when compared to previous measurements on sandstones, demonstrate the following results.

- For samples for which the effective hydraulic radius is greater than 10 µm the calculated pore surface fractal dimension is close to, but just less than, 2.
- Using the recovered values of D in the generalized PaRiS model presented by Zhang and Weller (2014) gives

excellent predictions of permeability. Using the constant value of 2 leads to a slight overestimation of permeability.

- Power law relationships between both σ'' and τ and S_{por} allow predictive relationships for permeability based on these parameters to be developed.

- Assumption of $D = 2$ for the unconsolidated samples in these relationships leads to an overestimation of k. However, use of an average value of D, slightly lower than 2, gives improved predictions using both σ'' and τ.

It can be concluded that for unconsolidated samples such as those in this study, a pore surface fractal dimension of approximately 2 in the generalized PaRiS model of Weller et al. (2015) can be used to develop predictive equations for permeability.

REFERENCES

Joseph, S., Ingham, M. and Gouws, G., 2015, Spectral induced polarization measurements on New Zealand sands –

dependence on fluid conductivity: Near Surface Geophysics, 13, 169-177

Pape, H., Riepe, L. and Schopper, J.R., 1987, Theory of self-similar network structures in sedimentary and igneous rocks and their investigation with microscopical methods: Journal of Microscopy, 148, 121-147.

Weller, A., Slater, L., Binley, A., Nordsiek, S. and Shujie, X., 2015, Permeability prediction based on induced polarization: Insights from measurements on sandstone and unconsolidated samples spanning a wide permeability range: Geophysics, 80, D161-D173.

Zhang, Z. and Weller, A., 2014, Fractal dimension of pore-space geometry of an Eocene sandstone formation: Geophysics, 79, D377-D387.

Induced polarization of seafloor massive sulfides

A. Hördt, K. Bairlein
TU Braunschweig
Mendelssohnstr. 3
38106 Braunschweig
a.hoerdt@tu-bs.de

G.Spagnoli
BAUER Maschinen GmbH
BAUER-Str. 1
86529 Schrobenhausen
Giovanni.Spagnoli@bauer.de

M.Jegen, M.Hannington, S.Petersen, T. Laurila
GEOMAR Helmholtz Centre for Oceas Research
Wischhofstr. 1-3
24148 Kiel
mjegen@geomar.de

SUMMARY

Sefloor massive sulfides (SMS) are believed to constitute an important future mineral resource. Nevertheless, little is known about the electrical properties of SMS, in particular under in-situ conditions. We measured electrical impedance spectra of 40 samples, 30 of which are sulfide-bearing, and 10 are unmineralized host-rock. The samples were saturated with sodium chloride solution with 5 S/m conductivity.

The resistivity magnitude shows a clear difference between mineralized and unmineralized samples, and also a weak grouping between the different types of mineralization. The imaginary conductivity at 1 Hz indicates a more pronounced discrimination between mineralized and unmineralized samples, suggesting that complex measurements might be useful for exploration purposes. We also measured spectra under dry conditions. Surprisingly, the sulfide-bearing samples exhibit significant phase shifts even for dry samples, indicating that the conducting minerals themselves cause a phase shift, and an interaction with an electrolyte might not be necessary.

Key words: ore exploration, seafloor massive sulfidces, mineralization.

INTRODUCTION

The electrical properties of continental ore-bearing rocks have been studied extensively with outcrops, in the laboratory, and with synthetic mixtures (e.g. Pelton et al., 1978; Vanhala and Peltoniemi, 1992, Nelson and van Voorhis 1983; Hupfer et al., 2015). However, except for some local studies (e.g. Iturrino et al., 2000; Bartetzko et al., 2006), little is known about the electrical properties of seafloor deposits. There is an increasing interest, in particular in seafloor massive sulfides (SMS), which are considered a new source of base metals with economic relevance (e.g. Hoagland et al. 2010; Hannington et al., 2011).

Since seafloor rocks are saturated with significantly more conductive electrolyte compared to continental rocks, and have a different chemical history, it is not obvious that results obtained with continental studies can be transferred to seafloor conditions. Therefore, we measure electrical impedance spectra of 30 SMS samples and 10 unmineralized seafloor basalt samples and investigate potential relationships between SIP parameters and mineral content.

METHODS AND RESULTS

The samples consist of a selection from different seafloor locations representing different tectonic settings, and a variety of compositions, ranging from basalt host rock, non-ore mineralization to massive sulfide mineralizations with different dominant base metals. A detailed description can be found in Spagnoli et al. (2016).

The 40 plugs with 25 mm diameter and 50 mm length were measured with the sample holder and impedance analyzer previously used for the investigation of sandstones and described in Hördt and Milde (2012). A highly conductive sodium chloride solution with 5 S/m conductivity was used to saturate the samples to simulate the seafloor conditions. Each samples underwent a well-defined cycle of saturation and drying, described in detail in Spagnoli et al. (2016). In order avoid a current bypass through at the interface between sample and acrylic glass cylinder, the samples were wrapped with teflon tape.

Figure 1 shows the resistivity magnitude and imaginary conductivity at a frequency of 1 Hz, sorted by sample number, that corresponds to a grouping according to the dominant mineralization type. The unmineralized or non-ore mineralized samples, which include the basalt, Ba-rich and Si-rich samples, generally have higher resistivities compared to the sulfide samples. In particular the Fe-rich and Cu-rich samples have very low resistivities below 1Ωm, and some even below the resistivity of the fluid used for saturation (0,2 Ωm).

The low resistivities cannot be explained with purely electrolytic conductivity and are most likely due to the conducting minerals. We conclude that the minerals are connected in these samples. This obervation is important because it means that the electrical spectra cannot be explained based on most of the existing theoretical models, which are exclusively designed for disseminated mineralization (eg. Wong, 1979; Revil et al., 2015).
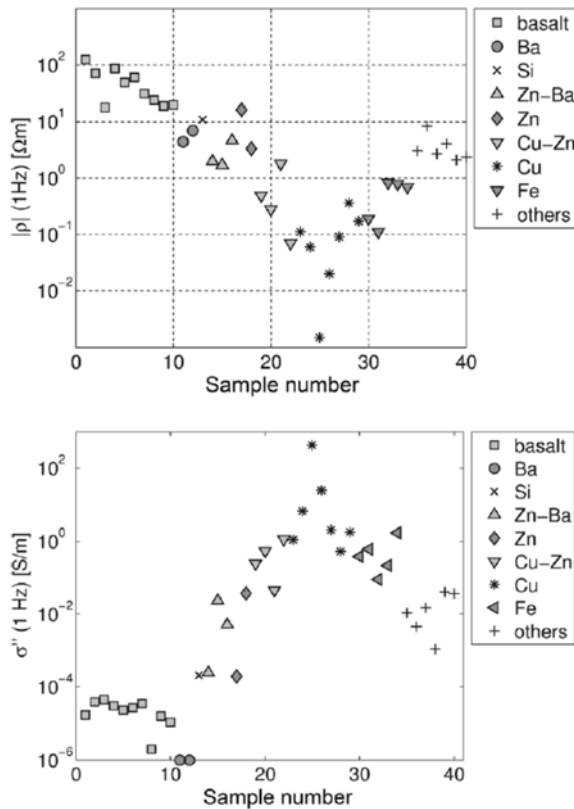
Figure 1. Resistivity magnitude (top panel) and imaginary conductivity (bottom panel) sorted by sample number, indicating the dominating type of mineral content. Figure modified after Spagnoli et al. (2016).

The imaginary conductivity (bottom panel of figure 1) shows a similar behaviour as the resistivity magnitudes: the non-mineralized samples have small imaginary conductivities, the sulfides have much larger values, with maxima for the Fe-rich and Cu-rich samples. However, compared to the resistivity magnitudes, the discrimination is considerably enhanced, the variation is more than 8 orders of magnitude in the imaginary conductivity compared to > 4 orders of magnitude for the resistivities. This is because the phase shifts are large for the mineralized samples and small for the unmineralized samples.

Figure 2 shows 6 selected spectra, 3 of which are for unmineralized, and 3 for mineralized samples. The sulfide bearing samples generally have large phase shifts in the range of several 100 mrad, and low resistivites, whereas sulfide-free samples have small phase shift and high resistivites. This was qualitatively expected and means that the principle idea, using IP to explore for ores, might work also under highly saline conditions met at the seafloor.
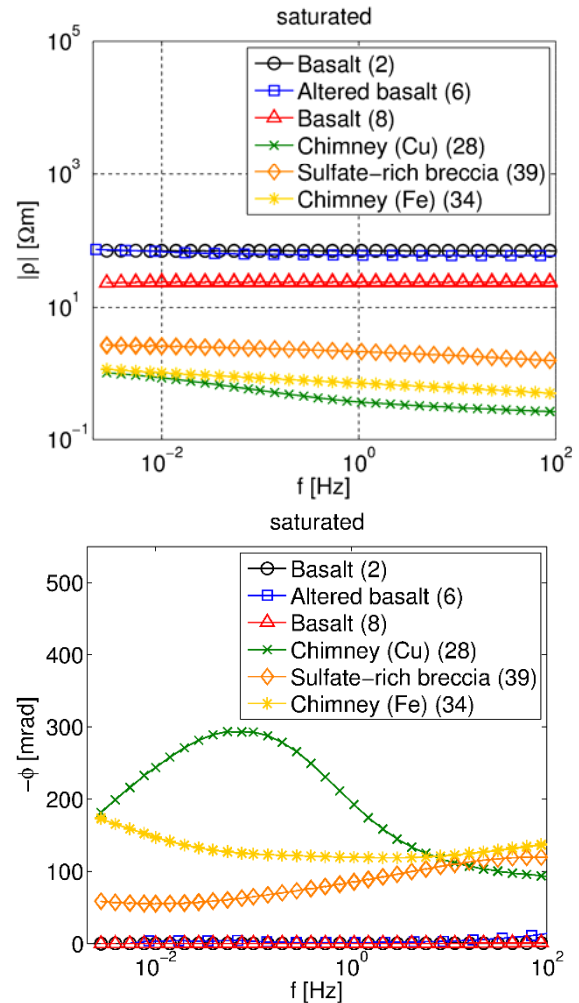

Figure 2. Selected spectra of three samples with no significant sulfide content (basalt samples) and three samples with significant sulfide content, saturated with 5 S/m sodium chlorite solution. Top panel: resistivity magnitudes. Bottom panel: phase shift.

The samples were also measured under dry conditions, after drying in a vacuum chamber at 10 mbar and 40°C for at least 24 hours. As expected, the resistivity magnitudes (figure 3, top panel) have considerably increased compared to the saturated samples. However, the resistivities of two mineralized samples are still small (below 10 Ωm), confirming that the conducting minerals are connected and thus contribute significantly to the bulk conductivity.

The phase shifts of the dry samples (figure 3, bottom panel) are large and reach up to several 100 mrad. This is unexpected, because it is generally assumed that the elctrolyte is essential to generate an IP effect. One hypothesis is that the phase shifts are an artefact caused by EM coupling effects or by the electrode impedance that might be relevant at high impedances. This is particularly apparent for the basalt samples, where the phase shift is large only at high frequencies. However, the mineralized samples do not have a particularly large resistance, and exhibit large phase shifts also at low frequencies. Therefore, an alternative hypothesis might be that the phase shift is caused by the conducting minerals themselves, without an electrolyte.
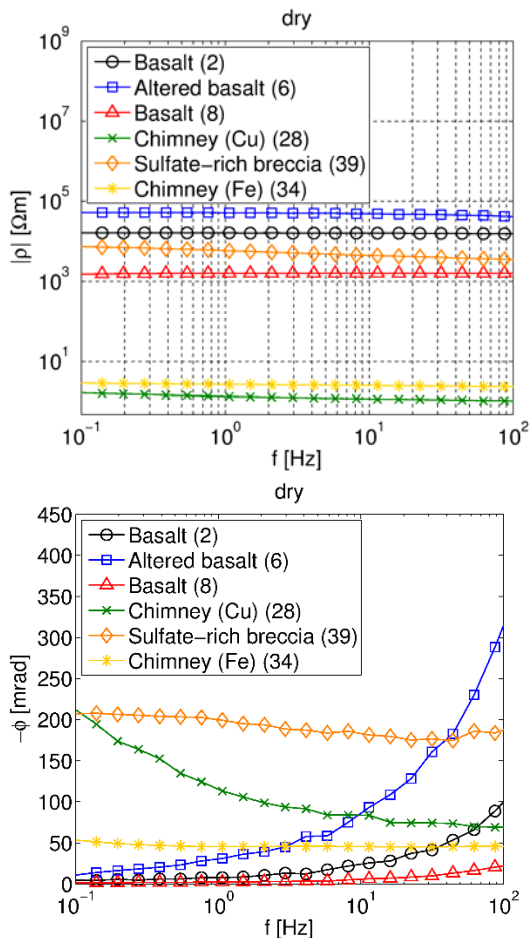
Figure 3. Spectra of the same samples shown in figure 2, after drying under vacuum and 40°C. Top panel: resistivity magnitude vs. frequency. bottom panel: phase shift vs. frequency.

CONCLUSIONS

Seafloor massive sulfides show a strong IP effect, i.e. large imaginary conductivities and phase shifts, even under highly saline conditions. This is not unexpected, considering previous results with continental ores, but is nevertheless considered an important experimental observation.

The results indicate that using the imaginary conductivity, even different types of mineralization (e.g. Cu-rich and Fe-rich) might be discriminated. According to previous studies, this discrimination would be due to texture of the minerals rather than their chemistry (e.g. Pelton et al., 1978). Many of the samples investigated here have resistivities so small that they can not be explained by electrolytic conductivity. This is confirmed by the measurements with dry samples, which also show low resistivites. We conclude that the minerals in those samples must be connected, and thus the spectra cannot be understood with existing theories, which are based on disseminated minerals.

We also observe large phase shifts for the dry samples. These results must be treated with caution, because they might be distorted by electrode effects. However, if confirmed, the consequences could be important because existing theories assume the elctrolyte as essential to explain IP effects.

REFERENCES

Bartetzko A., Klitzsch, N,, Itturino, G., Kaufhold, S., and Arnold, J., 2006, Electrical properties of hydrothermally altered dacite from the PACMANUS hydrothermal field (ODP Leg 193): Journal of Volcanology and Geothermal Research 152, 109-120.

Hannington, M., Jamieson, J., Monecke, T., Petersen S., Beaulieu, S. 2011. The abundance of seafloor massive sulfide deposits: Geology 39. 1155–1158.

Hoagland, P., Beaulieu, S., Tivey, M.A., Eggert, R.G, German, C., Glowka, L., Lin, J., 2009, Deep-sea mining of seafloor massive sulfides: Marine Policy 34: 728–732.

Hördt, A., and Milde, S., 2012, Studies on the origin of induced polarisation with gel-filled sandstone samples: Near-surface Geophysics, 6, 469-478.

Hupfer, S., Martin, T., Weller, A., Günther, T., Kuhn, K., Djotsa Nguimeya Ngninjio, V., Noell, U., 2015, Polarization effects of unconsolidated sulphide-sand-mixtures: Journal of Applied Geophysics, *in press.*

Iturrino, G.J,, Davis, E., Johnson, J., Gröschel-Becker, H. M., Lewis, T.J., Chapman, D., Cermak, V., 2000, Permeability, electrical, and thermal properties of sulfide, sedimentary, and basaltic units from the Bent Hill area of Middle Valley, Juan de Fuca Ridge. In: Zierenberg RA, Fouquet Y, Miller, Normark WR (ed), Proceedings of the Ocean Drilling Program, Scientific Results, 1-42, doi:10.2973/odp.proc.sr.169.115.2000.

Nelson, P.H., Van Voorhis, G.D., 1983, Estimation of sulfide content from induced polarization data: Geophysics, 48 (1), 62-75.

Pelton, W.H., S.H. Ward, G. Hallof, W.R. Sill, and P.H. Nelson, 1978, Mineral discrimination and removal of inductive coupling with multifrequency IP: Geophysics 43, 588-609.

Revil, A., Florsch, N., Mao, D. 2015, Induced polarization response of porous media with metallic particles -Part 1: A theory for disseminated semiconductors: Geophysics, 80 (5), D525-D538.

Spagnoli, G., Hannington, M., Bairlein, K., Hördt, A., Jegen, M., Petersen, S., and Laurila, T., 2016, Electrical properties of seafloor massive sulfides: Geo-marine letters, DOI 10.1007/s00367-016-0439-5.

Vanhala, H., Peltoniemi, M, 1992: Spectral IP studies of Finnish ore prospects: Geophysics, 57 (12), 1545-1555.

Wong, J., 1979, An electrochemical model of the induced polarization phenomenon in disseminated sulfide ores: Geophysics, 44, 1245-1265.

On the α-polarization of bacterial suspensions: SIP measurements on E. coli K12 and Rhodococcus erythropolis T902.1

Tamara PILAWSKI
Applied Geophysics Research Unit
Department ArGEnCo
Faculty of Applied Sciences
University of Liège
Allée de la Découverte 9 (B52)
4000 Liège
Belgium
tamara.pilawski@ulg.ac.be

Wolfgang TAPPE
Institute of Bio- and Geosciences
Agrosphere (IBG-3)
Forschungszentrum Jülich GmbH
52425 Jülich
Germany
w.tappe@fz-juelich.de

Egon ZIMMERMANN
Central Institute for Engineering,
Electronics and Analytics (ZEA-2)
Forschungszentrum Jülich GmbH
52425 Jülich
Germany
e.zimmermann@fz-juelich.de

Johan Alexander HUISMAN
Institute of Bio- and Geosciences
Agrosphere (IBG-3)
Forschungszentrum Jülich GmbH
52425 Jülich
Germany
s.huisman@fz-juelich.de

Frank DELVIGNE
Microbial Processes and Interactions
Gembloux Agro-Bio Tech
University of Liège
Passage des Déportés 2
5030 Gembloux
Belgium
f.delvigne@ulg.ac.be

Frédéric NGUYEN
Applied Geophysics Research Unit
Department ArGEnCo
Faculty of Applied Sciences
University of Liège
Allée de la Découverte 9 (B52)
4000 Liège
Belgium
f.nguyen@ulg.ac.be

SUMMARY

The influence of bacteria on the electrical properties of porous media has been explained by different mechanisms. A few studies have also reported direct bacterial polarization using measurements on bacterial suspensions at frequencies below 10 kHz, so-called α-polarization. These measurements were performed by dielectric spectroscopy techniques relying on two electrodes and models to correct for electrode polarization at low frequencies.

We performed complex conductivity measurements on bacterial suspensions from 0.01 to 45,000 Hz with an impedance spectrometer (phase accuracy better than 0.1 mrad below 1 kHz for a measurement on water) that used four-point measurements and thus does not require large corrections for electrode polarization). Two strains were studied: Escherichia coli (Gram-negative bacterium) and Rhodococcus erythropolis (Gram-positive bacterium). The imaginary parts of the complex conductivity of suspensions of both strains were very similar to the one of water. These preliminary results suggest that microbial alterations of the complex electrical conductivity measurements of porous media observed in previous studies are more likely related to other mechanisms than α-polarization of the bacteria, such as bioclogging, biomineralization, and growth and attachment of microbial cells to the sediment grains. We are planning to test additional strains to verify these results.

Key words: SIP, biogeophysics, bacteria, α-polarization

INTRODUCTION

For the last decade, numerous studies have shown geophysical changes in geological media affected by bacterial activity (Atekwana and Slater, 2009; Davis *et al.*, 2010; Masy *et al.*, 2016). Among the different geophysical techniques, spectral induced polarization was shown to be particularly sensitive to subsurface bacterial processes and microbially-induced alterations. Different mechanisms were proposed to explain the influence of bacteria on the electrical properties: bioclogging (Ntarlagiannis *et al.*, 2005; Abdel Aal *et al.*, 2010a), biomineralization (Atekwana and Abdel Aal, 2015; Personna *et al.*, 2008; Williams et al., 2005), growth and attachment of microbial cells to the sediment grains (Abdel Aal et *al.*, 2004, 2009 and 2010b; Davis et *al.,* 2006), and mineral weathering (Atekwana *et al.*, 2004). A few studies have also reported bacterial polarization at frequencies below 10 kHz, often referred to as α-polarization (Prodan *et al.*, 2008; Bot and Prodan, 2009; Zhang *et al.*, 2013). α-polarization has been mainly explained by a reversible storage of electrical charges moving under the influence of the external electrical field and being stored at some polarization length scales (Revil *et al.*, 2012). To our knowledge, all published measurements on bacterial suspensions have been measured using two-electrode setups that require correction for electrode polarizations in the kHz frequency range and below. To date, α-polarization measurements on bacteria remain difficult because of the considerable uncertainty in the correction of the large electrode polarization that occurs in the same frequency range as α-polarization (Asami, 2014).

The main purpose of this study was to measure the complex conductivity of bacterial suspensions at frequencies from 0.01 to 45,000 Hz with a high-accuracy impedance spectrometer (phase accuracy better than 0.1 mrad below 1 kHz for a measurement on water) and to determine the polarization associated with bacterial cells at this frequency range. Two strains were studied: Escherichia coli K12 and Rhodococcus erythropolis T902.1. E. coli is a rod-shaped Gram-negative bacterium found in the lower intestine of warm-blooded

organisms. R. erythropolis is a Gram-positive microorganism known to degrade hydrocarbons and has therefore been used in bioremediation.

MATERIALS AND METHODS

Bacteria cultivation and preparation

E. coli K12 wild type and R. erythropolis T902.1 were obtained from the Bio-Industries Research Unit of Gembloux Agro-Bio Tech and the Walloon Center of Industrial Biology of the University of Liège, respectively. Cultures were prepared in duplicate in 1 L flasks containing 500 ml of 8 g/l nutrient broth (Merck, 5443) consisting of 5 g/l of peptone and 3 g/l of meat extract. Bacteria were incubated at lab temperature (20°C) and 100 rpm orbital agitation until they reached the early stationary phase. Growth was monitored by optical density (OD) measurements at 570 nm. The cells were pelleted at 3345 x g for 30 minutes, and washed twice in M284 minimal medium (0.0275 mol/l KH_2PO_4, 0.0391 mol/l $Na_2HPO_4.12H_2O$, 0.02 mol/l NH_4Cl, 0.003 mol/l N_2SO_4, 0.00098 mol/l $MgCl_2.6H_2O$, 0.0002 mol/l $CaCl_2.2H_2O$, 0.000011 mol/l $C_6H_5FeO_7.H_2O$ and trace elements) diluted 20 times with milli-Q water (electrical conductivity of 612 µS/cm at 20°C). They were then resuspended in M284 minimal medium diluted 20 times so that the final OD at 570 nm was 0.40. Petri plates were prepared to count the colony-forming units (CFU) in order to estimate the number of viable cells of the samples.

Experimental setup

Low frequency electrical measurements (0.01 – 45,000 Hz) were performed in a 40 cm long polycarbonate column with an inner diameter of 3.4 cm. The measurement system developed in the Forschungszentrum Jülich is based on a four point measurement method as described in Zimmermann *et al.* (2008). It can measure the spectral induced polarization response of the bacteria suspensions with a phase accuracy better than 0.1 mrad up to 1000 Hz. Two brass electrodes were used as current electrodes and were fully inserted into the sample holder (perpendicular to the main axis of the column). Two brass potential electrodes were installed between the current electrodes. They were placed outside the sample to minimize electrode polarization at the surface of the electrodes. The spacing between the different electrodes was 12 cm.

RESULTS

Figure 1 shows the imaginary parts of the complex electrical conductivity (σ'') of E. coli and R. erythropolis. They were obtained by averaging two independent measurements. For comparison, σ'' of the water used to resuspend the bacteria is also plotted on the graph. No significant difference is observed between the two strains and the water, which strongly suggests that no α-polarization is observed for the two bacterial strains.

The viability of the cells was assessed by CFU counting on Petri plates. The CFU of E. coli and R. erythropolis were $(6.2\pm4.3)*10^8$ and $(9.2\pm0.4)*10^7$ CFU/ml, respectively.

CONCLUSIONS

α-polarization has been postulated to explain changes in the complex electrical conductivity below 10 kHz observed in geological media affected by bacterial activity. This polarization was measured in a few dielectric spectroscopy studies where strong electrode polarization required large corrections (Bot and Prodan, 2009; Zhang *et al.*, 2013). We performed complex electrical conductivity measurements on two bacterial suspensions using an impedance spectrometer at frequencies from 0.01 to 45,000 Hz and we did not observe any polarization. Therefore, we conclude that at lower frequencies other mechanisms are more likely to explain the influence of bacteria on the electrical properties of porous media: bioclogging, biomineralization, growth and attachment of microbial cells on the sediment grains.

We are planning to confirm these results by repeating these measurements (to get triplicates) and to test two other strains: Pseudomonas putida (Gram-negative bacterium) and Bacillus subtilis (Gram-positive bacterium).

REFERENCES

Abdel Aal, G., Atekwana, E., Slater, L., and Atekwana, E., Effects of microbial processes on electrolytic and interfacial electrical properties of unconsolidated sediments: Geophysical Research Letters, 31 (12), L12505.

Abdel Aal, G., Atekwana, E., Radzikowski, S., and Rossbach, S., 2009, Effect of bacterial adsorption on low frequency electrical properties of clean quartz sands and iron-oxide coated sands: Geophysical Research Letters, 36 (4), L04403.

Abdel Aal, G., Atekwana, E., and Atekwana, E., 2010a, Effect of bioclogging in porous media on complex conductivity signatures: Journal of Geophysical Research, 115, G00G07.

Abdel Aal, G., Atekwana, E., Rossbach, S., and Werkema, D., 2010b, Sensitivity of geoelectrical measurements to the presence of bacteria in porous media: Journal of Geophysical Research, 115, G03G017.

Asami, K., 2014, Low-frequency dielectric dispersion of bacterial cell suspensions: Colloids and Surfaces B: Biointerfaces, 119.

Atekwana, E., and Abdel Aal, G., 2015, Iron biomineralization controls on geophysical signatures of hydrocarbon contaminated sediments: Journal of Earth Science, 26 (6), 835-843.

Atekwana, E., and Slater, L., 2009, Biogeophysics: A new frontier in Earth science research: Reviews of Geophysics, 47 (4), RG4004.

Atekwana, E., Atekwana, E., Werkema, D., Allen, J., Smart, L., Duris, J., Cassidy, D., Sauck, W.,and Rossbach, S., 2004, Evidence for microbial enhanced electrical conductivity in

hydrocarbon-contaminated sediments: Geophysical Research Letters, 31, L23501

Bot and Prodan, 2009, Probing the membrane potential of living cells by dielectric spectroscopy: European Biophysics Journal, 38 (8), 1049-1059.

Davis, C., Atekwana, E., Atekwana, E., Slater, L., Rossbach, S., and Mormile, M., 2006, Microbial growth and biofilm formation in geologic media is detected with complex conductivity measurements: Geophysical Research Letters, 33, L18403.

Davis, C., Pyrak-Nolte, L., Atekwana, E., Werkema, D., and Haugen., M., 2010, Acoustic and electrical property changes due to microbial growth and biofilm formation in porous media: Journal of Geophysical Research, 115, G00G06.

Masy, T., Caterina, D., Tromme, O., Lavigne, B., Thonart, P., Hiligsmann, S., and Nguyen, F., 2016, Electrical resistivity tomography to monitor enhanced biodegradation of hydrocarbons with Rhodococcus erythropolis T902.1 at a pilot scale: Journal of Contaminant Hydrology, 184.

Naudet, V., and Revil, A., 2005, A sandbox experiment to investigate bacteria-mediated redox processes on self-potential signals: Geophysical Research Letters, 32, L11405.

Ntarlagiannis, D., Yee, N., Slater, L., 2005, On the low-frequency electrical polarization of bacterial cells in sands: Geophysical Research Letters, 32, L24402.

Personna, Y., Ntarlagiannis, D., Slater, L., Yee, N., O'Brien M., and Hubbard, S., 2008, Spectral induced polarization and electrodic potential monitoring of microbially mediated iron sulfide transformations: Journal of Geophysical Research, 113, G02020.

Prodan, E., Prodan, C., and Miller, J.H., 2008, The Dielectric Response of Spherical Live Cells in Suspension: An Analytic Solution: Biophysical Journal, 95 (9), 4174-4182.

Revil, A., Atekwana, E., Zhang, C., Jardani, A., and Smith S., 2012, A new model for the spectral induced polarization signature of bacterial growth in porous media: Water Resources Research, 48, W09545.

Williams, K., Ntarlagiannis, D., Slater, L., Dohnalkova, A., Hubbard, S., and Banfield, J., Geophysical Imaging of Stimulated Microbial Biomineralization: Environmental Science & Technology, 39 (19), 7592-7600.

Zhang, C., Salter, L. and Prodan, C., 2013, Complex Dielectric Properties of Sulfate-Reducing Bacteria Suspensions: Geomicrobiology Journal, 30 (6), 490-496.

Zimmermann, E., Kemna, A., Berwix, J., Glaas, W., Münch, H.M., and Huisman, J.A., 2008, A high-accuracy impedance spectrometer for measuring sediments with low polarizability: Measurement Science and Technology, 18, 105603.
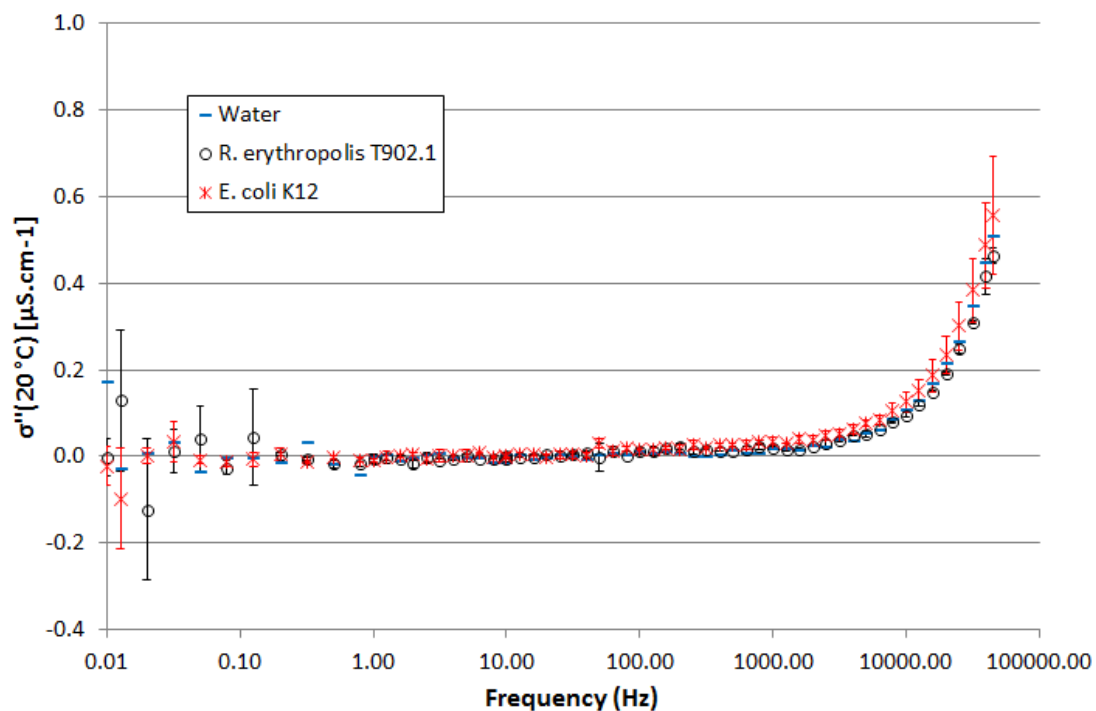
Figure 1. Imaginary parts of the complex electrical conductivity (σ'') measured on suspensions of E. coli and R. erythropolis between 0.1 and 45,000 Hz. They were obtained by averaging two independent measurements. The

vertical error bars represent the standard deviation of the data. For comparison, σ'' of the water used to resuspend the bacteria is also shown on the graph.

IP2016/4th International Workshop on Induced Polarization

www.sip-archiv.de – an internet based, interactive archive and database for SIP data

Matthias Halisch, Jens Gramenz, Lothar Gorling, Klaus Krause, Iakov Bolotovski
Leibniz Institute for Applied Geophysics (LIAG)
Stilleweg 2, D-30655 Hannover, Germany
matthias.halisch@liag-hannover.de

SUMMARY

Long-term storage of scientific data has become a topic of utmost importance for the scientific community. Due to European and national (here: German) initiatives, new guidelines and laws have been validated to ensure a reliable storage and documentation of scientific primary data.

As a result of a workshop and discussion round of the working committee induced polarization (AK-IP) of the German Geophysical Society (DGG), the Leibniz Institute for Applied Geophysics (LIAG) accepted the challenge to develop and create a safe, free and easy to use, internet based database and archive for SIP measurements.

Key words: archive, database, data storage, internet, SIP, SQL

INTRODUCTION

Long-term storage of scientific data has become a topic of utmost importance for the scientific community. Due to European and national initiatives, new guidelines and laws have been validated to ensure a reliable storage and documentation of scientific primary data (e.g.: Kuder and Kühne, 2006; EU, 2007; DFG, 2009; Ludwig & Enke, 2013). Due to more than ten years of experience with the development of scientific database structures (Kühne, 2006), the LIAG decided to create a new database system for a reliable and safe storage of data from SIP measurements. In the following, the authors would like to briefly introduce the main concept of the new database www.sip-archiv.de, to give a short technical report as well as to provide an outlook about the ongoing development.

CONCEPT & TECHNIQUE

The SIP database has been planned with respect to the needs and wishes of the German IP community that have been evaluated between October 2014 and March 2015. Accordingly, the following requirements form the main concept of this database: to provide a safe, long term archive and database structure for SIP data, web based, easy and free to use and self administrated, in order to ensure maximum control over individual and institutional data sets. In addition, this data base provides functionalities to exchange and provide data and metadata with respect to the guidelines of good scientific practice (DFG, 2013).

The backend of the application is developed in PHP (**P**HP: **H**ypertext **P**reprocessor), using a model-view-controller (MVC; Krasner and Pope, 1988) related approach that is based on the framework "CodeIgniter" (https://codeigniter.com). This tool has been chosen to reduce developing time by making use of some handy features like form validation or predefined internationalization routines. Additionally, the built-in abstraction layers make the application more portable, in case of server-side software, i.e. operating system or database engine change. The web frontend uses "Bootstrap" (www.getbootstrap.com) to obtain a responsive layout and enhanced cross browser compatibility. The web pages are served by Microsoft's Internet Information Services (IIS) running on Windows Server. The data is stored in a Structured Query Language (SQL) server database, which is the default relational database management system (RDBMS; Date and Darwen, 1997) in the local data centre. Figure 1 shows a generalized entity-relationship-model of the database. Figure 2 highlights the general architecture and infrastructure.
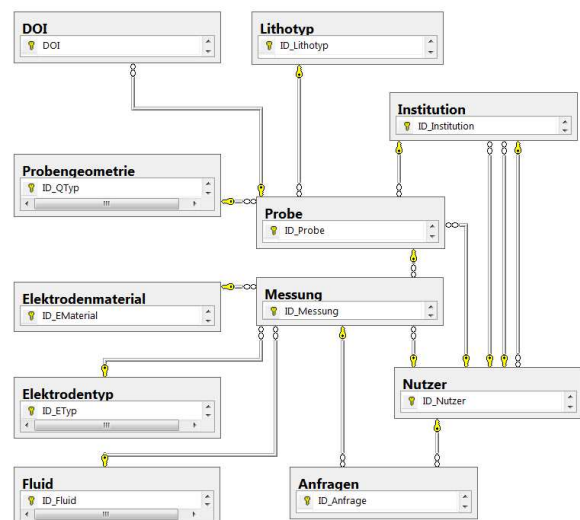

Figure 1. A generalized entity-relationship-model of the database. At the current stage of the development, only data of SIP measurements on hardrock samples are supported. This model will be extended in the near future, to provide storage capabilities for unconsolidated sample and field scale data.

CONCLUSIONS & OUTLOOK

With this archive and database structure, the national and international SIP community gets a powerful tool to store and manage their data from SIP measurements on a long time scale. Additionally, this archive is specifically designed to enhance national and international research collaborations, to initiate systematic round robin tests and / or projects, and to exchange data safely and self-controlled.

As an ongoing development, existing functionalities are permanently evaluated and adopted. New functionalities and storage capacities are planned, e.g. the implementation of laboratory SIP measurements on soil and other unconsolidated sample materials, as well as implementing upload and storage capabilities for field and large scale measurements (SIP profiles, 2D pseudo-sections, SIP soundings, etc.).

ACKNOWLEDGMENTS

REFERENCES

Date, C.J., and Darwen, H., 1997, A guide to the SQL standard: a users guide to the standard database language SQL, 4th edition, Addison Welsey Publishing, USA, 1997.

Deutsche Forschungsgemeinschaft (DFG), Ausschuss für Wissenschaftliche Bibliotheken und Informationssysteme, Unterausschuss für Informationsmanagement, 2009, Empfehlungen zur gesicherten Aufbewahrung und Bereitstellung digitaler Forschungsprimärdaten: www.dfg.de/download/pdf/foerderung/programme/lis/ua_inf_empfehlungen_200901.pdf

Deutsche Forschungsgemeinschaft (DFG), 2013, Momorandum on safeguarding good scientific practice: http://www.dfg.de/download/pdf/dfg_im_profil/reden_stellungnahmen/download/empfehlung_wiss_praxis_1310.pdf

EU Guideline 2007/2/EC, 2007, Infrastructure for Spatial Information in the European Community (INSPIRE): EU Guideline 2007/2/EC, Brüssel.

Kuder, J., and Kühne, K., 2007, GeoMind: Ein europäisches Internetportal für geophysikalische Daten: Mitteilungen der Deutschen Geophysikalischen Gesellschaft, Ausgabe 1+2/2007, S. 1-8, ISSN 0934-6554; Hannover.

Kühne, K., 2006, Das Fachinformationssystem Geophysik und seine Nutzung über das Internet: GIS - Geowissenschaftliche Anwendungen und Entwicklungen, 57. Berg- und Hüttenmännischer Tag, Wiss. Mitteilungen des Instituts für Geologie, 31: 227-231; Freiberg.

Krasner, G.E., and Pope, T.A., 1988, A cookbook for using the model-view controller user interface paradigm in smalltalk-80", J. Object Oriented Program., vol. 1, no. 3, pp. 26-49, Aug. 1988.

Ludwig, J., and Enke, H., 2013, Leitfaden zum Forschungsdaten-Management: 122 pp., Verlag Werner Hülsbusch, Glückstadt, 2013.
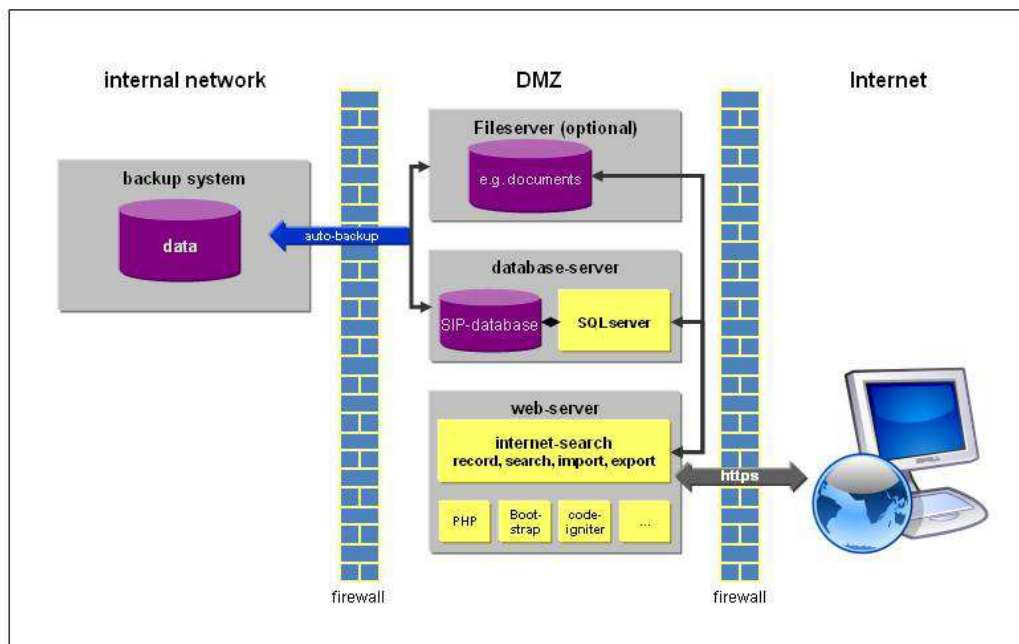
Figure 2. General architecture and infrastructure of www.sip-archiv.de.

SIP investigation at historical mining slag heaps

Tina Martin
Federal Institute for Geosciences and Natural Resources (BGR)
Wilhelmstr. 25-30, D-13593 Berlin/Germany
Tina.Martin@bgr.de

Thomas Günther
Leibniz Institute for Applied Geophysics (LIAG)
Stilleweg 2, D-30655 Hannover/Germany
Thomas.Guenther@liag-hannover.de

SUMMARY

Geophysical investigations at historical slag heaps are increasingly in focus due to economic, environmental or archaeological reasons. We present in this study the investigation of a historical slag heap in the Harz Mountains, Germany, where laboratory and field measurements were conducted.

Previous detailed laboratory measurements of different synthetic mineral-sand mixtures have shown that there is a relationship between chargeability and mineral concentration as well as between relaxation time and mineral grain size. With the development of a new approach for the simultaneous fitting of the whole spectral field data set to different models we are now able to interpret the field measurements further. We started to show that the relationships found in laboratory can be in principle transferred to the field data.

However, in situ samples also show that the SIP response can be very different between samples from the same heap. So a general statement of the mineral content/grain size of a slag heap only from some field profiles is not possible.

With the help of additional mineralogical, chemical and optical methods we try to characterize the different SIP response with the aim of rough classification of slag heap areas.

Key words: slag heap; SIP; field measurements, mineralogical results

INTRODUCTION

For a long time, retrieving residual from historical mining waste dumps was considered economically inefficient. Rising prices and a growing demand have corrected this estimation even for less productive material sources. So in the last few years different own geophysical investigations at abandoned mining heaps were conducted to determine the potential of the raw material. Also for the archaeological application investigation of historical slag heap sites in France were increasingly conducted (Florsch et al., 2011; 2012)

From own laboratory measurements at synthetic mineral-sand mixtures it is known (Hupfer et al., 2015) that concentration and mineral grain size of different minerals can be estimated with the spectral induced polarization (SIP) method by using the Cole-Cole equation (e.g. Cole & Cole, 1941; Pelton et al., 1978). With the newest two dimensional inversion algorithm (Günther & Martin, 2016) the analysis of the field SIP results at mining slag heaps can also improve the interpretation of the residual mineral content so that spatial information about the mineral content of historical heaps seems to be possible.

In this study the results of different profiles at a mining slag heap measured with the SIP technique are shown and compared with the synthetic mineral-sand conclusions. Additionally some (in situ) examples from the heap were investigated in laboratory and show the complexity of a further interpretation.

METHOD AND MATERIAL

A historical slag heap in the south-west part of the Harz mountains/Germany was investigated with several 2D profiles. Starting in the middle ages, copper, lead, silver and zinc ores were mined at different periods before it was abandoned more than 200 years ago. As a result, these dumps exhibit heterogeneous structures, i.e. variations in mineral composition and content, but also dominant grain size are expected. The total extension of the heap is about 600 m x 200 m but it is probably not continuous. The used SIP device was the multi-channel and PC-controlled instrument SIP 256C (Radic, 2004). As configuration we used the dipole-dipole array as it reduces coupling between the current and voltage cable near the electrodes. Although non-polarizable electrodes were recommended to measure small IP effects (e.g. Kemna et al. 2012) we used standard stainless steel electrodes because we expected large polarization effects from the slag. Nevertheless we tried to reduce the electrode influences by using two different electrodes at each measurement point (one for current injection, one for potential measurement). For the profiles we used up to 41 channels with an electrode distance of 1 m. We measured at 14 frequencies between 0.16 and 1000 Hz. A detailed description can be found in Günther & Martin (2016).

The in situ (at the surface) collected slag chunks of two profiles were cut into cylindrical shapes in order to fit into the four-point measuring cell. The samples were fully saturated with tap water ($\sigma = 700$ μS/cm) and measured under controlled laboratory conditions with the instrument SIP-ZEL (Zimmermann et al., 2008). As coupling agent we used an Agar-Agar gel. Parts of the slag chunks were also investigated with the XRF (X-ray fluorescence) spectroscope to analyze the element content. To estimate the porous nature of the slag samples the MIP method (mercury intrusion porosimetry) was applied.

RESULTS

Synthetic mineral-sand-mixtures

Hupfer et al. (2015) showed in their study that there is a strong relationship between the SIP signature and ore concentration, grain radius and pore fluid conductivity. They observed that the polarization increases with increasing ore concentration and with decreasing grain radius. Fitting these data with a Cole-Cole model clear relationships between chargeability and mineral concentration, as well as between relaxation time and grain size, could be found. For different pyrite grain sizes and concentrations the results can be seen in Figure 1.
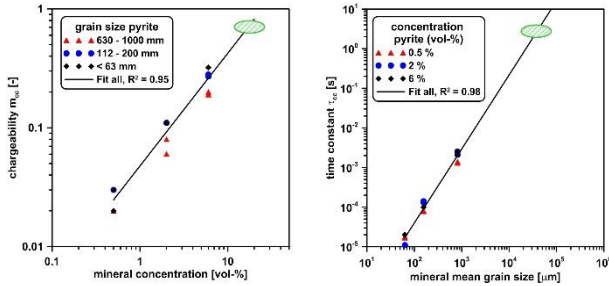
Figure 1: Relationship between chargeability and mineral concentration (left) and time constant and mineral grain size (right) for the synthetic mineral-sand-mixture samples after Hupfer et al. (2015). The green circle shows the expected grain sizes/mineral content from the SIP field measurements.

Field SIP measurements

In this study the results from two field profiles are shown. Profile 3 (Figure 2) was a 32 m long profile with 33 electrodes with an electrode distance of 1 m. The first 7 m of the profile were covered by grass followed by approx. 9 m of slag layer right on top. Further back we found a slag/grass layer sequence. Close to the surface the amplitudes for the frequency of f = 1.25 Hz correlate well with the slag/grass layers (Figure 2, top). So the slag shows typically resistivities above 600 Ωm whereas the soil layer and the surrounding material is defined by smaller resistivities (< 100 Ωm). In phase (Figure 2, bottom) the slag layer correlates with high phase values (> 7°). In contrast, both soil layer and non-slag material shows phase values < 1°.
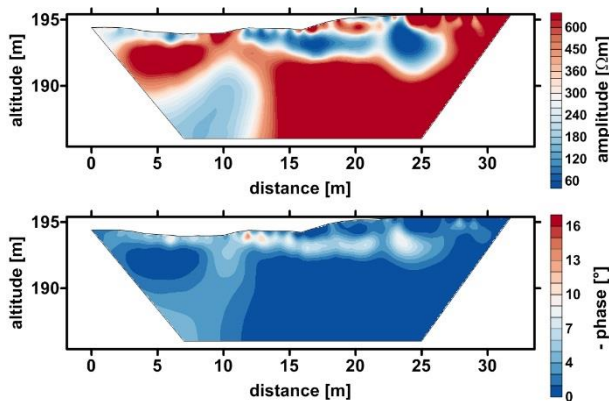

Figure 2: SIP results from profile 3 for 1.25 Hz. Top: amplitude, bottom: phase. The slag material is defined by higher resistivities and high phases.

Profile 5 was conducted approx. 150 m south of profile 3 and directed perpendicular. This profile was 40 m in length with an electrode distance of 1 m. A detailed description of these profiles can be found in Günther & Martin (2016). In the field, this profile was fully covered by grass. Figure 33 shows the results of profile 5 for f = 1.25 Hz. In resistivity (top) a high resistive layer can be found in a depth of approx. 1.5 - 2 m. This layer seems too thin out to the right hand part of the profile. In the phase section (bottom) a zone of high phase (up to 16°) in approx. 3 m depth can be seen through the whole profile. This layer has a phase maximum for the lowest fully observed frequency of 0.16 Hz. To higher frequencies these layer decrease in phase.
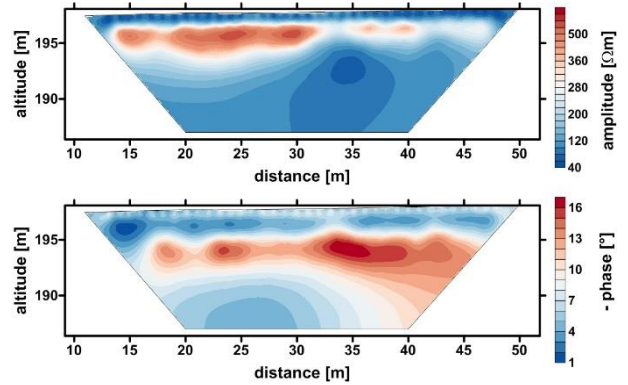

Figure 3: SIP results from profile 5 for 1.25 Hz. Top: amplitude, bottom: phase. The covered slag material is defined by higher resistivities and high phases.

Both profiles show that the slag material here is characterized by higher resistivities and very high phase values. With the development of a new approach for the simultaneous fitting of the whole spectral field data set to different models (here Cole-Cole for example) we are now in a position to obtain chargeability and time constant for both profiles (Günther & Martin, 2016). With the relationship found in the laboratory data, conclusions about mineral concentration and grain size should now be possible.

In Figure 4 the results for profile 5 can be found for the chargeability *m* (top), time constant τ (middle) and the relaxation exponent *c* (bottom). The chargeability of the supposed slag layer is around 0.7-0.8. The very noticeable layer with higher time constants shows values around 3 s.
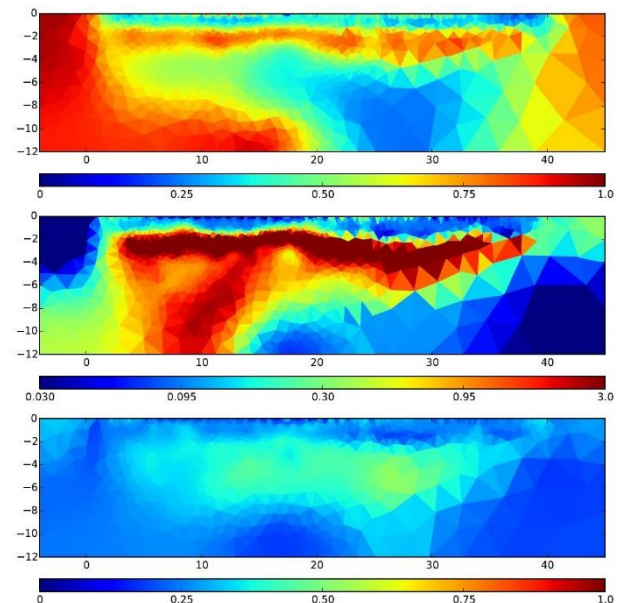

Figure 4: Fit of Cole-Cole parameters for each model cell of profile 5. Top: chargeability *m*; middle: time constant τ; bottom: relaxation exponent *c*.

Laboratory results of the slag samples

From the collected slag chunks various samples were cut and measured. In Figure 5 two samples from profile 3 (SK 1 - red) and two samples from a further profile (SK 2 - blue) can be seen. Analogue to the field results the red samples show high

resistivities (> 1000 Ωm). The phase values are significant (~ 5-6°) but not as high as in the field measurements. In contrast, the blue samples behave differently. Although only 50 m away from profile 3, the SIP characteristics are very different. These samples show much lower resistivities (< 50 Ωm) and very high phases (up to ~ 40°) with a clear maximum at 0.1 Hz resp. 0.01 Hz.

In Table 1 some selected results from the XRF analysis for both chunks can be seen. The slag residuals show still relatively high minerals content. In Table 2 some results from the MIP measurement are listed. Although the porosity is twice for sample SK 1, an explanation for the different SIP characteristic could not be found until now.
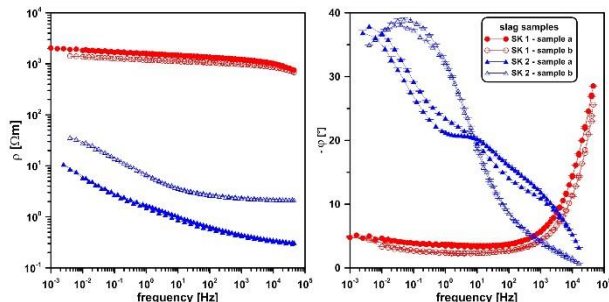

Figure 5: SIP laboratory results for different samples from two slag chunks. Similar to the field results, samples from SK 1 (profile 3 - red) show higher resistivities (> 800 Ωm) and high phase effects (around 5-6°). The blue samples are from another slag chunk (SK 2, but from the same heap) and show different SIP response.

Table 1: Selected results from the XRF Analysis

sample	Ba [%]	Pb [%]	Zn [%]	Cu [%]	Fe2O3 [%]	SiO2 [%]
SK 1	2.65	1.78	8.14	0.68	53.59	18.53
SK 2	3.80	3.83	8.57	0.51	43.55	25.30

Table 2: Selected results from the MIP.

sample	Porosity [%]	Density [g/cm³]	Avg. Pore diameter [μm]
SK 1	7.39	3.62	10.14
SK 2	3.36	3.75	14.42

CONCLUSIONS

In field measurements at a historical slag heap the SIP results show that slag material, which traditionally contains the left over parts, showed high resistivities and high phase values at least for low frequencies. Using the whole spectral information and fitting these data to a Cole-Cole-model allows us to determine chargeability and relaxation time similar to the parameters from Hupfer et al. (2015). Their results show a strong relationship between chargeability and mineral concentration as well as between relaxation time and grain size for pyrite-sand samples. If we extend the fit and locate the parameter values obtained from the field measurements (Figure 1) we calculate mineral concentration of about 10-15% what is conceivable in this area (compare Table 1). The obtained grain sizes in the dm/m area seem much too high for a pure mineral grain but the slag might act as a compact body.

The results from the laboratory measurements of slag samples, gathered in-situ from the profile, indicate that both resistivity and phase are in the same range although we also find samples at the same slag heaps (but few meters away from the profile) which shows very different SIP characteristics.

Generally it seems very promising to investigate historical slag heaps with the SIP method to get information about the residual mineral content and grain size. The investigations of more slag samples from other parts of the slag heaps or/and other slag mining dumps demonstrate that a lot of different slag types exist and according to this very different SIP results could be observed. By ongoing further analysis with mineralogical, optical and chemical methods we try to characterize these differences.

REFERENCES

Cole, K.S. & Cole, R.H., 1941. Dispersion and absorption in dielectrics I. Alternating current characteristics. J. Chem. Phys. 9, 341–351. doi:10.1063/1.1750906.

Florsch, N., Llubes, M., Tereygeol, F., Ghorbani, A. & Roblet, P., 2011. Quantication of slag heap volumes and masses through the use of induced polarization: application to the Castel-Minier site. Journal of Archaelogical Science, 38, 438{451. doi:10.1016/j.jas.2010.09.027.

Florsch, N., Llubes, M., & Tereygeol, F. (2012). Induced polarization 3D tomography of an archaeological direct reduction slag heap. Near Surface Geophysics, 10, 567{574. doi:10.3997/1873-0604. 2012042.

Günther, T. & Martin, T. (2016). Spectral two-dimensional inversion of frequency-domain induced polarisation data from a mining slag heap. Journal of Applied Geophysics, doi:10.1016/j.jappgeo.2016.01.008.

Hupfer, S., Martin, T., Weller, A., Kuhn, K., Günther, T., Ngninjio,V., & Noell, U. (2015). Laboratory SIP measurements at unconsolidated sulphide-sand-mixtures. Journal of Applied Geophysics, doi:10.1016/j.jappgeo.2015.12.003.

Kemna, A., Binley, A., Cassiani, G., Niederleithinger, E., Revil, A., Slater, L., Williams, K. H., Orozco, A. F., Haegel, F.-H., Hördt, A., Kruschwitz, S., Leroux, V., Titov, K., & Zimmermann, E. (2012). An overview of the spectral induced polarization method for near-surface applications. Near Surface Geophysics, 10, 453-468. doi:10.3997/1873-0604.2012027.

Pelton, W., Ward, S., Hallof, P., Sill, W., & Nelson, P. (1978). Mineral discrimination and removal of inductive coupling with multifrequency IP. Geophysics, 43, 588-609.

Radic, T. (2004). SIP256C - Users manual. Radic Research http://www.radic-research.de.

Zimmermann, E., Kemna, A., Berwix, J., Glaas, W., Münch, H., & Huisman, J., 2008. A high accuracy impedance

spectrometer for measuring sediments with low polarizability.
Meas. Sci. Technol. 19. doi:10.1088/0957-0233/19/9/094010.

Influence of plant roots on induced polarization of cultivated soil columns

Sophie Maloteau
UR TERRA, Gembloux Agro-Bio Tech, ULg
2, passage des Déportés
5030 Gembloux
Belgique
sophie.maloteau@ulg.ac.be

Frédéric Nguyen
Bât. B52/3 Géophysique appliquée, Quartier Polytech 1
allée de la Découverte 9
4000 Liège
Belgique
F.Nguyen@ulg.ac.be

Guillaume Blanchy
Gembloux Agro-Bio Tech, ULg
2, passage des Déportés
5030 Gembloux
Belgique
gblanchy@student.ulg.ac.be

Sarah Garré
UR TERRA, Gembloux Agro-Bio Tech, ULg
2, passage des Déportés
5030 Gembloux
Belgique
sarah.garre@ulg.ac.be

SUMMARY

Here the influence of plant roots on geophysical measurements is tested. For this purpose, electrical resistivity (ER) and induced polarization (IP) measurements are conducted on cultivated soil columns with one plant of Brachypodium.

The preliminary results in known media show that acceptable values are obtained from the IP measurements. Even though, we are still testing the specific impact of the electrodes and the column layout on the IP measurements, the decay curves display the expected form and behaviour. The results from this experiment will give us a first idea of the ability of IP to serve as a proxy for the presence of roots in a column. This, combined with ERT and TDR measurements, should lead us to a better understanding of the electrical signature of bulk soil with roots at different soil moisture levels.

Key words: TDIP; roots; soil; pedo-physical relationship; Brachipodium

INTRODUCTION

Geo-electrical methods have been widely used for the last 40 years in many fields: mineral investigation, soil and water pollution, engineering application for subsurface surveys, etc (Reynolds, 2011). Many factors can influence the electrical properties of a media, and thus influence the electrical resistivity (ER) and induced polarization (IP) measurements. Among those factors, it has been observed occasionally that plant roots affect bulk electrical resistivity and electrical induced polarization(Waisel et al., 2002; Kemna et al., 2011; Vanderborght et al., 2013). However, this impact is not yet well understood. The goals of this experiment are to quantify the effect of plant roots on electrical properties of the soil subsurface and particularly on IP measurements.

METHOD AND RESULTS

For this research, it is assumed that roots system affect the electrical properties of the rhizosphere. Indeed the root activity (by transporting ions, releasing exudates, changing the soil structure,…) will cause changes in rhizosphere sufficient to be detected by geophysical measurements. This experiment is included in a bigger research project, eROOT, about the influence of roots system on geophysics measurements.

In this experiment, 6 cylindrical columns (Φ=20 cm, h=45 cm) are filled with repacked saturated loam: Two columns are made of transparent plexi in which 40 electrodes are inserted (5 levels of 8 electrodes) and connected to the MPT-DAS machine (Figure 1).
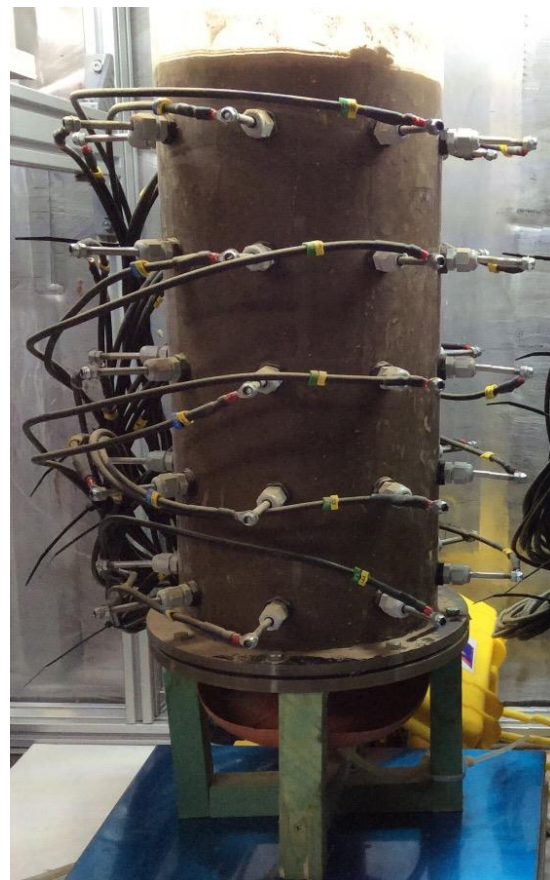

Figure 1. One column of soil connected to 40 electrodes for ERT and IP measurements.

Each of those 2 columns is placed on a scale. Resistivity and chargeability (with 11 time windows) are measured on the first column, whereas only resistivity is measured on the second column because 4 TDR probes are inserted between each level of electrodes. The 4 other columns are made of grey plastic cylinders pre-cut in 5 pieces corresponding to the 5 electrodes levels and for which the RLD (Root Length Density) is measured at each development stage of the plant (Figure 2).

The experiment takes place in a container where the air temperature, the photosynthetically active radiation (PAR), the photoperiod and the relative humidity are controlled and measured.

We have sown one seed of Brachipodium distachyon (L.) Beauv. in each column.

When the plant is big enough to support saturated conditions, the columns are irrigated till saturation (Day 1). From that day, no irrigation will be applied until the end of the experiment in order to observe a drying cycle.

Measurements begin at Day 1 and will continue for 2 months. ERT and IP measurements (vertical and horizontal dipole-dipole array) are conducted twice a day while TDR probes and scales are measuring continuously. Parameters of the controlled environment of the container are also measured permanently.

Preliminary results of electrical resistivity (Ohm m) and phase angle of IP measurements (mrad) for columns obtained during the testing phase with (1) saturated sand, (2) ½ saturated loam and ½ water, and (3) only water and one submerged root system of Brachipodium, are shown in Figure 3 and Figure 4.

CONCLUSIONS

The preliminary results in known media show that acceptable values are obtained from the IP measurements. Even though, we are still testing the specific influence of the electrodes and the column layout on the IP measurements, the decay curves display the expected form and behaviour. The results from this ongoing experiment will give us a first idea of the ability of IP to serve as a proxy for the presence of roots in a column. This, combined with ERT and TDR measurements, should lead us to a better understanding of the electrical signature of bulk soil with roots at different soil moisture levels.

ACKNOWLEDGMENTS

REFERENCES

Kemna, A., Kelter, M., Pfeifer, J., Zimmermann, E., Walter, A., 2011. Imaging and characterizing root systems using electrical impedance tomography. Presented at the AGU Fall Meeting 2011, San Francisco, California, USA.

Reynolds, J.M., 2011. An introduction to applied and environmental geophysics, 2nd ed. Wiley.

Vanderborght, J., Huisman, J.A., Kruk, J. van der, Vereecken, H., 2013. Geophysical Methods for Field-Scale Imaging of Root Zone Properties and Processes. Soil–Water–Root Process. Adv. Tomogr. Imaging, 247–282.

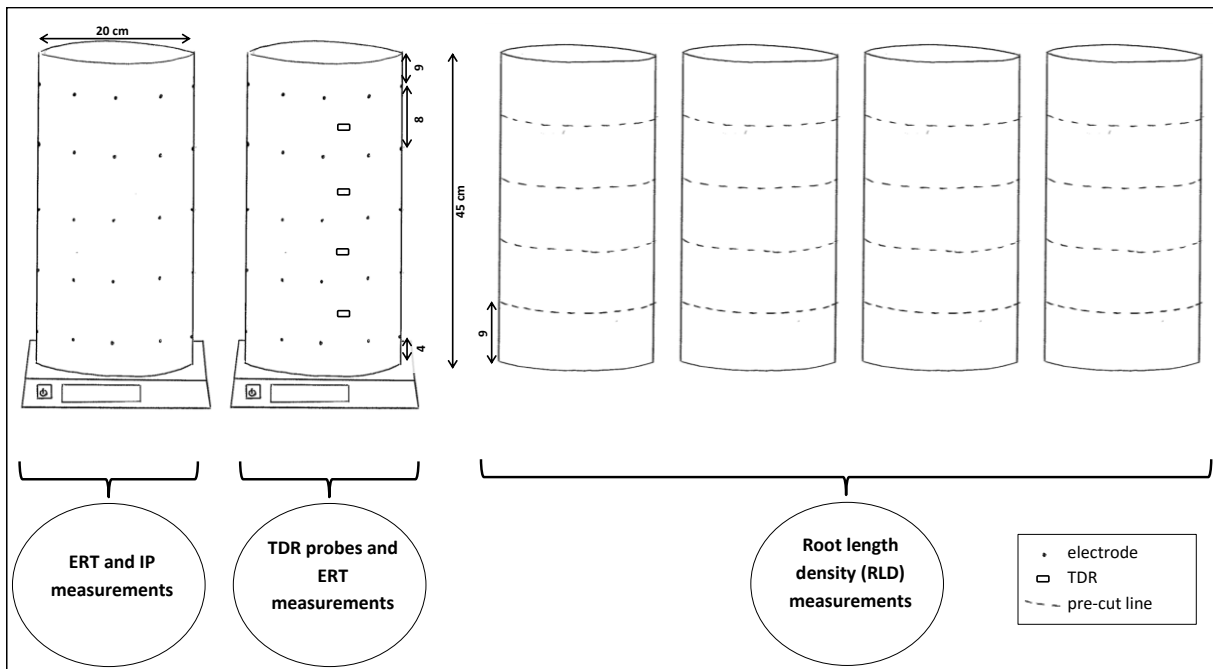Waisel, Y., Eshel, A., Beeckman, T., Kafkafi, U., 2002. Plant Roots: The Hidden Half, Third Edition. CRC Press.

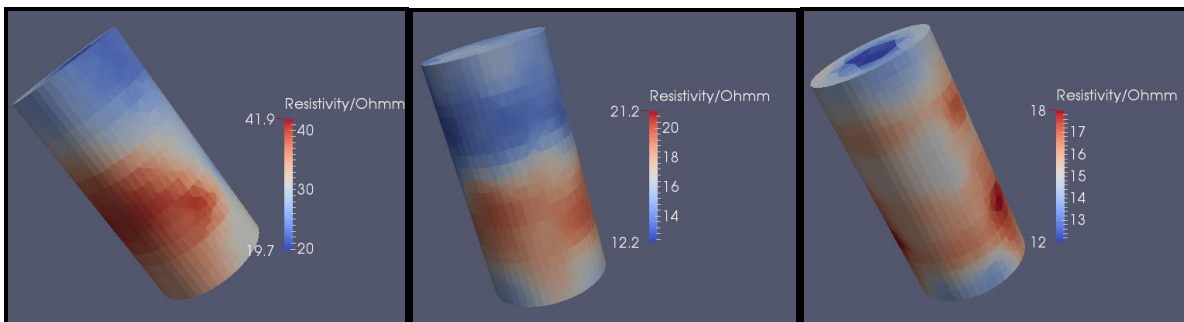**Figure 2. Scheme of the experiment set up.**

Figure 3. Electrical resistivity tomography (Ohm m) of columns with (1) saturated sand, (2) 1/2 saturated loam and 1/2 water, and (3) water only with 1 plant of Brachipodium.
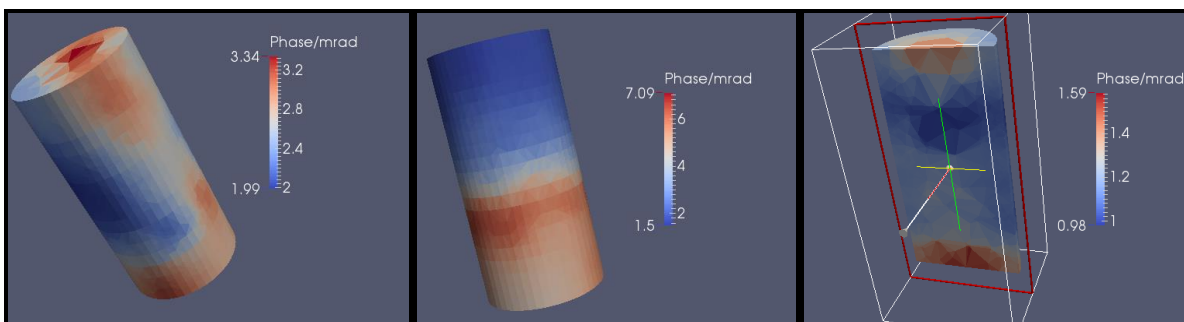

Figure 4. Phase angle tomography (mrad) of columns with (1) saturated sand, (2) 1/2 saturated loam and 1/2 water, and (3) water only with 1 plant of Brachipodium.

Concept of our New Multi-Channel SIP Instrument: SIP256D

Tino Radić
www.radic-research.de
Zehntwerderweg 188A, 13469 Berlin, Germany
radic @radic-research.de

SUMMARY

The quality of SIP measurements is largely determined by the hardware concept of the measuring instrument. High frequency impedance measurements are only possible with the shortest possible current and potential cables. For this, the transmitter should always be located at the electrodes. The current and potential measurement should also be carried out directly at the corresponding electrodes. Our newly developed instrument SIP256D satisfies all these requirements.

Key words: Spectral Induced Polarization, Minimizing Systematic Errors, Expanding Frequency Range.

INTRODUCTION

In the last few years, the number of possible applications of the method of spectral induced polarisation (SIP) has had a notable sharp increase. An example of one such application is the determination of the coefficient of permeability of sand and sandstone, which is important for hydrogeologists (Weller et al, 2010). The assessment of the health of a tree through characteristic features in the impedance spectrum should also be mentioned (Martin et al., 2013). The basis for this was in-depth knowledge gained in the laboratory in the last few years about the connection between petrophysical attributes such as pore space geometry, pore fluid conductivity (Hoerdt et al, 2014) and temperature (Bairlein et al, 2014) of non-mineralised rocks and their resulting frequency dependent electrical impedance. The size of the formation is closely linked with the frequency, at which it is represented in the spectrum. This means that impedance measuring devices must be able to deliver a high quality of data in a wide frequency range. For example, our Chameleon instrument (Radić, 2014) gives measurements between 0.001 Hz and 250.000 Hz - $8^{1/2}$ decades (Figure 1).

THE CHALLENGE

In order to be able to widely use the knowledge gained in the laboratory also in the field, the range of measurement has to be increased to include higher frequencies. Measuring devices for use in the field have to, however, meet further requirements. In this way, a higher progress in measurement and a higher degree of automation are expected of a modern measuring instrument.
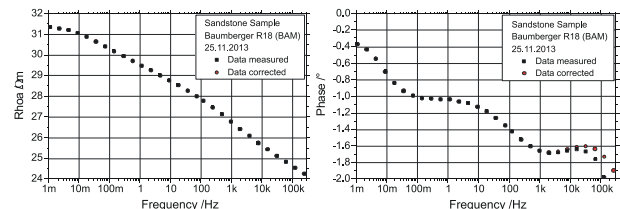

Figure 1. The impedance spectrum of a sandstone (Baumberger R18) shows that IP effects appear in a wide area of frequency. Laboratory measurement with our Chameleon instrument.

For geoelectric direct current measurements the concept of a multi-channel multi-electrodes instrument has established itself. (Figure 2). This concept has, however, for IP measurements limited suitability. Measurement results are already systematically and irreversibly biased at frequencies from ~10 Hz. An analysis of this concept shows that the cause of this is not the electronics themselves, but is the cable, which connects the electrodes with the electronics. (Dahlin, 2012). There is a multitude of coupling effects because of the capacity of the cable. These increasingly bias the impedance measurements with a higher frequency. With our SIP256C Multi-Receiver instrument (Figure 3), the most important of these coupling effects can be avoided, thus extending the area of frequency to 1 kHz. The most effective method to minimise the effects of cable coupling is therefore to avoid them altogether. This means concretely that one reduces the length of each cable to its necessary minimum. Additionally, it is necessary to avoid a parallel cable run. We have already made an important first step with our SIP256C instrument by establishing the current and voltage measurements directly at the electrodes.
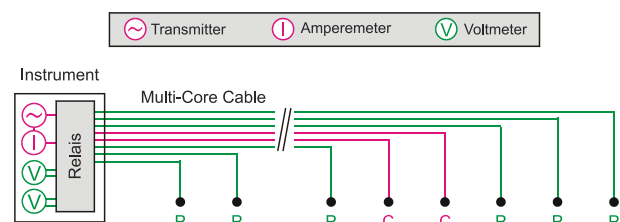

Figure 2. Schema of a typical multi-electrode instrument for geoelectric measurements. The electronics for voltage and current measurements are located together with the transmitter in one casing. A multicore cable is used to connect the electrodes (P, C) with the electronics. Typical cable lengths are tens up to hundreds of meters. Capacitive coupling between the cables and the soil results in systematic data errors.
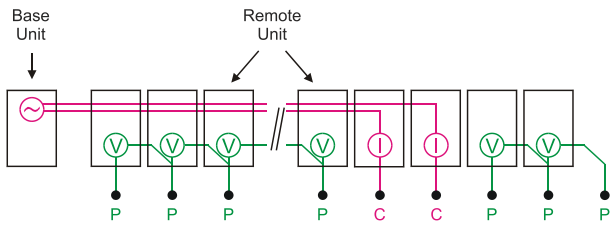
Figure 3.   Schema of our multi-receiver instrument SIP256C. Remote Units are used to measure currents and voltages direct at the electrodes. Thanks to the short potential cable, undesired coupling effects are significantly smaller as with a multi-electrode instrument (Figure 2).

For this, a Remote Unit is located at each electrode. Thus, the lengths of the potential lines are reduced to a minimum; namely to the distances between the pairs of potential electrodes. Furthermore, with this concept configurations of measurements (dipole-dipole) can be chosen with which the current and potential cables do not run parallel. This fundamentally distinguishes our concept from most other multi-electrodes instruments, which assemble the entire measuring electronics in one place, and which connect to the electrodes via long multicore cables. With our SIP256C, it was possible for the first time to obtain high value measurements up to 1kHz with medium size arrays and moderate soil conductivity conditions. With worse conditions (larger cable lengths, variable contact resistance of electrodes), measurement results at the highest frequencies still turn out unsatisfactory. The course of this is the capacitive coupling of the electrical cable with the ground. We were able to solve this problem by actively shielding the current cable. A modified SIP256C instrument (Figure 4a), which we created for Aachen University (Germany), shows that with it this coupling effect can be extensively suppressed (Radić et al., 2012). A separation of the current cable and the potential cable is not, however, necessary (Figure 4b).
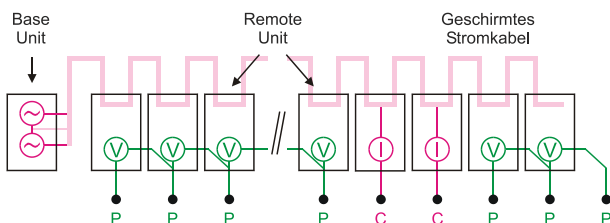

Figure 4a.   Schema of the modified SIP256C instrument. The electrical cables (pink) are actively shielded and furthermore separated from the potential cables (green) with a distance of 1m.
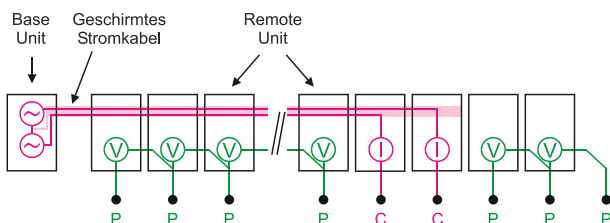

Figure 4b.   The same schema as in Figure 4a, however, here the shielded cables are not set-up separately from the potential cables.

THE NEW HARDWARE: SIP256D

Our current concept has to be further developed to achieve even higher frequencies (20 kHz). In particular it is essential to minimise the length of the electrical cable. This, however, cannot be realised with a central transmitter, as used in the SIP256C. Instead, each of our Remote Units have to be equipped with their own transmitter (Figure 5). The length of the current cable is then identical to the distance of both current electrodes, and for this reason it is as short as possible. However, also the remaining short current cable exhibits a low capacitive coupling with the ground. The resulting parasitic leakage current is dependent on the voltage difference compared to the ground. If the potential difference was successfully minimised then the leakage current would be minimal and would no longer bias the impedance measurement. To achieve this, both transmitters located at the current electrodes are connected in series. Now the current strengths are compared just as with the CE-compensation with a shielded current cable and are measured by both the RUs, which are located at the current electrodes. If they do not match, then the voltage of one the transmitters is increased and the voltage of the other is decreased. The overall voltage stays the same. An automatic algorithm calculates in a few steps the setting for matching the current strengths. Now the electrical cable exhibits approximately the level of the ground and systematic mistakes caused by the current cable capacity are minimised. The increased hardware in the Remote Units comes with less hardware in other places. Instead of a Base Unit with an integrated transmitter, only an interface is needed which connects PC and the chain of Remote Units. In addition, the connecting cable between the Remote Units contains just one single unshielded wire for the current. Both of these features save on money, volume and weight.
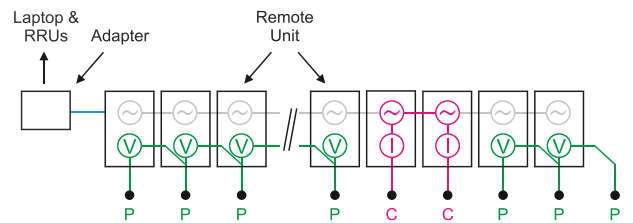

Figure 5.   Schema of our new SIP256D instrument. A transmitter is located in each Remote Unit. With this, the length of the electrical cable is reduced to a minimum.

BUILT-IN TRANSMITTER

To equip each Remote Unit with its own transmitter presents a challenge in various ways. The transmitter has to be cost effective, compact, light and equipped with a high degree of efficiency. Unfortunately, transmitters for sinusoidal signals, such as the ones that we have successfully used for many years, do not exhibit these features.
The above challenges would at best be satisfied with a transmitter that is especially constructed to generate rectangular signals. From a theoretical viewpoint, rectangular signals should be just as suitable for high value SIP measurements. The fact that rectangular signals exhibit a large harmonic wave spectrum urges caution.
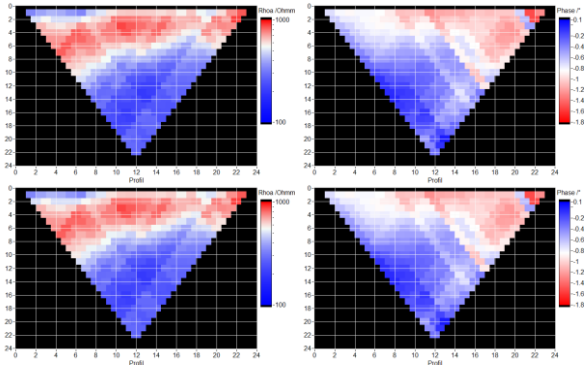
Figure 6. Amplitude and Phase of the resistivity at 80 Hz. Top: Sinusoidal Signal, Bottom: Rectangular Signal. Location: Lübars (Berlin, Germany). Configuration: Dipole-Dipole, a=0.5 m.

On the one hand, the requirements for the linearity, speed and stability of the signal processing electronics are even higher with a rectangular signal. On the other hand, with the appearance of EM-effects, the amplitudes of the harmonic waves decrease more slowly with the distance as those of the fundamental frequency. The result is distinct overshooting at the flanks of the receiver signals. Field measurements with a modified SIP256C instrument show, however, that at least with small and medium distances between electrodes, a moderate specific conductivity of the ground and frequencies at least up to 1kHz show no loss of quality (Figure 6). A further challenge results from the necessity to power the transmitters from the Remote Units' internal batteries. Until now, the concept envisaged a single 50 watt transmitter, which is used for all current dipole configurations. Power for 10 hours requires 500 watt*h of energy. If one divides this energy between typically 20 Remote Units then the result is an energy requirement of 25 watt*h for each Remote Unit. This energy can, for example, be provided by a 12 V NiMh battery pack with 2.1 Ah. Due to the fact that two built-in transmitters are normally connected in series, the aimed for total power of 50 watt is reached.

EXTERNAL TRANSMITTER

The use of two mobile transmitters presents a cost effective alternative to using built-in transmitters (Figure 7). This variation requires, however, that the user personally moves the transmitters step for step along the profile.
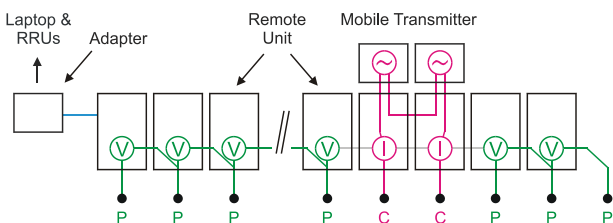

Figure 7. Same schema as in Figure 5, but instead of a built-in transmitter, two mobile transmitters are used. This variation costs less and allows the use of stronger transmitters. However, it requires that the user themselves changes over the transmitters.

For this, both transmitters are to be connected to both Remote Units respectively, which are currently responsible for the power input. We can provide an external transmitter with up to 600 watt, while the performance of a built-in transmitter is limited to only 25 watt. A higher performance is also possible if needed. For this, the power input is not longer realised via the Remote Units, but via separate electrodes.

CONCLUSIONS

Laboratory measurements prove that the structure of the porosity of non-mineralised rock is shown in the impedance spectrum. Measuring instruments have to be able to deliver high value IP data in a broad frequency area in order to record as much information as possible about the structure of the substrate also in field use. Alternating current measurements with multi-channel instruments are, however, biased through capacitive coupling effects between the measuring cable and the ground. An improved measuring concept avoids the most frequent sources of error and thus allows SIP measurements of up to 20 kHz.

REFERENCES

Bairlein, K., Hoerdt, A., Buecker, M. and Nordsiek, S., 2014, Experimental and theoretical studies of the temperature dependence of the spectral induced polarization (SIP) based on a membrane polarization model: Ext. Abstract, 3rd International Workshop on IP, Oleron Island, France, 6-9 April 2014.

Dahlin T. and Leroux V., 2012, Improvement in time-domain induced polarization data quality with multi-electrode systems by separating current and potential cables: Near Surface Geophysics, 2012, 10, 545-565.

Hoerdt, A. and Buecker, M., 2014, The salinity dependence of SIP parameters studied with an extended model of membrane Polarization: Ext. Abstract, 3rd International Workshop on IP, Oleron Island, France, 6-9 April 2014.

Martin, T. and Guenther, Th., 2013, Complex Resistivity Tomography (CRT) for fungus detection on standing oak trees: European Journal of Forest Research (2013) 132 (5-6), 765-776.

Radić, T. and Klitzsch, N., 2012, Compensation Technique to Minimize Capacitive Cable Coupling Effects in Multi-Channel IP Systems: Ext. Abstract, P81, Near Surface Geoscience 2012 - 18th European Meeting of Environmental and Engineering Geophysics, Paris, France, 3-5 September 2012.

Radić, T., 2014, Measuring IP Effects at high frequencies. First lab and field data from 0.001 Hz - 250 kHz: Ext. Abstract, 3rd International Workshop on IP, Oleron Island, France, 6-9 April 2014.

Weller, A., Nordsiek, S. and Debschütz, W., 2010, Estimating permeability of sandstone samples by nuclear magnetic resonance and spectral-induced polarization: Geophysics 75, 215-226.

Spectral Inversion of SIP field data using pyGIMLi/BERT

Thomas Günther
*Leibniz Institute for Applied
Geophysics (LIAG)
Stilleweg 2
D-30655 Hannover, Germany*
Thomas.Guenther@liag-hannover.de

Tina Martin
*Federal Institute for Geosciences
and Natural Resources (BGR)
Wilhelmstr. 25-30
D-13593 Berlin, Germany*
Tina.Martin@bgr.de

Carsten Rücker
*Berlin Institute of Technology
Institute f. Applied Geosciences
Ernst-Reuter-Platz 1
D-10623 Berlin, Germany*
Carsten.Ruecker@tu-berlin.de

SUMMARY

With the developing SIP instruments there are increasing applications of spectral induced polarization in the field. The spectral content of the electric parameters has the potential of characterizing the subsurface and must therefore be retrieved from inversion. Up to now there is no open available inversion package for researchers.

We present the open-source library pyBERT, a C++-Python library for inversion of field resistivity data. It is able to analyse the measured spectra with a variety of different approaches. A Python manager class allows non-programmers to access and visualize in different ways and includes pre-processing of the data as well as post-processing of results, e.g. fitting Cole-Cole models.

We give an impression on how to use these codes and present results based on a synthetic model demonstrating that spectral parameters can be reliably retrieved.

Key words: field SIP, spectral inversion, programming, open-source software, slag heap.

INTRODUCTION

Resistivity is a key parameter in many applications in the field of hydrology, engineering geology or exploration. Besides resistivity, i.e. energy loss, the ability of polarization, i.e. energy storage, can reveal important properties like mineral content or dominant pore size. Laboratory measurements are usually done in the frequency domain over a wide frequency range from mHz to kHz. The magnitude and phase spectra are either fitted with Cole-Cole models (Pelton et al., 1978) or decomposed using Debye or Warburg models (Nordsiek & Weller, 2008; Florsch et al., 2014).

Contrary to the laboratory measurements, field measurements are usually conducted in time domain (TD), i.e. the full wave form of the voltage is recorded. Traditionally, only an integral value, the total chargeability, was used for imaging. However, the spectral inversion on dominant relaxation time is lost then. Fiandaca et al. (2013) presented a method to retrieve Cole-Cole parameters from inverting the full decay.

However, the resolvable bandwidth of available time-domain instruments is restricted by limitations of the source signal and the recording gates. Frequency-domain (FD) instruments are able to cover much wider ranges, however at the cost of significantly increased measuring time. Up to now, there is only a limited number of publications on FD field SIP.

In this work we focus on the analysis of frequency-domain data, i.e. data sets of magnitude and phase for a number of measured frequencies. The easiest approach is to treat each data set independently. An improvement could be made by subsequent inversion using the preceding frequency as a starting or reference model. Other ways are simultaneous inversion of all data with smoothness constraints along frequency or with respect to Cole-Cole parameters (e.g. Routh et al., 1998; Loke et al., 2016). While before mostly approximations for small phases have been used, Kemna (2000) proposed fully complex calculation of the governing partial differential equation and solved the inverse problem in two steps, first for magnitude and then improving the phase.

Up to now, there is no open available code that includes spectral inversion of SIP data. We present a code within the BERT software, is based on the software library GIMLi, that uses a variety of different inversion approaches and includes pre- and post-processing of data and models.

SIP INVERSION METHODS

Single-frequency inversion

We use the triple-grid inversion approach described by Günther et al. (2006). In 2D, the subsurface is discretised by using triangular meshes with the advantage that including arbitrary topography can be described. Whereas a coarse mesh is used for inversion, a refined mesh is used for the forward calculation using the secondary field approach (Rücker et al., 2006). On a highly-refined mesh the primary potentials are computed by using quadratic shape functions. A Fourier transform is used to solve the 3D source problem into 2D (Loke et al., 2006) using Gauss-Legendre and Gauss-Laguerre wavenumber integration (Kemna, 2000).

A Gauss-Newton algorithm is used to minimize the error-weighted data misfit along with the roughness of the model (Günther et al., 2006). Weighting of the two terms is achieved by a regularization parameter that is determined such that the smoothest model that is able to fit the data is found.

After resistivity inversion, the measured phase is inverted using a low-phase approximation as done by Martin & Günther (2013), i.e. the imaginary resistivity is the model parameter. Alternatively, a fully complex calculus (e.g. Kemna, 2000) can be used for calculating of the forward response and also the Jacobian matrix. Logarithmic transforms are used to keep both data and model positive (Kim & Kim, 2011).

In time domain, where apparent chargeability is measured by integrating the voltage curve, one could also use the low-phase approximation. Another way incorporates a second real-valued inversion of higher-frequency data with the first model as reference model, which are the only TD implementations so far.

Multi-frequency inversion

The data of the individual frequencies could be independently inverted. However, the ambiguity inherent in the inversion leads to artifacts so that the spectral information can easily be lost. We use the fact that all underlying relaxation processes (as described by Debye, Warburg or Cole-Cole models) generally exhibit smooth spectra and apply smoothness constraints along the frequency axis.

The apparent resistivities of all frequencies are inverted simultaneously for frequency-dependent resistivity as described in detail by Günther & Martin (2016). The data vector comprises all sub-vectors and the model vector accordingly. The Jacobian matrix has a block-diagonal behaviour.

$$J = \begin{bmatrix} J_1 & \cdots & 0 \\ \vdots & \ddots & \vdots \\ 0 & \cdots & J_N \end{bmatrix} \quad (1)$$

where the matrices J_i are the Jacobian matrices for a number of N individual frequencies. The regularization is applied on both the spatial and the spectral axis, i.e. neighbouring cells of the same frequency and the same cells with neighbouring frequencies are involved by the derivative operator. After magnitudes, the same is done for the phases and another coupled inverse problem is solved, before further analysis of the results follows.

A completely different way of discretization consists in describing each model by a sum of Debye (or Warburg) terms, i.e. a Debye decomposition (Nordsiek & Weller, 2008)

$$\rho = \rho_0 \left(1 - \sum_{k=1}^{K} m_k \left(1 - \frac{1}{1 + i\omega\tau_k} \right) \right) \quad (2)$$

with a number of K predefined relaxation constants τ_k and associated spectral chargeabilities m_k that are inverted for. Each model cell owns a Debye spectrum that is used to derive mean relaxation times and total chargeability values. The size of the model space is comparable, but the Jacobian matrix involves further derivatives. This is also the case for a direct inversion for Cole-Cole parameters where the resistivity of each model cell is described as follows:

$$\rho = \rho_0 \left(1 - m \left(1 - \frac{1}{1 + (i\omega\tau)^c} \right) \right) \quad (3)$$

IMPLEMENTATION

The pyGIMLi framework

We use the open-source framework GIMLi (Geophysical Inversion and Modelling Library), a C++ library that includes performance-critical parts as finite element analysis and equation solvers. Boost is used to bind the whole library to the modern and flexible free programming language Python, in which most of the logical code is written. See www.pygimli.org for a documentation of the individual modules consisting of mesh generation, solvers and different geophysical methods.

pyGIMLi includes a class for handling SIP spectra (as they arise in the lab or in the field) that comprises different ways of plotting, removal of electromagnetic coupling, or fitting. Although all important part are available as functions, data are organised in a class which makes using the individual methods easy and intuitive.

An example code looks as follows

```
from pygimli.physics import SIP
sip = SIP('example.txt')  # read data
sip.showData(norm=True, KramersKronig=True)
sip.removeEM(epsilon=True)
sip.fitColeCole()
sip.showAll(savePDF=True)
```

pyGIMLi is able to do fully constrained models, e.g. for time-lapse or laterally constrained inversion in an efficient way. The Jacobian matrix (1) is a block diagonal matrix that stores only references to the Jacobians of the individual forward operators, whose forward responses are pasted together to yield the model response. So if a single inversion comprises a number of D data and a number of M model cells, only NxDxM entries are stored instead of NxDxNxM.

pyBERT and SIP inversion

BERT (Boundless Electrical Resistivity Tomography, Günther & Rücker, 2012) is a package built upon GIMLi. Besides the classical command line based inversion with configuration files there are also Python bindings called pyBERT. They include a resistivity class that handles single frequency (FD) or total chargeability (TD) data. On top of this, a specialized class SIP2d was designed for handling complete multi-frequency data. Up to now it reads the format of the Radic instruments (www.radic-research.de) and can visualize spectra or pseudo-sections (and export multipage pdf files of it), run different inversion approaches and do post-processing and model output. An example code reads as follows:

```
from pybert.SIP import SIP2d
sip = SIP2d('example.res')  # SIP256C file
sip.generateSpectraPDF(maxdist=20)
sip.generateDataPDF(kmax=50000)
sip.removeEMTerms(Pelton=True)
sip.invertSingleFrequency(f=0.625)
sip.invertSimultaneous(maxF=200)
sip.fitColeColeModel(show=True)
sip.saveResults()
```

We test the approach by using a synthetic model.

SYNTHETIC MODEL

We make use of a synthetic model consisting of a shallow slag heap body with two different relaxation constants (Fig. 1). The resistivities are quite homogeneous in the subsurface. Only the slag bodies are highly polarisable with different relaxation constants of 0.1 and 1.0 s and a common c of 0.5.
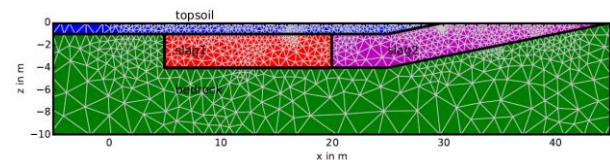

Figure 1. Synthetic model of a shallow slag heap, divided into two parts (r=200 Ωm, m=0.8/0.7 and τ=0.1/10 s) over a 500 Ωm bedrock and partially covered by a 100 Ωm topsoil (after Günther & Martin, 2016).

We show inversion results of noisified synthetic data for four frequencies (Fig. 2). The bottom of the slag is well found from resistivity which does otherwise not distinguish more.
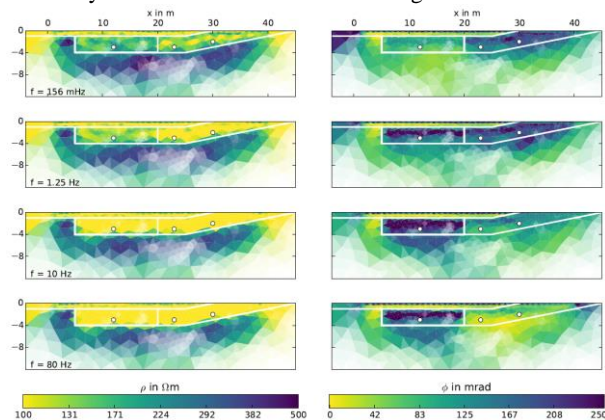

Figure 2. Resistivity (left) and phase (right) from inversion of synthetic data for four selected frequencies (156 mHz, 1.25 Hz, 10 Hz, and 80 Hz).

The phase delineates the slag body and shows maximum values for the right part at low frequencies, whereas the left part shows up for higher frequencies.

We test the method by extracting the resistivity and phase values of selected model cells inside the slag body (see markers in Fig. 2). The general trend of decreasing resistivity and phase maxima at low frequencies is obvious (Fig. 3). The values are then fitted by a Cole-Cole model.
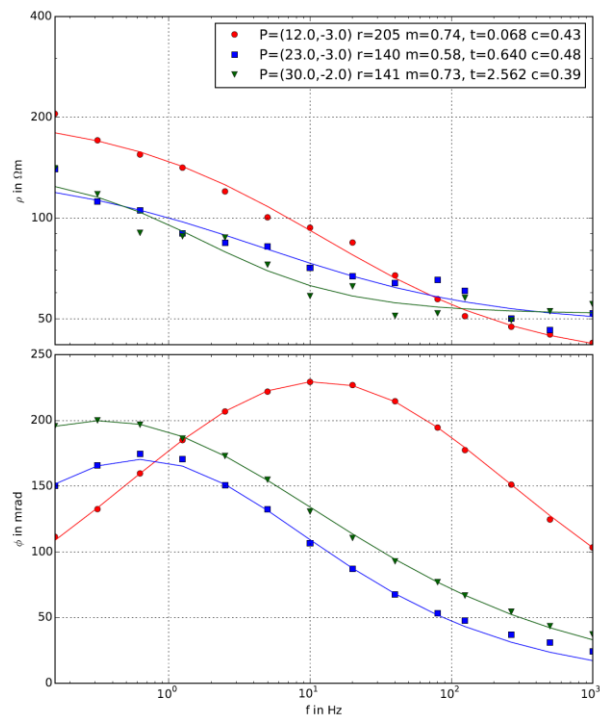

Figure 3. Cole-Cole fit for synthetic inversion results of three slag model cells (see markers in Fig. 2 for positions).

Whereas the resistivity of the first cell is retrieved correctly, the other two are underestimated by about 30% due to the low contrasts in the model and the used smoothness constraints. However, the retrieved values for chargeability are quite close to the synthetic values given in Fig. 1, although the time constant of point 3 is too high. In general it reveals that the

spectral behaviour is determined very well by the phases, whereas the resistivity spectra show undulations and make it hard to retrieve spectral properties.

After all model cells have been fitted by the same routine, we obtain images for chargeability, time constant and relaxation exponent (Fig. 4). The chargeability shows increased values at the centre, but also at the surface and at depth. The time constant shows the correct values for the two slag bodies, but the anomalies are smeared towards the bottom. Interestingly, the exponent also delineates the slag body (with a too deep lower boundary) with correct values of about 0.5 whereas the other cells show values of about 0.25 (the starting values).

In total, looking at all properties simultaneously the slag can be delineated and the two parts can be clearly distinguished by their relaxation constant. The curves are very smooth in contrast to individual inversion results. Simulations with much lower synthetic chargeability increase the undulations in the phase and improve the chance that the spectral behaviour is retrieved by resistivity only. However, these results are highly depending on the used error models. Further systematic parameter studies are needed to fully assess potential and limits.
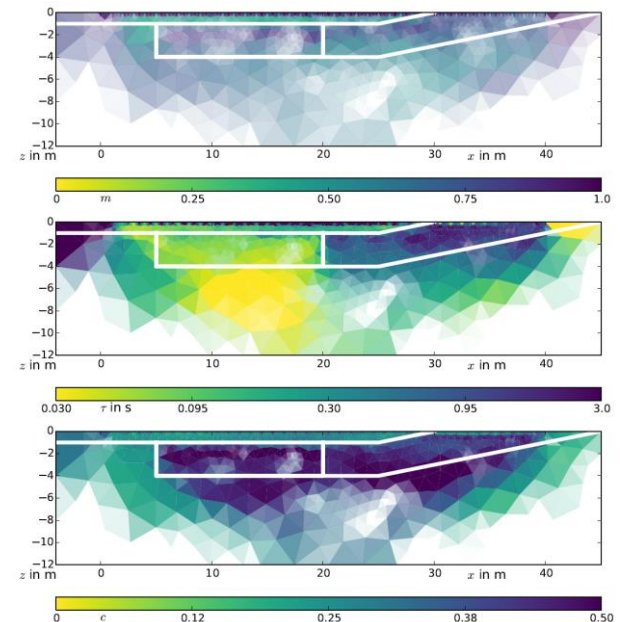

Figure 4. Result of Cole-Cole fit for all model cells showing chargeability (top), time constant (middle) and exponent (bottom). White lines denote the synthetic model boundary.

CONCLUSIONS

The presented software pyGIMLi/BERT is an open-source framework for resistivity inversion that also includes the processing of spectral induced polarization data in the frequency domain. As a generally applicable model, it includes constrained inversion of all frequencies simultaneously which is efficiently achieved by using block matrices.

Synthetic models based on Cole-Cole parameters show that the spectral parameters chargeability and time constant can be reliably retrieved by a fit of the obtained resistivity or phase spectra. Inversion of field data from a historic slag heap demonstrates the applicability to field data (Günther and Martin, 2016).

Further development could be achieved by extension to time domain SIP data. The tool could be used for extensive modelling studies for rigorous comparison between both approaches or to design optimum survey design for a given target. Although spectrally constrained inversion or discretisation by Debye or Warburg models are general approaches that do not require a specific behaviour, direct inversion for Cole-Cole parameters potentially yields the most reliable results in specific cases. However, the presented spectrally constrained inversion can present suitable starting models.

ACKNOWLEDGMENTS

REFERENCES

Fiandaca, G., Ramm, J., Binley, A., Gazoty, A., Christiansen, A. V. & Auken, E. (2013). Resolving spectral information from time domain induced polarization data through 2-D inversion. Geophysical Journal International, 192, 631–646.

Florsch, N., Revil, A. & Camerlynck, C. (2014). Inversion of generalized relaxation time distributions with optimized damping parameter. Journal of Applied Geophysics, 109, 119-132.

Günther, T., Rücker, C. & Spitzer, K. (2006). Three-dimensional modeling and inversion of DC resistivity data incorporating topography - Part II: Inversion. Geophys. J. Int., 166, 506-517.

Günther, T. & Rücker, C. (2012): Boundless Electrical Resistivity Tomography (BERT) v. 2.0 - Open Access Software for Advanced and Flexible Imaging. Ext. Abstr., Schlumberger Symposium of 100 years ERT, Paris 10/07/10.

Günther, T. & Martin, T. (2016). Spectral two-dimensional inversion of frequency-domain induced polarisation data from a mining slag heap. Journal of Applied Geophysics, doi:10.1016/j.jappgeo.2016.01.008.

Kemna, A. (2000). Tomographic inversion of complex resistivity. Ph.D. thesis. Ruhr-Universität Bochum.

Kim, H.J. & Kim, Y.H. (2011): A unified transformation function for lower and upper bounding constraints on model parameters in electrical and electromagnetic inversion. Journal of Geophysics & Engineering 8, 21-26. doi:10.1088/1742-2132/8/1/004

Loke, M., Chambers, J. & Ogilvy, R. (2006). Inversion of 2D spectral induced polarization imaging data. Geophysical Prospecting 54, 287–301.

Martin, T. & Günther, T. (2013). Complex resistivity tomography (CRT) for fungus detection on standing oak trees. European Journal of Forest Research, 132, 765–776.

Nordsiek, S. & Weller, A. (2008). A new approach to fitting induced polarization spectra. Geophysics 73(6), F235-F245.

Pelton, W., Ward, S., Hallof, P., Sill, W. & Nelson, P. (1978). Mineral discrimination and removal of inductive coupling with multifrequency IP. Geophysics, 43, 588–609.

Routh, P.S., Oldenburg, D.W. & Li, Y. (1998). Regularized inersion of spectral IP parameters from complex resistivity data. SEG Expanded Abstracts 1998. doi:10.1190/1.1820608.

Rücker, C., Günther, T. & Spitzer, K. (2006). 3-D modeling and inversion of DC resistivity data incorporating topography - Part I: Modeling. Geophys. J. Int., 166, 495-505.

On the Effectiveness of 1D Inversions of TEM Data affected by Induced Polarization

Marc Seidel
Institute of Geophysics and Meteorology
University of Cologne
Albertus-Magnus-Platz, 50923 Cologne, Germany
seidel@geo.uni-koeln.de

Bülent Tezkan
Institute of Geophysics and Meteorology
University of Cologne
Albertus-Magnus-Platz, 50923 Cologne, Germany
tezkan@geo.uni-koeln.de

SUMMARY

In case of a polarizable subsurface, effects of inductively induced polarization (IP) can have an impact on time-domain electromagnetic measurements (TEM) and may lead to nonmonotonous voltage responses or even sign reversals in the recorded transients. For this reason, we developed a new 1D inversion algorithm for the central-loop and the separate-loop TEM configurations using the Cole-Cole relaxation model.

1D forward calculations for a polarizable homogeneous half-space were conducted with the aim of analyzing the impacts of varying Cole-Cole parameters on TEM transients with respect to possible sign reversals. Additionally, we considered the variation of geometrical parameters like the transmitter size and the receiver offset. For the inversion of TEM data, one consequence of these modelings is the large number of equivalences that arise from the additional Cole-Cole parameters.

Subsequently, 1D inversions of synthetic data were performed to study the potentials and limitations of the new inversion algorithm regarding the resolution of the Cole-Cole parameters. The obtained findings were eventually adopted on the inversion of real TEM field data that contained considerable IP signatures such as sign reversals. One field dataset was recorded at the Nakyn kimberlite field in Western Yakutiya, Russia in the central-loop configuration. The second field dataset originates from a waste site in Cologne, Germany, and was measured utilizing the separate-loop configuration.

Key words: TEM, IP, Inversion, Cole-Cole model

INTRODUCTION

While interpreting time-domain or transient electromagnetic (TEM) data, effects of inductively induced polarization (IP) are often neglected. This might lead to misinterpretations of TEM results in case of a polarizable subsurface. These effects vary from nearly imperceptible influences on the transients to the distortion of monotony or even to one or more sign reversals.

Spies (1980) and Smith and West (1989) reported the appearance of sign reversals in transient electromagnetic data obtained by a coincident-loop configuration. These features cannot be interpreted using common 1D interpretation techniques. According to Weidelt (1982), local inhomogeneities or 3D effects can be ruled out as a source of negative voltages when the data is taken in the coincidental-loop configuration. However, these signatures can be explained through dispersive conductivities.

Flis et al. (1989) showed that a polarizable subsurface can trigger polarization currents due to the separation of charges during the downward transit of the inductive currents. The direction of these relaxing currents is opposite to the direction of the induced currents and may therefore lead to sign reversals in the recorded transients. Whether these IP effects can be observed, and to what extent, depends strongly on the intensity of the polarization currents compared to the measured induction currents.

A possible polarizability leads to a capacitor-like behavior of the subsurface which is commonly described through the Cole-Cole relaxation model (Pelton et al., 1978). In that, one or more layers are assigned with a complex and frequency-dependent resistivity $\rho(\omega)$:

$$\rho(\omega) = \rho_0 \left[1 - m \left(\frac{1}{1 + (i\omega\tau)^c} \right) \right], \qquad (1)$$

where ω is the angular frequency in s^{-1}, ρ_0 is the direct current resistivity in Ωm, m the chargeability, c the frequency exponent (both dimensionless) and τ the relaxation time in s.

The forward modeling of IP effects in transient electromagnetics using the Cole-Cole model has been the studied in several publications over the last decades. The history of the inversion of IP-affected TEM data deploying the Cole-Cole model is much briefer and only a few scientific papers were published so far. Kozhevnikov and Antonov (2006) successfully inverted IP-affected central-loop TEM data recorded over a kimberlite mine in Western Yakutia, Russia (this dataset is furthermore subject to this work).

The same authors studied the inversion potentials of synthetic TEM data affected by fast-decaying induced polarizations for a homogeneous half-space and a two-layered earth (Kozhevnikov and Antonov, 2008 and 2010) and successfully applied an inversion algorithm on central-loop TEM data in permafrost areas providing fast-decaying IP effects (Kozhevnikov and Antonov, 2014). Any aforesaid publication concentrated on the inversion of data measured or calculated in the central- or coincidental-loop configuration.

In this work, we discuss the results of a newly developed 1D TEM inversion algorithm for IP-affected synthetic and field data utilizing the central- and separate-loop configuration. For this, we employed a 1D forward algorithm based on former works of P. Weidelt using the Cole-Cole relaxation model for dispersive resistivities. 1D forward calculations for a homogeneous half-space were conducted with the aim of analyzing the impacts of the Cole-Cole parameters on TEM transients regarding the time and the negative amplitude of possible sign reversals. Subsequently, 1D inversions of synthetic data were performed using the Cole-Cole model to

study the potentials of such an algorithm with respect to the resolution of the Cole-Cole parameters.

The obtained findings were eventually adopted on real field data which provided considerable IP signatures such as sign reversals. One examined field dataset was recorded in the central-loop configuration on the Nakyn kimberlite field in Western Yakutiya, Russia (Kozhevnikov and Antonov, 2006). A second field dataset, measured in the separate-loop configuration, origins from a waste site in Cologne, Germany (Schaumann, 2001).

FORWARD MODELING STUDIES

For the forward modeling studies, a new 1D forward algorithm deploying the Cole-Cole relaxation model was used. Here, the resistivity ρ is replaced by the dispersive resistivity $\rho(\omega)$ (see equation 1).

The electromagnetic fields are calculated in the frequency domain for a given transmitter/receiver configuration. Afterwards, the fields are Fourier-transformed into the time domain using digital filters. The numerical solution of the Bessel integrals was conducted by a fast Hankel transform (Johansen and Sørensen, 1979). In our studies, we always vary one parameter and keep the remaining ones fixed.

The Cole-Cole parameters were chosen in the way that they provide considerable IP effects. Partially, they are slightly exaggerated to facilitate proper studies of these effects. The introduced current was a 1 A step-off function with no ramp. The calculated induced voltage response is proportional to the time derivative of the z-component of the secondary magnetic flux density integrated over a receiver area of 1 m². All calculations were performed for the times from 1 µs to 10 ms using 61 sampling points for each transient.

The most prominent features of IP-affected data are sign reversals and the following negative amplitudes. Therefore, we concentrated on the study of the impacts of the Cole-Cole parameters on the times of possible sign reversals (SR) and the maximum of the subsequent negative response (NR), see Figure 1.
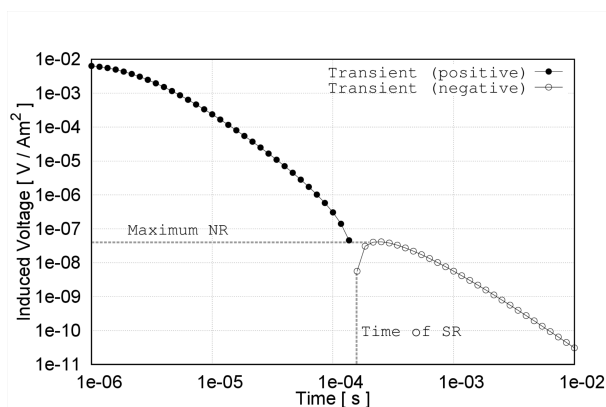

Figure 1. Forward calculated transient data with a sign reversal (central-loop configuration) of the homogeneous half-space with Cole-Cole parameters: $\rho_0 = 100$ Ωm, m = 0.5, c = 0.5, $\tau = 0.001$ s, transmitter loop size 50 m x 50 m.

INVERSION OF SYNTHETIC DATA

Regarding the inversion of synthetic data, we primarily investigated the homogeneous half-space but also examined two and three layer cases. Due to the additional Cole-Cole parameters per layer (m, c and τ), the total number of free parameters in the inversion process increases rapidly making a structured analyses of the inversion results rather complex. An additional challenge is the ambiguity between IP-affected and non IP-affected data. Kozhevnikov and Antonov (2008) showed that the inversion results for synthetic data from a polarizable half-space can also be explained through a multi-layer subsurface model without IP effects.

Figure 2 shows an exemplary successful inversion result of synthetic separate-loop data for a three layer model which consists of a polarizable layer ($\rho_0 = 3$ Ωm, m = 0.5, c = 0.5, τ = 0.001 s) between two non-polarizable layers (both $\rho_0 = 30$ Ωm). The thicknesses are 5 m for first layer and 10 m for the second layer. For the starting model we varied the resistivity of the first layer to 20 Ωm and its thickness to 7 m. The polarizable second layer in the starting model has the values $\rho_0 = 1$ Ωm, m = 0.6, c = 0.5, τ = 0.001 s and its thickness was defined as 8 m. The forward calculated data for the starting model is shown as a dashed line in Figure 2, the inversion result as a solid line. Before the inversion, the synthetic data was imposed with 2% Gaussian noise. The first sign reversal is due to the geometry of the separate-loop configuration, the second sign reversal is attributed to IP effects.
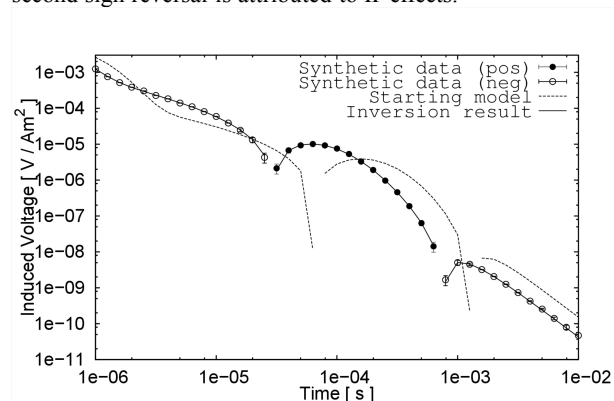

Figure 2. Synthetic data, forward calculated starting model and inversion result of a three-layer case (separate-loop configuration).

INVERSION OF FIELD DATA

To test our new inversion algorithm with field data taken in the central-loop configuration, the group of N.O. Kozhevnikov from the Institute of Geophysics of the SB RAS, Novosibirsk, Russia, granted us access on TEM data which was recorded during a diamond prospection in Western Yakutiya, Russia (Kozhevnikov and Antonov, 2006). This dataset consists of 25 TEM soundings taken with a 200 x 200 m² transmitter loop and a 100 x 100 m² receiver loop along a 5 km profile. Some of these soundings contain two sign reversals while others have no sign reversal but provide a break of monotony and a local minimum. According to Kozhevnikov and Antonov (2006), these IP-like patterns can be attributed to a few meters thin and shallow layer consisting of frozen quartz sands. Therefore, the observed IP-effects occur at very early times and decay very fast. Furthermore, this fast decay is the reason for a second sign

reversal observed on some soundings. Figure 3 shows the data and the inversion result of one exemplary TEM sounding from that dataset.
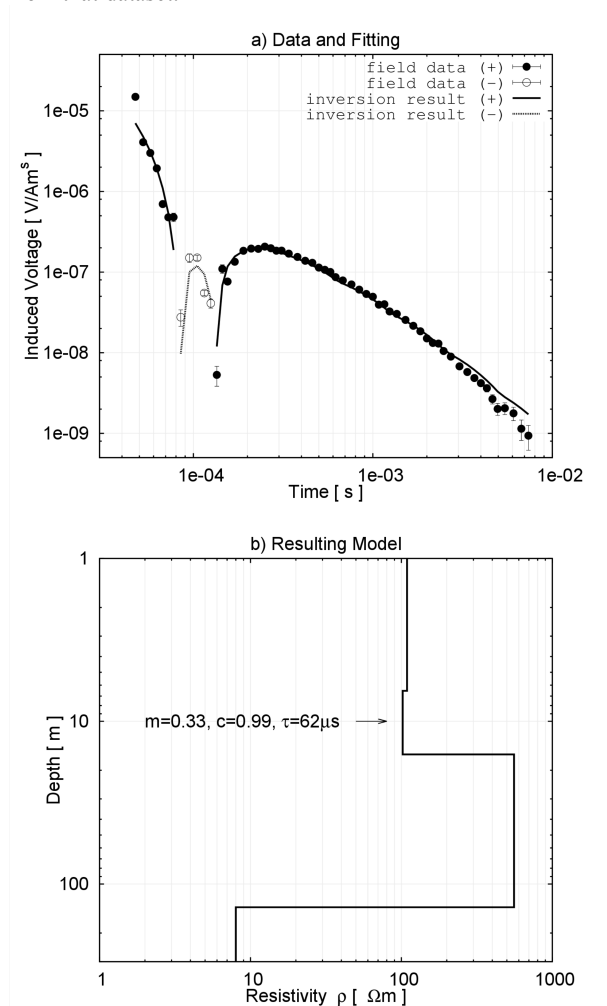

Figure 3. a) Field data and inversion result of one station from the central-loop TEM dataset from Western Yakutiya (Kozhevnikov and Antonov, 2006). b) Resulting model and Cole-Cole parameters of the second, polarizable layer.

The inversion of IP-affected separate-loop TEM data is of greater complexity due to the additional sign reversal. Gerlinde Schaumann of the BGR, Germany, permitted us to use data which was recorded in the separate-loop configuration on top of a former waste site in Cologne Ossendorf, Germany (Schaumann, 2001). The examined dataset consists of 20 TEM soundings taken with a transmitter loop size of 25 x 25 m² and a receiver offset of 25 m. Some of the recorded transients comprise 2 or even 3 sign reversals which may originate from a shallow, polarizable layer.

The inversion of this dataset was challenging and the algorithm was nearly unable to find sound data fittings. These difficulties originate probably from lateral inhomogeneities in the subsurface.

CONCLUSIONS

We investigated the capabilities of a 1D forward and inversion algorithm for IP-affected data in time-domain electromagnetics applying the Cole-Cole relaxation model. For a polarizable homogeneous half-space, the influence of variations of the Cole-Cole parameters and geometrical factors like transmitter size and receiver offset on synthetic transients have been studied utilizing the central-loop and the separate-loop configuration.

One consequence of including the Cole-Cole model in the inversion of TEM is the large number of equivalent models that result from the different parameters. Without the Cole-Cole model (or any other model describing IP-effects), the interpretation of IP-unaffected TEM data already encounters the issue of possible equivalences. With the Cole-Cole model applied, this issue becomes more complex.

The inversion algorithm was tested successfully on synthetic data. We point out that the success of the inversion strongly depends on the choice of a starting model which is inherent to the implemented damped least squares approach. This dependency increases when applying the Cole-Cole model to one or more layers of the starting model.

We successfully carried out inversions of central-loop field data which provided considerable IP patterns. The inversion of separate-loop field data turned out to be more challenging on the available field data which can be traced back to lateral inhomogeneities.

REFERENCES

Flis M. F., Newman G. A. and Hohmann G. W., 1989, Induced Polarization Effects in Time-Domain Electromagnetic Measurements: Geophysics 54, 514–523.

Johansen H.K. and Sørensen K., 1979, Fast Hankel Transforms: Geophysical Prospecting 27, 876-901.

Kozhevnikov N. O. and Antonov E. Y., 2006, Fast-decaying IP in frozen unconsolidated rocks and potentialities for its use in permafrost-related TEM studies: Geophysical Prospecting 54, 383–397.

Kozhevnikov N. O. and Antonov E. Y., 2008, Inversion of TEM data affected by fast-decaying induced polarization: Numerical simulation experiment with homogeneous half-space: Journal of Applied Geophysics 66, 31–43.

Kozhevnikov N. O. and Antonov E. Y., 2010, Inversion of IP-affected TEM responses of a two-layered earth: Russian Geology and Geophysics 51, 708–718.

Kozhevnikov N. O. and Antonov E. Y., 2014, TEM Surveys for seach of taliks in areas of strong fast-decaying IP effects: Russian Geology and Geophysics 55, 1428–1436.

Pelton W. H.,Ward S. H., Hallof W. R., Sill W. R. and Nelson P. H., 1978, Mineral Discrimination and Removal of Inductive Coupling with Multifrequency IP: Geophysics 43, 588–609.

Schaumann G., 2001, Transientenelektromagnetische Messungen auf Mülldeponien - Untersuchung des Einflusses von 3D-Leitfähigkeitsvariationen und 1D-frequenzabhängiger Polarisierbarkeit: PhD thesis, University of Braunschweig, Braunschweig, Germany.

Smith R. S. and West G. F., 1989, Field examples of negative coincident-loop transient electromagnetic responses modeled with polarizable half-planes: Geophysics 54, 1491-1498.

Spies B. R., 1980, A field occurrence of sign reversals with the transient electromagnetic method: Geophysical Prospecting 28, 620–632.

Weidelt P., 1982, Response characteristics of coincident loop transient electromagnetic systems: Geophysics 44, 1325–1330.

IP2016/4th International Workshop on Induced Polarization

Characterization of Abandoned Mine Tailings by means of Time- and Frequency-Domain Induced Polarization Imaging

Jakob Gallistl
TU-Wien

Jakob.Gallistl@geo.tuwien.ac.at

Adrian Flores Orozco
TU-Wien
Gusshausstraße 27-29, 1040-Vienna Austria
Flores@tuwien.ac.at

Matthias Bücker
TU-Wien

Matthias.Buecker@geo.tuwien.ac.at

SUMMARY

Induced Polarization (IP) imaging datasets were collected in both time domain (TDIP) and frequency domain (FDIP) for the characterization of abandoned mine-tailings and in order to assess possible down-gradient transport of sulphide minerals. The study area is characterized by measurable iron and copper concentrations of fine-grained minerals (gain size < 1 mm), which are expected to cause a distinct IP response. This study aims at the evaluation of the applicability of TDIP and FDIP at the field scale, its capability to quantify metallic volumetric content and to discriminate between different metallic minerals. Furthermore, the analyses of water samples down gradient from the tailings have revealed significant concentrations of heavy metals, such as arsenic and mercury. Hence, imaging results of an extensive mapping campaign were used to delineate preferential flow paths of sulphides and the extensions of the contaminated volume.

Key words: frequency domain; time domain; field measurements; imaging; metallic minerals.

INTRODUCTION

There is a growing interest in the characterization of abandoned mine-tailings – on one hand, because of the possible economic value of metal-rich tailings, on the other hand, because of the need to evaluate the environmental impact due to the leaching and migration of heavy metals. Although the analysis of soil and groundwater samples provides direct information about the parameters of interest (e.g., chemical composition, concentration), such characterization is time consuming and does often not provide the required spatial resolution to evaluate the geometry and extension of mineral deposits or contaminated volumes. Furthermore, the relatively high costs of ex-situ characterization methods often render detailed site investigations prohibitively expensive. To overcome these limitations, recent studies (e.g., Jang M, 2009; Peinado et al., 2010) have suggested the use of portable X-Ray Fluorescence Spectrometry (XRFS) devices to determine *in-situ* concentrations of heavy metals and permit the assessment of extensive areas. Although promising, the XRFS technique has a limited investigation depth of a few millimetres.

Geophysical methods are well suited for collecting spatially continuous data. Given the strong induced polarization response observed in presence of electronic conductors (e.g., metallic minerals), the Induced Polarization (IP) method has been established as a standard tool for the exploration of metallic ores (e.g., Pelton et al., 1978). Recent studies have also demonstrated the capability of the IP method to assess changes in the chemical composition of groundwater (Flores Orozco 2011: 2013; Placencia-Gómez, 2014; 2015). Furthermore, petrophysical models have been suggested to quantify the grain size of metallic minerals based on the frequency dependence of the IP response (e.g. Wong, 1979).

In this study we present the application of the IP imaging method for the characterization of an abandoned mine tailing. Extensive field measurements were collected to delineate the geometry of the lithological contacts with high spatial resolution, identify zones at which metallic minerals accumulate and extend the interpretation of IP images towards the quantification of the metallic volumetric content. Measurements were collected in both frequency and time domain (FDIP and TDIP) in order to evaluate the applicability of existing petrophysical models to discriminate between metallic minerals, and to infer dominating grain sizes of the metallic minerals.

METHOD

Initial characterization of the site was done by means of frequency-domain measurements (FDIP). To minimize acquisition time and rapidly assess the main structures at the site, these measurements were collected at a single frequency (1 Hz). FDIP measurements were collected with a DAS-1 system (Multi-Phase Technologies, LLC). Based on the initial characterization, particular areas were selected for the collection of FDIP measurements over a broader frequency bandwidth (0.05 to 200 Hz). For comparison, the same profiles were re-collected in the time domain (TDIP) using a square wave form with 50% duty cycle, a pulse length of 2 s, and 35 linearly distributed IP windows. Selected TDIP profiles were also measured with a Syscal Pro (Iris Instruments) using a 2 s pulse length and 50% duty cycle, but sampling the entire wave form by means of voltage readings every 10 ms. The data were collected using multiple-gradient configurations, similar to those proposed by Dahlin and Zhou (2006). These configurations consist in potential measurements collected between electrodes located within the current dipole. In particular, we collected potential measurements using skip-0, skip-1, skip-2, skip-3 and skip-4 schemes (i.e., increasing the length of the potential dipole by increasing the number of skipped electrodes within the potential dipole). In order to use all eight channels of the DAS-1 equipment, the length of the current dipole was ten times the length of the potential dipole. For the evaluation of data error, selected profiles were also measured as normal-reciprocal pairs using a dipole-dipole configuration with

dipole lengths varying from skip-0 to skip-6. Data error was quantified by means of the statistical analysis of normal-reciprocal readings as described by Flores Orozco et al. (2012a). The inversion of the data was performed with CRTomo, a smoothness-constraint algorithm by Kemna (2000). For the sake of comparability, the inversion of TDIP datasets was performed using a linear conversion of the measured integral chargeability to apparent phase values (at the fundamental frequency of 0.125 Hz), which assumes a constant-phase response (Kemna, 2000).
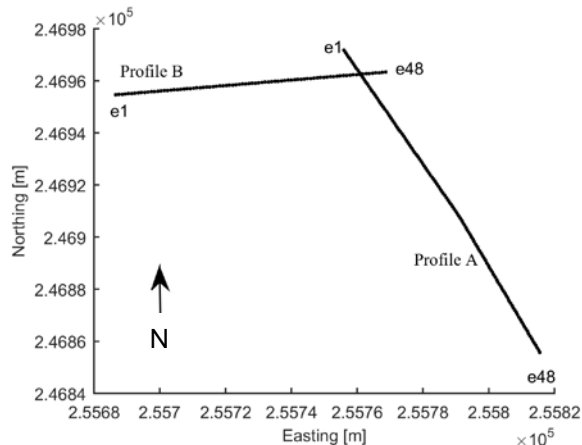

Figure 1. Orientation of the electrical profiles A and B. The position of the first (e1) and last electrode (e48) is indicated for each profile.

Here, we are presenting imaging results obtained for FDIP data collected along two transects: 1) Profile A, which starts 20 m outside of the tailings and crosses the study area from North to South. Measurements were collected with 48 electrodes with a separation of 3 m; and 2) Profile B, which is located down-gradient of the tailings, perpendicular to Profile A (from West to East), using 48 electrodes with a separation of 2 m. A schematic representation with the orientation of profiles A and B is presented in Figure 1.

RESULTS

Imaging results for FDIP data collected at 1 Hz along profile A (Figure 2) reveal three main units. 1) at the beginning of the profile, generally low resistivities (ρ) and phase shifts (ϕ) prevail; 2) between 30 and 60 m along the profile, an anomaly characterized by high resistivities (> 10^4 Ωm) and low phase shifts can be observed; and 3) an anomaly characterized by low resistivity values (< 1000 Ωm) and high polarization response ($-\phi$ > 15 mrad) appears approximately between 60 and 120 m along the profile. The electrical images presented in Figure 2 were intriguing, particularly the anomaly characterized by the extremely high electrical resistivity values. Excavations at the location of the resistive anomaly between 30 and 60 m along the profile revealed a construction waste dump that mainly consists of large rocks and bricks. This was an important finding of the exploratory campaign, as this dump is not described in any of the records of the mine and might have a strong impact on the hydrogeology of the site. However, the shallow anomaly observed between 80 and 120 m, which is also characterized by high resistivity values (~1000 Ωm), is not related to construction waste, but to fine grained sand. Collection of samples at the site revealed the presence of fine-grained metallic minerals at depth (~ 1.5 - 3

m below the surface), which explains the high polarization response ($-\phi$> 15 mrad). XRFS measurements on the sediment cores recovered from drillings at this location reported values between 2000 and 3000 ppm copper. The anomaly observed at the beginning of the profile A, characterized by low resistivity values (<100 Ωm) is likely related to the accumulation of metallic sulphides which are transported down gradient the mine tailing.
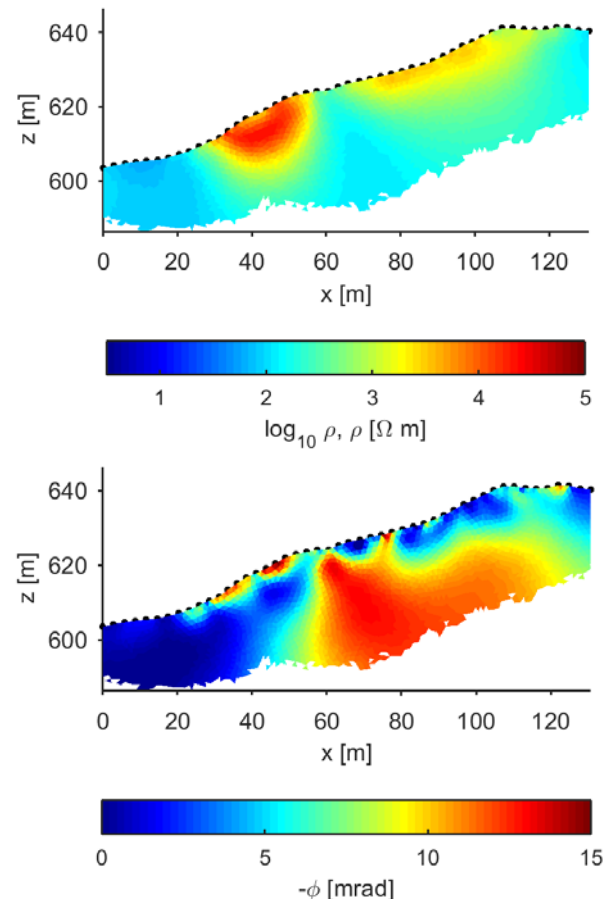

Figure 2. Electrical imaging results for FDIP data collected at 1 Hz along profile A. The complex electrical resistivity is expressed in terms of electrical resistivity (top) and phase shift (bottom). The positions of the electrodes are indicated by black dots.

To better understand the response down gradient the mine tailing and to characterize possible transport and accumulation of metallic sulphides at the foot of the mountain, extensive measurements were collected down gradient the tailings. Figure 3 shows the imaging results for data collected along profile B located in this area revealing low electrical conductivity values, which are likely related to the increase of the metallic content. XRFS measurements on recovered sediments (down to 3 m depth) revealed values varying between 1400 and 10,000 ppm copper and 2.2 ppm mercury. However, such concentrations are a consequence of the down-gradient transport of metallic sulphides. Besides the occurrence of metallic minerals in the subsurface, the low electrical resistivity values are also a consequence of the high clay content observed in collected sediments. Nonetheless, the resistivity image (Figure 3, top panel) exhibits an anomaly characterized by slightly higher resistivity values (~ 100 Ωm),

which is related to sandy materials. At both edges of this resistive anomaly we also observe two anomalies characterized by high phase-shift values ($-\phi >$ 15 mrad), which are correlated with an increase of the metallic content reported by XRFS measurements. Plots in Figure 3 also reveal an increase in the IP response for measurements collected at the lowest frequencies (0.25 Hz), with negligible values observed at higher frequencies (not shown here for brevity). We hypothesize that the increase of the phase shift at the lower frequencies corresponds to the presence of larger grain sizes as predicted by the model of Wong (1979).
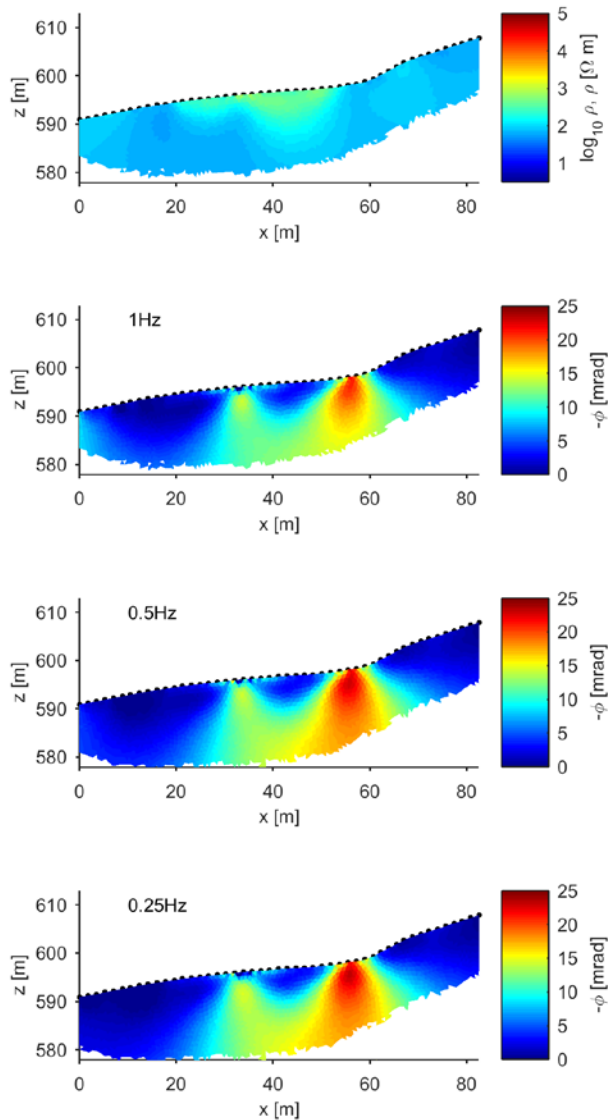

Figure 3.   Electrical imaging results for FDIP data collected along profile B (located down gradient the mine tailing). The complex electrical resistivity is expressed in terms of the electrical resistivity (top) and the phase shift (the last 3 rows) for data collected at three different frequencies (1, 0.5 and 0.25 Hz). The electrode separation for the collection of the data was 2 m.

Although not presented here, the electrical images for FDIP and TDIP datasets reveal consistent results, demonstrating the robustness of the IP technique, independent from the measuring technique. Ongoing work focusses on the quantification of spectral parameters (e.g., Cole-Cole

parameters) to describe the frequency dependence of the observed IP responses. We believe that maps representing the distribution of spectral parameters at the study area, and their correlation with XRFS data, will permit an improved characterization regarding the changes in the composition and grain size of the metallic minerals. Furthermore, we are planning the inversion of the extensive datasets using a full-wave form approach (e.g., Fiandaca et al., 2012) in order to extract spectral parameters also from TDIP measurements.

CONCLUSIONS

Our results confirm the potential of the IP method to characterize the occurrence of metallic minerals in the subsurface, even if the size and concentration of such minerals in mine tailings is much lower than those observed in mining exploration. However, results presented here reveal the large degree of heterogeneity typically observed on mine tailings. Although not a primary objective of the study, IP images permitted the identification of a secondary deposit associated to construction waste, linked to high electrical resistivity values. The characterization of such heterogeneities is critical to fully understand the fate and transport of metallic sulphides. For data collected at 1 Hz, the sediments at the mine tailing presented only a modest polarization response ($-\phi \sim$ 15 mrad); whereas down gradient, the polarization response was larger ($-\phi >$ 20 mrad), with a stronger response observed at lower frequencies (<1 Hz). This indicates transport and accumulation of metallic sulphides down gradient the mine tailings.

REFERENCES

Dahlin, T., Zhou, B.,. 2006, Multiple-gradient array measurements for multichannel 2D resistivity imaging: Near Surface Geophysics 4(2), 113-123.

Fiandaca, G., Auken, E., Christiansen A.V., and Gazoty, A.,. 2012, Time-domain-induced polarization: Full-decay forward modeling and 1D laterally constrained inversion of Cole-Cole parameters: Geophysics 77(3), E213-E225.

Flores Orozco, A., Kemna, A., Zimmermann, E.,. 2012, Data error quantification in spectral induced polarization imaging: Geophysics 77(3), E227-E237.

Flores Orozco, A., Williams, K.H., Long, P.E., Hubbard, S. S., Kemna, A.,. 2011, Using complex resistivity imaging to infer biogeochemical processes associated with bioremediation of an uranium-contaminated aquifer: Journal of Geophysical Research: Biogeosciences 116(G3), 2156-2206.

Flores Orozco, A., Williams, K.H., Kemna, A.,. 2013, Time-lapse spectral induced polarization imaging of stimulated uranium bioremediation: Near Surface Geophysics: 11(5), 531-544.

Kemna, A., 2000. Tomographic Inversion of Complex Resistivity: Theory and Application, Der Andere Verlag, Osnabrück.

Jang, M.,. 2009, Application of portable X-ray fluorescence (pXRF) for heavy metal analysis of soils in crop fields near

abandoned mine sites: Environmental Geochemistry and Health 32(3), 207-216.

Peinado, M., Morales Ruano, S., Bagur González, M.G., Estepa Molina, C.,. 2010, A rapid field procedure for screening trace elements in polluted soil using portable X-ray fluorescence (PXRF): Geoderma 159(1-2), 76-82.

Pelton, S. H., Ward, S. H., Hallof, P. G., Sill, W.,. 1978, Mineral discrimination and removal of in multifrequency IP: Geophysics, 43, 588-609.

Placencia-Gómez, E., Slater, L.D.,. 2014, Electrochemical spectral induced polarization modeling of artificial sulfide-sand mixtures: Geophysics 79(6), EN91-EN106.

Placencia-Gómez, E., Parviainen, A., Slater, L.D., Leveinen, J.,. 2015, Spectral induced polarization (SIP) response of mine tailings: Journal of Contaminant Hydrology 173, 8-24.

Wong, J., 1979. An electrochemical model of the induced polarization phenomenon in disseminated sulfide ores. Geophysics, 44(7), 1245–1265.

2D Cole-Cole Inversion of Time-Domain IP Data Measured in Krauthausen, Germany

Hannah Langenbach
Institute of Geophysics and Meteorology,
University of Cologne
Albertus-Magnus-Platz 2, 50923 Cologne, Germany
langenbach@geo.uni-koeln.de

Bülent Tezkan
Institute of Geophysics and Meteorology,
University of Cologne
Albertus-Magnus-Platz 2, 50923 Cologne, Germany
tezkan@geo.uni-koeln.de

SUMMARY

In October 2012 and 2013 overall 14 time domain IP profiles were measured in Krauthausen, Germany using the Terrameter LS. A gradient array with an electrode distance of 2.5 m was used. The data quality conforms to the high requirements of the inversion algorithm. Time series were measured at every profile for at least 200 electrode combinations. Every time series consists of 7-11 transients.

For inversion of our IP time series we use the time dependence of the resistivity and evaluate the Cole-Cole models in time domain.
Using an approximate solution the forward model for every time point is solved directly in time domain and independently from each other.
For each cell a composed transient is inverted into a homogeneous Cole-Cole model independently of each other.

We were able to achieve a satisfying Cole-Cole model for the survey area. A two layer resistivity model is estimated. The second more resistive layer is also more chargeable. Model areas with high chargeability are correlated with areas with higher frequency exponents and higher relaxations times.

Key words: Time domain, 2D/3D inversion, Cole-Cole model

INTRODUCTION

In the 1940s the IP effect was first described by Cole and Cole (1941) and the IP method was used for mining explorations since the 1950s (Zonge and Wynn 1975). Conventional time-domain IP studies used resistivity and chargeability only, resulting in an incomplete description of the observed voltage decay. On the other hand to derive the subsoil structure the frequency-dependent conductivity is modelled for frequency domain measurements (e.g. Pelton et al. 1978).
A method to evaluate the Cole-Cole models in time-domain was developed by Guptasarma (1982). Furthermore, Yuval and Oldenburg (1997) described an approach considering the time dependence of the chargeability for 2D inversion of time-domain IP data. There are a few approaches taking the whole transient into acount (e.g. Hönig and Tezkan, 2006; Fiandaca et al. 2012).

For our measurements in Krauthausen we used the Terrameter LS, ABEM (lent from the University of Lund). Krauthausen is a test site of the Forschungszentrum Jülich GmbH, Germany. We measured whole IP transients up to 6 sec. This is necessary to resolve the Cole-Cole parameters accurately.
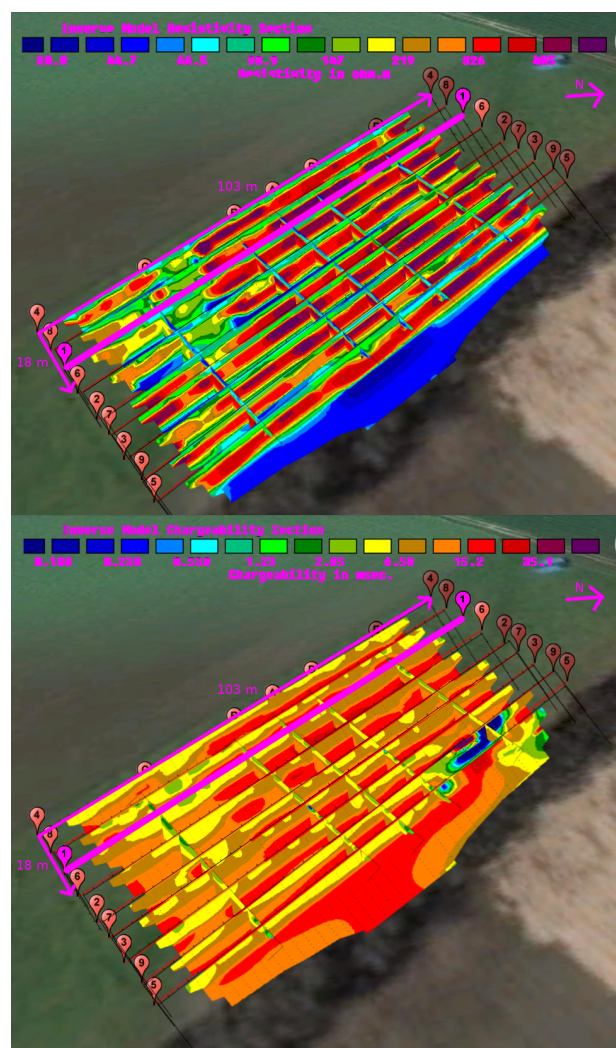

Figure 1. RES2DINV inversion results for the resistivity (top) and the integrated chargeability (bottom). 14 profiles were measured in Krauthausen, Germany.

For inversion, we use the time dependence of the resistivity and evaluate the Cole-Cole models in time domain. First the electrical field at each time point is independently inverted using a DC forward modelling code (Spitzer,1995). Afterwards the estimated time-dependent resistivity for each

cell is inverted into a homogeneous Cole-Cole model independently of each other.
The efficiency of the algorithm is demonstrated using synthetic and field data.

MEASURED DATA

In October 2012 and October 2013 overall 14 profiles were measured in Krauthausen using the Terrameter LS.
For an overview conventional inversion results with RES2DINV are shown in Figure 1 for resistivity and for integrated chargeability.

Per profile approximately 200 time series were measured. Every time series consists of 7-11 transients, which were stacked after filtering and cuting the whole time series. For every time point of every transient the standard deviation is calculated. As an example a stacked transient measured by the first receiver at profile 1 is shown in Figure 2.
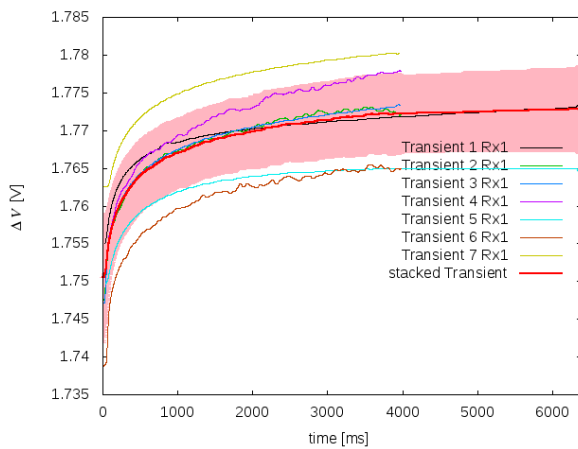

Figure 2. Measured and stacked transients measured by the first receiver of profile 1. The standard deviation is marked in light red.

2D INVERSION OF FIELD DATA

In time domain the exact solution of the IP effect can be realised by using equation (1), where r' denotes the coordinate of the current source, I is the current, δ is Dirac's delta function, ρ is the resistivity and E is the electrical field.

$$\Delta \cdot \left(\frac{1}{\rho(t,r)} * E(t,r) \right) = I \delta(r-r') \tag{1}$$

The electrical field values are calculated in the frequency domain and then transformed into the time domain using the fast Hankel transformation.

Using an approximate solution (equation (2)) the forward problem is solved directly in the time domain. Every time point can be calculated independently from each other.

$$\Delta \cdot \left(\frac{1}{\rho(t,r)} \cdot E(t,r) \right) = I \delta(r-r') \tag{2}$$

First of all the last time points of all transients are commonly inverted in a resistivity model (Figure 3).

This model is used as a starting model for the inversion of all other time points. Because of this relatively good starting model the resistivity models for all time points are similar to each other.
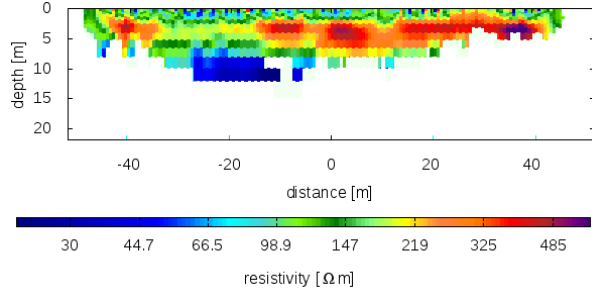

Figure 3. 2D DC resistivity model of Profile 1 (see Figure 1) of the last inverted time point (3.4 s). White areas are faded out according to sensitivity calculations.

In Figure 4 measured and calculated transients of the first receiver of Profile 1 are shown. The fit is satisfying with a RMS error of 1.45%. Calculating χ^2 an error of 6% is supposed including statistical errors. With a χ^2 of 0.17 the transient is slightly over fitted.
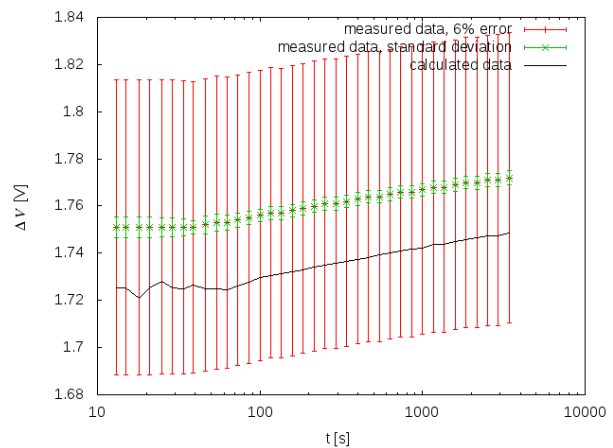

Figure 4. The calculated transient is plotted in black, red dots mark the measured transient, the standard deviation is colour-coded green and the 6%error-range is shown in red.
The RMS error of the first receiver of Profile 1 is 1.45% and χ^2 is 0.17 .

Finally each cell is inverted into a homogeneous Cole-Cole model after equation (3) independent of each other.

$$\rho(\omega) = \rho_0 \left(1 - m \left(1 - \frac{1}{1 + (i \omega \tau)^c} \right) \right) \tag{3}$$

In Figure 5 a composed transient of the different 2D DC inversions of the different time points (of the topmost cell for profilemeter -20 m) and the calculated Cole-Cole transient are shown as an example.
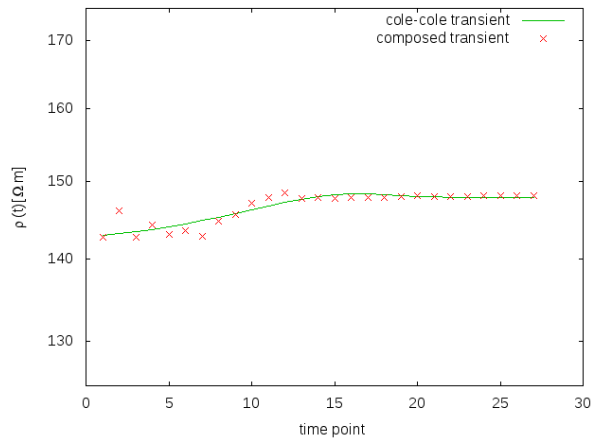
Figure 5.   A composed transient from the 2D DC inversions of each time point is marked with red dots and the calculated Cole-Cole transient is plotted in green. The RMS error is 1.41%. The cell is located at (-20,0).

The estimated resistivity ρ and chargeability m are shown in Figure 6. As expected the Cole-Cole resistivity results are akin to 2D DC resistivity model of the last time point (see Figure 3). The chargeability is higher in the deeper part of the model.
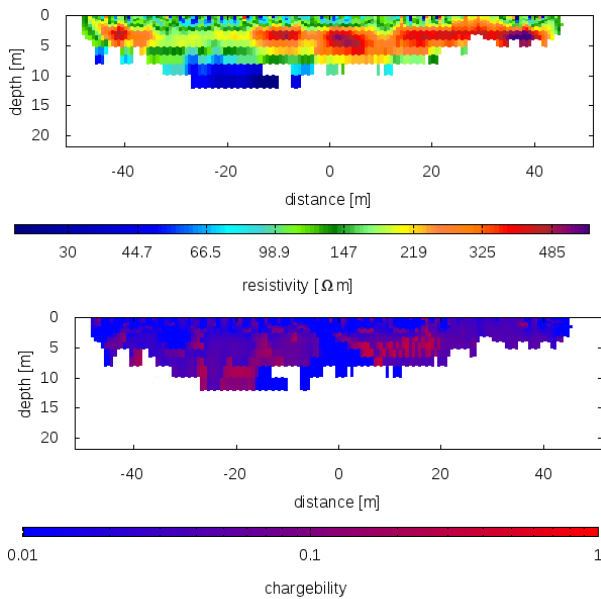

Figure 6. Cole-Cole Inversion results for resistivity (top) and chargeability (bottom) for profile 1 in Krauthausen, Germany.   White areas are faded out accorrding to sensitivity calculations.

In Figure 7 the results for the frequency exponent c and the relaxations time τ are shown.   Model-areas with high chargeability are correlated with areas with higher frequency exponents and higher relaxations times.
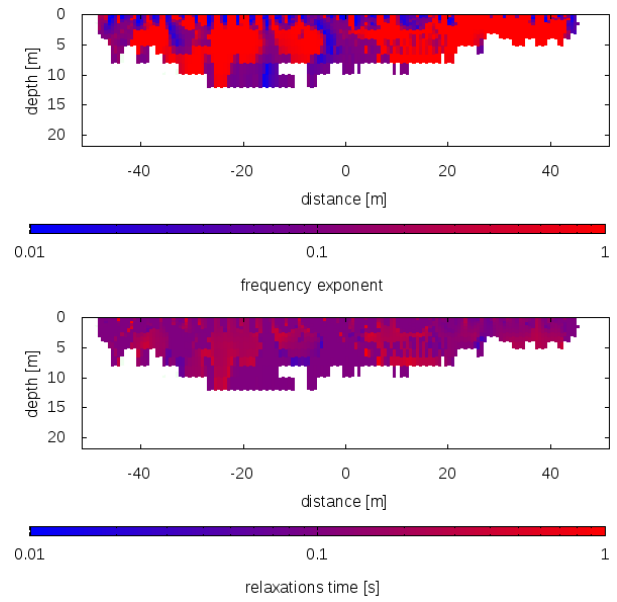

Figure 7.   Cole-Cole Inversion results for frequency exponent (top) and relaxations time (bottom) for profile 1 in Krauthausen, Germany.   White areas are faded out according to sensitivity calculations.

CONCLUSIONS AND OUTLOOK

In 2012 and 2013 14 time domain IP profiles were measured in Krauthausen, Germany.   The measured data quality conform to the high requirements of the inversion algorithm. We were able to achieve a satisfying Cole-Cole model for the survey area.
Currently the inversion algorithm is extended to 3D and the approach after Dias (2000) is supplemented.

REFERENCES

Cole, K.S. and Cole, R.H., 1941, Dispersion and absorption in dielectrics, I. Alternating current characteristics: Journal of Chemical Physics 9, 341–351.

Dias, C.A., 2000, Developments in a model to describe low-frequency electrical polarization of rocks:. Geophysics 65, 437–451.

Fiandaca, G., Ramm, J., Gazoty, A., Christiansen, A. V. and Auken, E., 2012, Resolving spectral information from time domain induced polarization data through 2-D inversion: Geophys. J. Int, doi:10.1093/gji/ggs060.

Guptasarma, D., 1982, Computation of the time-domain response of a polarisable ground: Geophysics 47, 1574–1576.

Hönig, M., and Tezkan, B., 2006, 1D and 2D Cole-Cole-inversion   of   time-domain   induced-polarization   data: Geophysical Prospecting 55, 117-133.

Pelton, W.H., Ward, S.H., Hallof, P.G., Sill, W.R. and Nelson, P.H., 1978, Mineral discrimination and removal of inductive coupling with multifrequency IP: Geophysics 43, 588–609.

Spitzer, K., 1995, A 3D finite-difference algorithm for DC resistivity models using conjugate gradient methods: Geophysical Journal International 123, 903–914.

Yuval and Oldenburg, D., 1997, Computation of Cole-Cole parameters from IP data: Geophysics 62, 436–448.

Zonge, K.L. and Wynn, J., 1975, Recent advances and applications in complex resistivity measurements: Geophysics 40, 851–864.

Mapping the lithotypes using the in-situ measurement of time domain induced polarization: El-log

Esben Auken   **Gianluca Fiandaca**   **Anders V Christiansen**   **Pradip Kumar Maurya**   **Helle Holm**

HydroGeophysics Group, Institute for Geoscience, Aarhus University
C. F. Møllers Alle 4, DK-8000 Aarhus C, Denmark
Esben.auken@geo.au.dk

SUMMARY

This study presents a novel application of the El-log-drilling technique for measurement while drilling of the DC, time domain IP and gamma log. In addition pore water samples can be taken at arbitrary levels. The technique itself is developed in Denmark and has been widely used in the field of ground water and environmental studies. The El-log drilling method yields detailed information on small changes in lithology, sediment chemistry and water quality and with data comparable to what can be obtained in the laboratory. .

We collected the data at a landfill site located near Grindsted in the southern part of Denmark. The purpose of the study was 1) to obtain a direct correlation between the undisturbed geophysical logs and surface measurements, 2) correlation of IP parameters to lithology and grain size distribution and 3) to investigate any correlation with effluent and IP parameters. We inverted the recorded resistivity and IP decays using full decay modelling with the Cole –Cole model and found that the chargeability correlates very well the clay content in the sandy aquifer.

Key words: El-log, Borehole IP, Time domain IP, Cole-Cole model

INTRODUCTION

An accurate delineation of subsurface lithology is achieved by geophysical borehole log, particularly gamma and electrical logs used in hydrogeological investigations. Often the electrical logging is carried out after the borehole is made where the measured formation resistivity is affected by the borehole fluid. However, with the El-log drilling techniques it is possible to measure the geophysical properties of undisturbed formations. In Denmark this technique has been widely used for hydrogeological studies in unconsolidated sediment (Sørensen and Larsen, 1999).

In the present study, we have exploited the El-log method for in-situ measurements of the time domain induced polarization signal together with the resistivity measurements. The data represent undisturbed samples comparable to what can be obtained by measurement in the laboratory. The data were collected close to a landfill located at Grindsted (southern part of Denmark). Later on, IP data were inverted using the Cole-Cole model (Fiandaca et al., 2012). An interpretation made together with gamma log reveals a detailed description of different lithological units.

METHOD AND RESULTS

Ellog Method

The Ellog is a high resolution drilling technique used in groundwater and environmental investigations in unconsolidated sediments. With this method apparent formation resistivity and chargeability are measured using the electrodes integrated with the hallow stem augur. In addition, it measures the gamma radiation, and water samples can be taken at any arbitrary level. The electrodes are embedded in insulating material and connected through the cables to the resistivity meter on the ground (Figure 1) while the gamma sensor is inside the auger close to the tip. The water sampler device is also inside the auger and is connected with tubes to the surface.
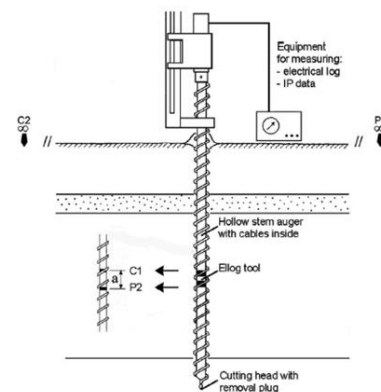

Figure 1 Principal sketch of the El-log drilling rodP are the potential electrode and C are the current electrodes. The distance a is equal to 20 cm. A gamma log is located inside the auger. Water samples are taken through inlets close to the drill tip. Modified from Sørensen and Larsen, 1999.

The field site and data acquisition

The field site is located at Grindsted landfill in the southern part of Denmark (Figure 2). The landfill is located on a glacial outwash plain with 10.12 m quaternary sand layer in the top and a regional tertiary sand layer, which extends to the depth of 80m and is confined by a clay layer. The target of the investigation is to delineate the inter-bedded thin layers of clay and lignite.

For recording of resistivity and IP data we used the LS-Terrameter instrument by ABEM. The instrument was remote controlled by an in house developed instrument that also acquired the gamma log data. A Pole-Pole type of configuration was used for measurement where three potential and one current electrodes were embedded in the augur and two electrodes were placed on the surface as remote electrodes. The on and off time length for the time decay measurement was 4 seconds. The full waveform data were recorded at a sampling rate of 3750 Hz. The positions of the boreholes (B1, B3 and B5) are shown in figure 2.
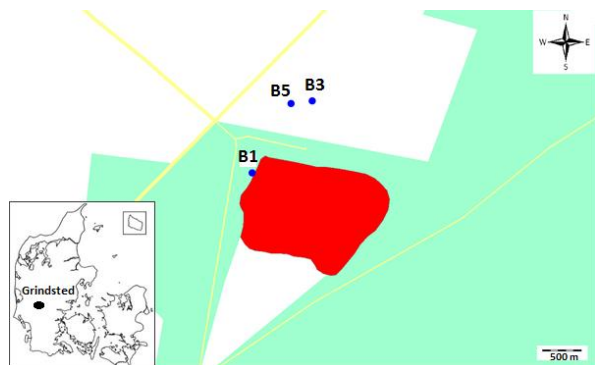
Figure 2 Location of the field site: landfill is shown in red, boreholes are shown by blue dots

Data processing and Inversion

IP signals suffer from two major problems during data acquisition- 1) Noise from power lines, which limits the use of the signal at early times 2) Background-potential drift in the measured signal distorting the shape of the IP decays in the late times. In order to recover the maximum spectral information from the time domain IP data, a recently developed signal processing algorithm (Fiandaca, et al., 2015) is applied on the full waveform recorded signal. Using this algorithm, the fundamental frequency of power lines and their harmonics are cancelled, thus allowing the use of earlier and narrower gates down to a few milliseconds. After the harmonic de-noising and removal of background drift, the signal is re-gated using logarithmically scaled gates.

The data were inverted following Fiandaca et., al (2012) (Auken et al. 2015). This code uses the Cole-Cole model for parameterization and takes into account full waveform, stack size and filter characteristics of the instrument. The data space consists of apparent resistivity and apparent chargeability for each gate and the model space consists of the four Cole-Cole parameters namely, resistivity (ρ), chargeability (m0), relaxation time (τ) and frequency exponent (c).

Results

Figure 3 shows the inversion results (including normalized chargeability) from the borehole B3 along with the gamma log. Total drilling depth for this borehole was 32.5 m. A geological log was made one meter apart from the Ellog and is also shown in Figure 3. The different lithological units correlate well with gamma, resistivity and the m0 log. The high chargeability peak (~100 mv/v) around 10 m 15 m and 27.5 m are very well correlated with the thin mica saturated clay and lignite layers, which is also strongly supported by the peaks in gamma log. The low resistivity seen from a depth of 17 m to 27m is the zone where contamination from the landfill is observed. Overall, results show very good agreement with the geological log.

CONCLUSIONS

The presented study shows how in-situ measurements of resistivity, IP and gamma log data are efficiently collected with the El-log method. Spectral information was retrieved using the 1D inversion of full time decay data. The method has shown that it is possible to make a very accurate correlation between geology and the geophysical parameters.

ACKNOWLEDGMENTS

REFERENCES
Auken, E., Christiansen, A. V., Fiandaca, G., Schamper, C., Behroozmand, A. A., Binley, A., Nielsen, E., Effersø, F., Christensen, N. B., Sørensen, K. I., Foged, N., and Vignoli, G.,2015, An overview of a highly versatile forward and stable inverse algorithm for airborne, ground-based and borehole electromagnetic and electric data: Exploration Geophysics, 2015, 223-235

Fiandaca, G., E. Auken, A. Gazoty, and A. V. Christiansen, 2012, Time-domain induced polarization: Full-decay forward modeling and 1D laterally constrained inversion of Cole-Cole parameters: Geophysics, v. 77, p. E213-E225.

Fiandaca, G., Olsson, P-I., Auken, E., Larsen, J. J., Maurya, P. K., & Dahlin, T. (2015). Doubling the Spectrum of Time-Domain Induced Polarization: Removal of Harmonic Noise and Self-Potential Drift. Abstract from AGU Fall Meeting 2015, San Fransisco, United States.

Sørensen, K. I., and F. Larsen, 1999, Ellog Auger Drilling: 3-in-one Method for Hydrogeological Data Collection: Ground Water Monitoring & Remediation, v. 19, p. 97-101.
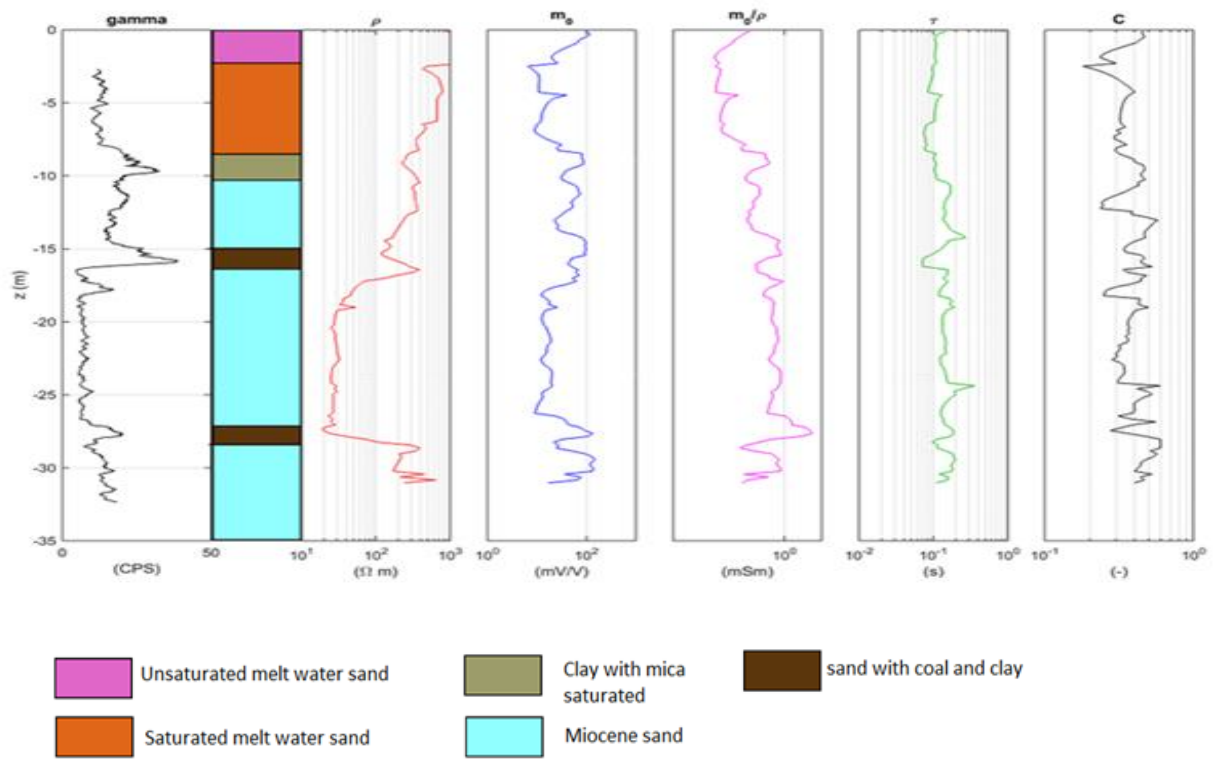
.

Figure 3 Inversion results of borehole B3, Geological log are shown between the resistivity and gamma log. Color code represents the different lithological units

IP2016/4th International Workshop on Induced Polarization

Is the IP response related to geology or contaminants in a leachate plume at the Grindsted Landfill, Denmark?

Ingelise Møller
Geological Survey of
*   Denmark and Greenland*
C.F. Møllers Allé 8, 8000 Aarhus C
ilm@geus.dk

Pradip K. Maurya
Department of Geoscience
Aarhus University
C.F. Møllers Allé 4, 8000 Aarhus C
pradip.maurya@geo.au.dk

Nicola Balbarini
Department of Environmental Engineering
Technical University of Denmark
Bygningstorvet, 2800 Kgs. Lyngby
nbal@env.dtu.dk

Gianluca Fiandaca
Department of Geoscience
Aarhus University
C.F. Møllers Allé 4, 8000 Aarhus C
Gianluca.fiandaca@geo.au.dk

Anders V. Christiansen
Department of Geoscience
Aarhus University
C.F. Møllers Allé 4, 8000 Aarhus C
anders.vest@geo.au.dk

Helle Holm
Department of Geoscience
Aarhus University
C.F. Møllers Allé 4, 8000 Aarhus C

Vinni K. Rønde
Depart. of Environmental Engineering
Technical University of Denmark
Bygningstorvet, 2800 Kgs. Lyngby
vikar@env.dtu.dk

Knud E. S. Klint
Geological Survey of
*   Denmark and Greenland*
Ø. Voldgade 10, 1350 Copenhagen K
kesk@geus.dk

Esben Auken
Department of Geoscience
Aarhus University
C.F. Møllers Allé 4, 8000 Aarhus C
esben.auken@geo.au.dk

Poul L. Bjerg
Depar.t of Environmental Engineering
Technical University of Denmark
Bygningstorvet, 2800 Kgs. Lyngby
plbj@env.dtu.dk

SUMMARY

Contaminants in leachate plumes from landfills and other contaminated sites are a threat to the environment. Efficient site characterization methods are needed. The perspectives of the IP method are investigated in combination with geological sampling and chemical analyses of water samples. Along a leachate plume from a landfill hosting both household and chemical waste, borehole IP data, geological samples, grain size, and contaminant concentrations in water samples are examined for correlations related to geology and concentrations of contaminants.

Results relating the Cole-Cole parameters with sediment types and pore water resistivity representing the concentrations of the contaminants show that the formation resistivity primarily is controlled by the contaminant concentrations while the IP parameters primarily are related to the clay content and grain size distribution of sandy sediments at the site.

Key words: Cole-Cole parameters, clay content, grainsize analyses, landfill leachate plume.

INTRODUCTION

Leachate plumes from landfills and other contaminated sites are a threat for groundwater, surface water, and eco systems. Efficient mapping and site characterization are required for the establishment of reliable monitoring and remediation plans.

The GEOCON project aims at advancing geological, geophysical and contaminant monitoring technologies for contaminated site investigations. The induced polarization method (e.g., Revil et al. 2012) both applied at the surface and in boreholes is brought into an integrated site characterization scheme with water sampling, geological and hydrogeological site models and coupled transport models. One of the research questions that have to be addressed is whether it is possible to separate the IP response from the contaminants from the ones from the geology. To answer this question we examine borehole IP data, geological samples, grain size, and contaminant concentrations in water samples along a leachate plume from a landfill hosting both household and industrial chemical waste using various statistical tools. Preliminary results are presented here.

METHOD AND RESULTS

The field site and the geological setting

The field site, Grindsted Landfill is situated in the south-western part of Jutland, Denmark. The landfill has been active for about 50 years from the 1930'ies to the 1970'ies, where household waste and construction material have been deposited along with chemical waste from a local chemical industry (Kjeldsen et al. 1998).

In the area thin layers of quaternary deposits cover Miocene deposits. The quaternary sediments mainly consists of coarse sandy meltwater deposits while the Miocene sediments primarily are medium to fine mica-rich sand and interbedded thin clay and lignite layers deposited in a flood plain or coastal lagoon environment.

The landfill, its leachate plume and the surrounding areas have earlier been subject to a high number of mainly chemical investigations of water samples from boreholes (e.g, Kjeldsen et al 1998).

Field methods and data

Three El-log drillings (Sørensen 1989) are carried out at the leachate plume in front of the Grindsted Landfill. The El-log method is expanded to measure time-domain IP along with the electrical resistivity in a 20 cm normal configuration and gamma radiation (Auken et al, 2016). The geophysical data are acquired in-situ while auger drilling. The DCIP data are inverted for the Cole-Cole parameters using a 1D vertical constrained inversion procedure (Fiandaca et al. 2012).

Since no useful geological samples are obtained by the El-log auger drilling, an additional borehole is drilled one metre a part from one of the El-log positions to achieve high quality geological samples. All samples are geologically described and selected samples are analysed for the grain-size distribution.

All boreholes are screened at different levels for water sampling. Additionally the El-log method collects water samples.
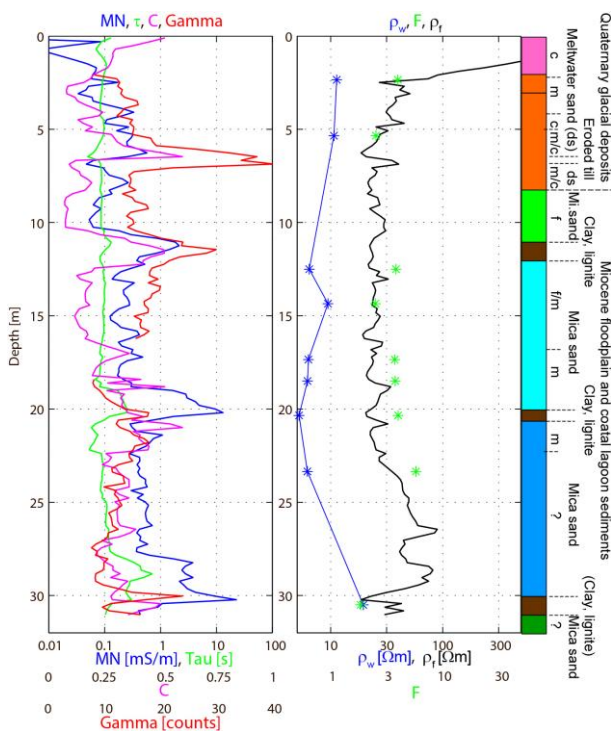

Figure 1. Geophysical borehole logs (Gamma, The Cole-Cole parameters: formation resistivity ρ_r, normalized chargeability MN, relaxation time τ, constant controlling the frequency dependence C), pore water resistivity (ρ_w), formation factor (F) and lithological log at borehole B1. The right-hand side colour-coded column indicate the geological log as observed in samples in the interval 0-22 m depth and interpreted from gamma log in the interval 22-32 m. The geological determined grain size of the sandy sediments are marked (f=fine, m=medium, c=coarse).

The logging results

The DCIP data from borehole B1 presented as Cole-Cole parameters are shown in Figure 1, together with the Gamma-log, the pore water resistivity measured on water samples at nine levels. At these nine levels the formation factor is calculated. The geological log from borehole B2, one metre a part from borehole B1, is supplemented with deposition environment, the sediment type and the geological determined grain size of the sandy sediments (Figure 1).

Correlations

The overall trend of the formation resistivity log measured by the El-log and the pore water resistivity measured on water samples are similar (Figure 1). The concentration of some of the contaminants controls the pore water resistivity and thereby the formation resistivity, at least in the clay-free parts of the ground. In other boreholes at the site, the non-contaminated pore water above the leachate plume is observed to have resistivities above 100 Ωm.

From a visual inspection of the DCIP log and the geological log it can be seen that the highest levels in the normalized chargeability above 1 mS/m are related to the clay and lignite layers (Figure 1). Cross plots of the Cole-Cole parameters colour-coded with the related geological description or interpretation display clear coherence between the Cole-Cole parameters and the sediment type (Figure 2). Different types of relationships are indicated in the cross plots for combinations of Cole-Cole parameters and sediment types related to clay content and grain size of the sandy sediments.

Taking all data into account there is no significant evidence of that the contaminants in the leachate plume at Grindsted Landfill influence on the IP response.

CONCLUSIONS

We examine borehole IP data, geological samples, grain size, and contaminant concentrations in water samples along a leachate plume from a landfill hosting both household and industrial chemical waste using various statistical tools with the purpose of addressing the question whether it is possible to separate the IP response from the contaminants from the ones from the geology.

In the primarily sandy sediments at the Grindsted Landfill we have observed (1) that the formation resistivity overall correlate with the pore water resistivity, representing concentrations of some of the contaminants, (2) that the IP parameters MN, τ and C seems to correlate with clay content and grain size of the sandy sediments and (3) that there is no significant evidence of that the contaminants influence on the IP parameters MN, τ and C.

ACKNOWLEDGMENTS

the Programme commision on sustainable energy and environment.

REFERENCES

Auken, E., Fiandaca, G., Christiansen, A.V., Maurya, P.K., Holm, H., 2016, Mapping the lithotypes using the in-situ measurement of time domain induced polarization: El-log: 4th International Workshop on Induced polarization.

Fiandaca, G., Auken E., Christiansen, A., and Gazoty A., 2012, Time-domain-induced polarization: Full-decay forward modeling and 1D laterally constrained inversion of Cole-Cole parameters: Geophysics, 77, E213–E225.

Kjeldsen, P., Grundtvig, Aa., Winther, P. and Andersen, J.S. 1998, Characterization of an old municipal landfill (Grindsted, Denmark) as a groundwater pollution source: Landfill history and leachate compostition: Waste Management and Research, 16, 3-13.

Revil, A., Karaoulis, M., Johnson, T., and Kemna, A., 2012, Review: Some low-frequency electrical methods for subsurface characterization and monitoring in hydrogeology: Hydrogeology Journal, 20, 617–658.

Sørensen, K., 1989, A method for measurement of the electrical formation resistivity while auger drilling: First Break 7, 403-407.
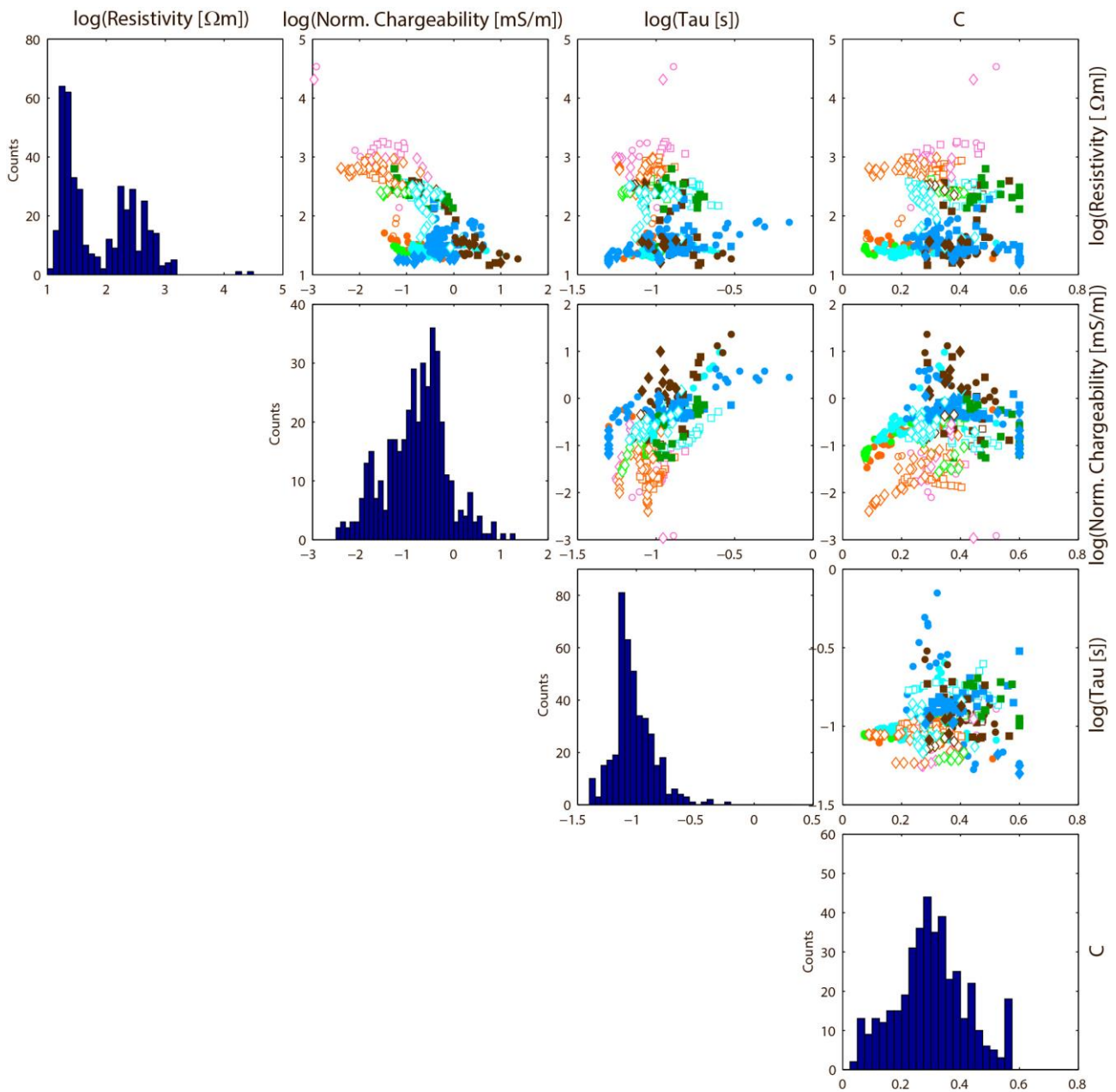

Figure 2. Histograms and cross plot of the Cole-Cole parameters from the three El-log drillings. The parameters are colour coded according to the geological log in Figure 1. An open plotting symbol indicates no or weak concentrations of contaminants, while a filled plotting symbol indicates high concentrations of contaminants. Data from B1, B3 and B5 are marked with a circle, square and a diamond, respectively.

Mapping and characterization of Induced Polarization in airborne TEM data from central East Greenland – application of a Self-Organizing Map procedure

Anaïs Brethes
GEUS, LTU
Øster Volgade 10,
1350 København K - Denmark
aib@geus.dk

Thorkild M. Rasmussen
Luleå University of Technology (LTU)
971 87 Luleå,
Sweden
thorkild.maack.rasmussen@ltu.se

Pierpaolo Guarnieri
GEUS
Øster Volgade 10,
1350 København K - Denmark
pgua@geus.dk

Tobias Bauer
LTU
971 87 Luleå,
Sweden
tobias.bauer@ltu.se

SUMMARY

Induced Polarization (IP) effects were observed in airborne Time Domain EM (TEM) data acquired in central East Greenland in the context of exploration for disseminated sulphides in a sedimentary basin. Some of the IP anomalies were targeted by drilling which revealed the absence of mineralization. In order to understand the possible causes of the IP effects we first identified them in the TEM data. IP indicators were extracted from the shape of the transient curves at every measurement location and were analysed by using a Self-Organizing Map (SOM) procedure. Results from K-mean clustering of the SOM are visualized on a geographical map showing the transient curves' characteristics. Some of the clusters are clearly correlated with the geology whereas others merely reflect recordings below the noise level. In order to interpret the cause of the IP anomalies the airborne TEM data were inverted for the Cole-Cole parameters.

Key words: Induced Polarization, Self-Organizing Map (SOM), Airborne Time-Domain EM, Cole-Cole parameters

INTRODUCTION

A high-resolution dual moment, i.e. Low Moment (LM) and High Moment (HM) airborne time-domain electromagnetic survey was conducted along the eastern margin of the Jameson Land basin in central East Greenland to explore for base metals. The survey area comprises crystalline basement to the East and layered Early Triassic to Jurassic sediments to the West. The layers are dipping a few degrees towards West. The Triassic sequence is 1 to 2km thick and mostly of continental origin. The fluviatile Early Triassic arkoses and conglomerates, the lower Middle Triassic grey limestone and black shale beds and overlying gypsiferous sandstones and mudstones are known to host disseminated sulphides (Harpøth et al., 1986). Sulphide mineralization was the target of an airborne TEM survey acquired with a SkyTEM system over an area of 550km^2. N-S oriented lines were flown with an average terrain clearance of 30m and a separation of 300m while E-W oriented tie-lines were flown with 4km separation. Additional lines were flown over 3 areas of particular interest with different orientation and a separation of 150m. The data were processed and inverted by SkyTEM Aps.

The conductivity models showed some conductive layers as well as IP effects in the data. IP effects in TEM data reflect the relaxation of polarized charges in the ground which can be good indicators of the presence of metallic particles. Some of these locations were drilled during the following field season but unfortunately did not reveal the presence of mineralization. The aim of this study is therefore to understand the possible causes of these IP effects. The remote location of the area prevents the data to be affected by cultural noise such as power lines, fences, etc. The electrical charge accumulation in the ground can be related to the presence of sulphides, oxides or graphite or to the presence of clays or fibrous minerals. Permafrost may also cause IP effects and is then expected to be associated with a highly resistive subsurface.

In order to spatially locate the areas where IP effects occur in the TEM data and compare them with the geology, the shape of the transient curve was analysed. IP effects can be indicated in the transients by:

- the presence of negative values;
- a very fast or very slow rate of decay of the positive part of the soundings (Smith and Klein, 1996).

Several characteristics of the transient curves (IP indicators) of the SkyTEM survey were extracted and analysed by using the Self-Organizing Map (SOM) technique. This is a type of neural network algorithm developed by Kohonen (2001) for analysis of multivariate data. The basic idea of SOM is to provide a method for easy visualizing of multi-dimensional data. The SOM may be viewed as a two-dimensional grid onto which multi-dimensional input data are projected or mapped from a multi-dimensional space (the space dimension is equal to the number of input variables) containing all the geographically distributed data characteristics from the transient curves. Input data that are similar or close to each other, irrespectively of geographic location, are mapped to the same or adjacent position in the SOM. A standard K-mean clustering procedure on the SOM grid is used to perform yet another simplification for easy visualization. Data that belongs to a particular cluster in the SOM data space can afterward be mapped into a geographical map. The SiroSOM software (Fraser and Dickson, 2007) was used for the SOM analysis. Once IP were identified and located, Cole-Cole parameters were recovered from the airborne TEM data in specific locations using the program AarhusInv developed by the hydrogeophysics group of Aarhus university (Auken et al., 2014).

SELF ORGANIZING MAP AND SPATIAL ANALYSIS OF THE IP EFFECTS

LM and HM data were respectively recorded over 20 and 21 gates from 12 to 1220µs and from 119 to 14686µs. The transients were analysed at every 10th measurement location along the flight lines for which 15 parameters (IP indicators) were calculated: (1) the sum of all negative values, (2) the sum of negative values in the most early local minimum, (3) the first negative value, (4) the gate of the first negative value, (5) the minimum value, (6) the gate of the minimum value, (7) the number of gates of consecutive negative values, (8) the maximum descending slope in the negative part, (9) the gate of the maximum descending slope in the negative part, (10) the maximum ascending slope in the negative part, (11) the gate of the maximum ascending slope in the negative part, (12) the maximum descending slope in the entire curve, (13) the gate of the maximum descending slope in the entire curve, (14) the maximum ascending slope in the entire curve, and (15) the gate of the maximum ascending slope in the entire curve.

Two examples of HM response curves are shown in Figure 1, which illustrates some of the characteristics of the survey data. The example from line L303101 (Figure 1a) has a very well-defined local minimum with 9 consecutive negative values in early gates. This is considered a clear indication of IP effects in the data. The example from Line 301901 (Figure 1a, b) has 3 consecutive negative values at the latest gates. A small local minimum with positive values is observed prior to the negative values. The data from the late gates from Line 301901 are close to or below the noise level. However, inspection of adjacent sample locations show a similar pattern, but it is difficult to exclude that systematic noise is causing the observed pattern.
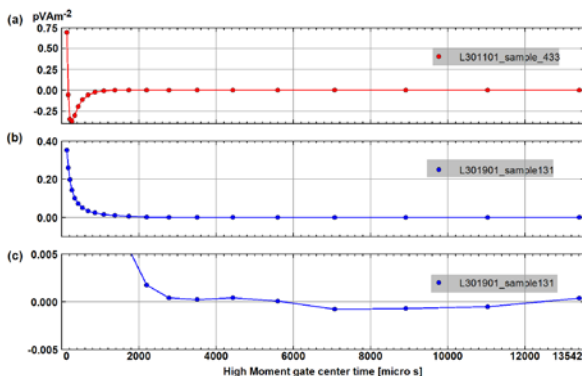

Figure 1. Examples of response curves from HM data. (a) data from L301101 with clear indication of IP effects; (b) data from Line L301901 showing possible but uncertain indications of IP, (c) similar as in (b) but different ordinate values.

For this study, HM data and LM data are analysed separately but they could easily also be analysed jointly. Prior to the SOM analysis of the response curve characteristics, the data were smoothed laterally using a running mean filter applied respectively over 345 points and 65 points to the HM and LM data. The running mean filtering was applied for random noise reduction. Each data type is furthermore normalized by their standard deviation for floating point number and by the range for integers. SOM grid cell sizes of 66x60 and 64x58 were used for the HM and LM data respectively. Figure 2 shows the

14 K-mean clusters of the SOM (grid) obtained from the analysis of the 15 dimensional HM data. SOM component maps corresponding to each of the 15 HM IP indicators are shown in Figure 3, which provides easy visualization of data correlations. The link between individual clusters and IP indicators can be seen by comparing similar grid locations in the maps shown in Figures 2 and 3. The corresponding geographical location of data within each cluster is shown in Figure 4 on the geological map.
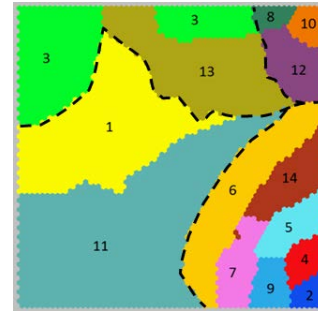

Figure 2. The fourteen K-mean clusters in SOM data space (66x60 grid cells) based on HM data. The dashed lines separate four clusters' groups based on the response curve pattern they represent and on the geological units they are correlated with.

A possible cause to the IP effects in this arctic area is permafrost. In this case, IP indicators would be expected over the whole survey area whereas it seems that they are localised to specific places that are discussed in the following paragraphs.

Inspection of Figures 2 and 3 shows that the clusters numbered 3, 8, 10, 12 and 13 have their first negative value of the transient curve at a very late gate. This may be explained by the signal being below noise level in the late gates as illustrated in Figure 1bc. They show very steep descending slope in the very first gates. Three of these clusters (8, 10 and 12) are located in alluvial fans close to the sea and along river beds where high conductivity is indicated in the surface layers. They are therefore considered not associated with IP. On the contrary, the clusters 2, 4, 5, 9 and 14 represent transient curves with the minimum values of the sum of negatives and their first negative and minimum values appear in the first time gates. They furthermore show negative values for at least 13 gates and may be considered as strong IP effects.

Some clusters (1 and 11 in HM data and 1, 4, 7, 8 and 13 in LM data [not shown]) are associated almost exclusively with areas where crystalline basement is outcropping (see Figure 4). The transient curves corresponding to the clusters from LM data start with negative values and then quickly become positive with oscillating behaviour within the noise level in the late gates. In the HM data the transient curves do not have significant negative values. Cluster 11 represent response curves that have the same pattern than in the LM data and cluster number 1 represents transient curves starting with positive but low values which pass below zero about 8 time gates later. We do not discuss these further in this study.

The remaining clusters which present stronger IP indicators appear to be concentrated in several areas. In the northwestern part of the survey area (see Figure 4a and b), the IP indicators in the HM data reveal a N-S elongated patch of almost

symmetrically distributed clusters (from west to east: clusters 6, 14, 5, 4, 5, 14 and 6). These clusters occur over outcropping Upper Triassic sediments and all describe the same transient curve pattern. However, the most negative sum of negatives, minimum value and first negative value are located in the central part of the patch and increase towards the sides. The minimum and first negative values appear in the earliest time gates and negative values are observed for 12 to 15 consecutive gates. The IP effect in this area is significant and stronger along the N-S elongated central part. This symmetry is less clear in the LM data which show quickly decaying transient curves that pass in the negative values in the late time gates. These elements suggest that the IP source body is elongated in a N-S direction.

Quaternary
Tertiary intrusions
Jurassic
Late Triassic
Middle Triassic
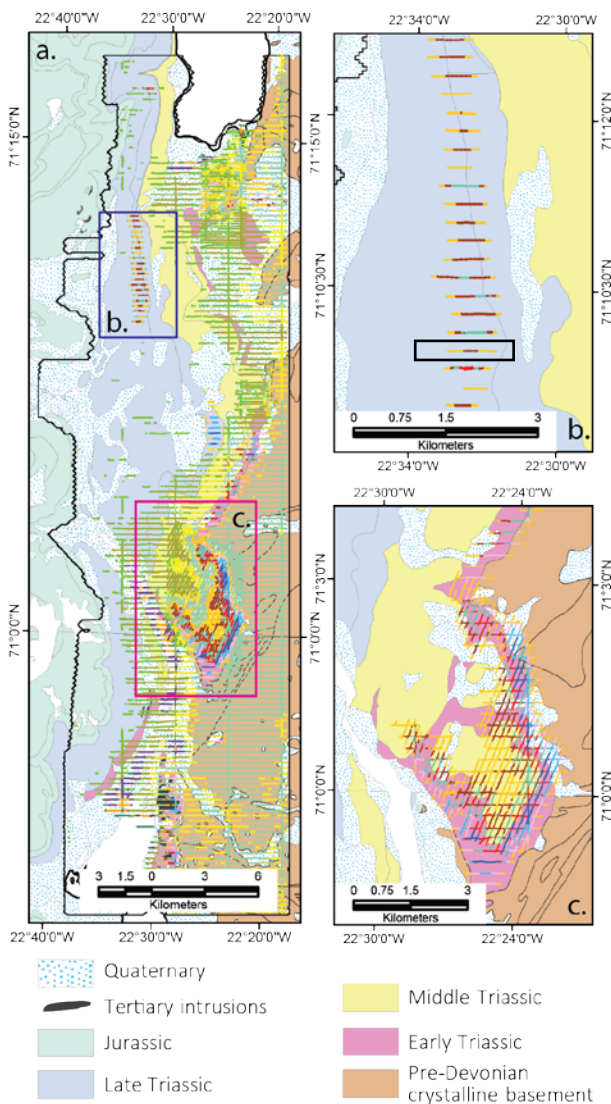Early Triassic
Pre-Devonian crystalline basement

Figure 4. IP indicators plotted with their respective cluster's colour defined from the SOM analysis of the HM TEM data (see Figure 2 for the clusters colour symbols). They are plotted over the simplified geology of the study area. The dark line represents the coverage of the SkyTEM survey and the blue and pink rectangles locate the Figures 4b, and c on which only clusters associated with strong IP effects are displayed. The rectangle on Figure 4b locates the data that are inverted in Figure 5.

In the central part of the survey area (see Figure 4a and c), the clusters are clearly correlated with the outcropping geology both in the LM and HM data. The area where the upper part of Middle Triassic sediments is outcropping is correlated with the clusters 6 and 14 in the HM data. They describe a transient curve which reaches negative values in relatively early time gates and stay in the negative part. Clusters 5, 4, 2, 9, 7 and 6 have the same transient curve shape starting in the negative part. However the clusters 4 and 2 which are correlated with the location of the uppermost part of the Early Triassic formation show curves with the steepest ascending slopes and the most negative sum of negative value. The clusters 7 and 6 are correlated with the transition between the outcropping Early Triassic sediments and the basement and show insignificant IP indicators compared to where Middle and Early Triassic sediments are outcropping in this area. In the same area the clusters in the LM data represent transient curves that all have the same pattern where Early and Middle Triassic sediments outcrop. However, the maximum decaying slope and earliest negative values reached are correlated with areas where the upper Lower Triassic and lower Middle Triassic sediments are outcropping. These elements indicate that the IP effects are correlated with lithological units in the upper part of Early Triassic sediments and lower Middle Triassic sediments that have been described to host base-metal sulphides (Harpøth et al., 1986).

INVERSION FOR COLE-COLE PARAMETERS

To further characterize the possible sources of IP that affect the airborne TEM data we inverted them using AarhusInv to recover their spectral content in terms of resistivity and of Cole-Cole parameters (Pelton et al., 1978). We present results from inversion of a subset of a flight line (see location on Figure 4b) with strong IP effects. The conceptual model used for the inversion presented here contains 4 layers. The noise ascribed to the data is defined as a linear function with slope -0.5 in a logarithmic presentation of data as function of gate centre time. The noise level at 1 ms is defined a $2.5 \cdot 10^{-12}$ T/s. An error floor of 3% is furthermore applied in the noise characterisation. The data entering the inversion are normalised by peak dipole moment and receiver area.
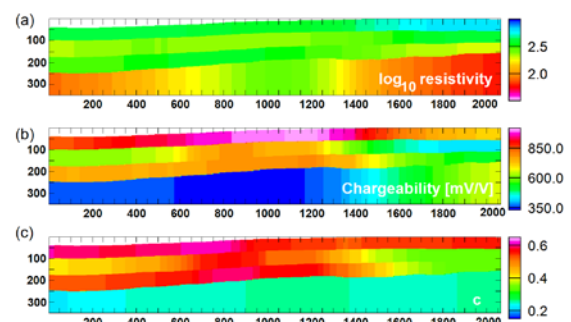

Figure 5. Model obtained from inversion of data from Line 104801 (data are shown in Figure 6)

Figure 5 shows the model and Figure 6 shows the corresponding measured data and model response. The general trend of the measured data is reproduced by the model responses. The highest chargeability values of 900mV/V are confined to the first 150 m in the central part of the section. It is correlated with high frequency constant c values (0.4 - 0.6) and resistivities are relatively low (300 Ωm). As IP effects due

to permafrost would influence the entire area and also show high resistivity values, we reject this possibility for this case. However, at this stage of the modelling it is difficult to discriminate other possible sources of IP effects as the presence of clays or disseminated sulphides.
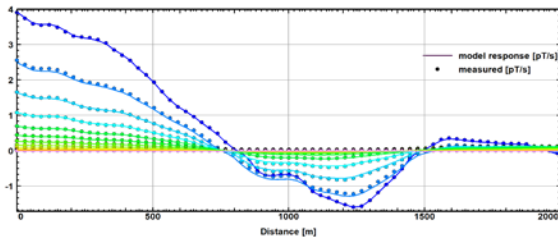

Figure 6. Measured HM data and model responses for the model in Figure 5. Measured data are shown by coloured circles and model responses are shown by corresponding solid lines.

CONCLUSIONS

The SOM analysis of the IP indicators extracted from the transient curves of LM and HM data is a very easy way to visualize the spatial distribution of the IP effects characteristics. Several areas affected by IP effects were described in terms of spatial distribution allowing correlations with the geology. We exclude permafrost as source of the IP effect. The inversion of the TEM data for the Cole-Cole parameters for a selected area was not conclusive with respect to the actual cause of the observed strong IP effect. The inversion however allowed to spatially define the IP source bodies. To complete the study, we will model the complex resistivity measurements from the drillcore samples of this area in order to recover the Cole-Cole parameters and compare them to the modelled IP parameters in the airborne TEM data.

REFERENCES

Auken, E., Christiansen, A.V., Kirkegaard, C., Fiandaca, G., Schamper, C., Behroozmand, A.A., Binley, A., Nielsen, E., Effersø, F., Christensen, N.B., Sørensen, K., Foged, N., Vignoli, G., 2014, An overview of a highly versatile forward and stable inverse algorithm for airborne, ground-based and borehole electromagnetic and electric data: Exploration Geophysics, 46, 223–235.

Fraser, S.J., and Dickson, B.L., 2007, A New Method for Data Integration and Integrated Data Interpretation: Self-Organising Maps: Fifth Decennial International Conference on Mineral Exploration, Toronto, Proceedings of Exploration 07, 907-910.

Harpøth, O., Pedersen, J.L., Schønwandt, H.K., Thomassen, B., 1986, The mineral occurrences of central East Greenland: Meddelelser om Gronland Geoscience 17.

Kohonen, T, 2001, Self-Organizing Maps Third Extended Edition: Springer Series in Information Sciences, vol. 30.

Pelton, W.H., Ward, S.H., Hallof, P.G., Sill, W.R., Nelson, P.H., 1978, Mineral Discrimination and Removal of Inductive Coupling with Multifrequency IP: Geophysics, 43, 588–609.

Smith, R.S., Klein, J., 1996, A special circumstance of airborne induced-polarization measurements: Geophysics, 61, 66 –73.
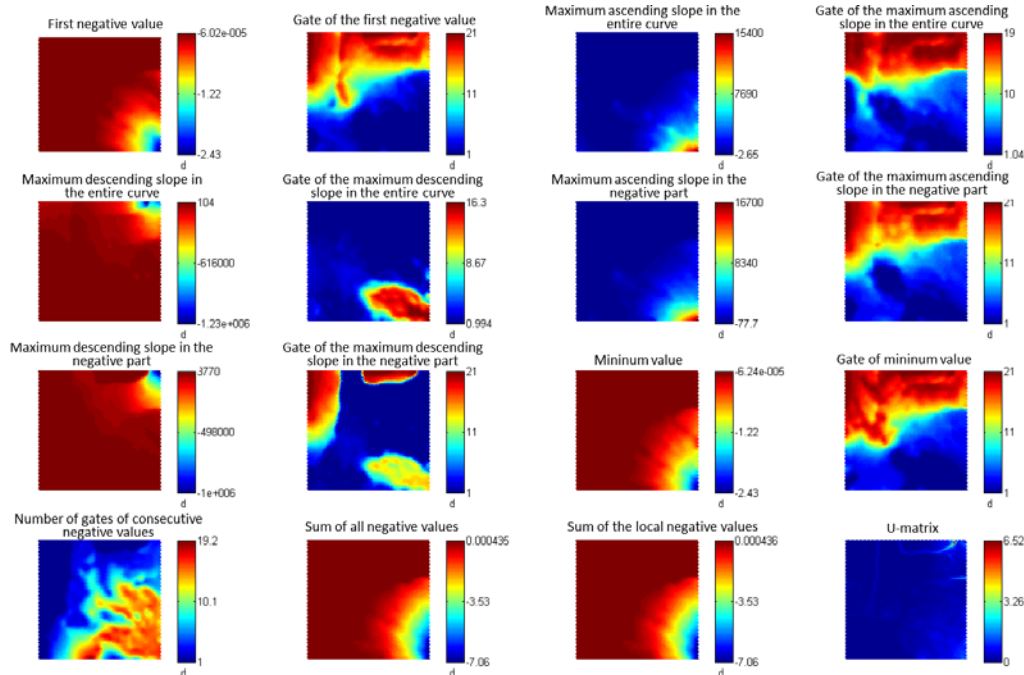
Figure 3. Component maps corresponding to each IP indicator in SOM data space. Similar data are associated with a common best matching unit (BMU) vector and the distance relation between BMUs for a particular grid location and the surrounding BMUs are visualized in the U-matrix by using a colour scale. In the present case, the clustering range is small.